Dark Cosmology Centre

Exploring Cosmology with Supernovae

A study of supernovae and their applications

Xue Li

Dissertation
Submitted for the Degree

PHILOSOPHIÆ DOCTOR

Supervisor: Prof. Jens Hjorth

Dark Cosmology Centre
The PhD School of Science
Faculty of Science

University of Copenhagen

Submission: *30, Sept, 2014*
Defence: *Anja C. Andersen*

Opponents: *Ariel Goobar*
Páll Jakobsson

ACKNOWLEDGEMENTS

Appreciation is a wonderful thing.
It makes what is excellent in others
belong to us as well.
Voltaire

Studying as a PhD is a special journey in my life that I could not have completed without many grateful helps from some people.

First and for most, I would like to thank my supervisor Jens Hjorth, not only for choosing me as his student, but also for his office door being always open for me and I can step in and ask questions anytime, not to mention most (at least some) of them are stupid questions. He shows me how good a human and a supervisor could be: patience, encouragement. I thank him for the tremendous useful and helpful discussions with me. I appreciate that he shared many good ideas with me, as well as taught me some basic knowledge on astronomy and astrophysics. I still remember the time when he taught me K correction, or peculiar velocity calculation, etc... He helped me out of the confusion about the usage of the definite article 'the' and the articles 'a' and 'an', corrected and improved my written English so much. I learnt from him the attitude towards science and scientific research, which I have been and will be benefit for my entire life.

Being a foreign especially quiet student, everything was different and strange to me. I must thank Michelle Cumming Løkkegaard, Corinne Toulouse-Aastrup, Julie Meier Hansen, Allison Wing-Shan Man and Karen Pardos Olsen for their helpful hands to pull me out of the hard times. I also thank all my Chinese friends here and abroad. They are 'Michelin three-star' cooks; they provide hugs and warm places when I need them; they make me feel at home, they share my happiness, etc.

I thank Johan Richard, Radosław Wojtak, Enrico Ramirez-Ruiz and Tamara Davis for many fruitful discussions, which helped me improve my publications. I thank Danuta Paraficz, Árdís Elíasdóttir and Johan Samsing for many helpful discussions on gravitational lensing. I also learnt a lot from Claudio Grillo, Andrew Zirm, Tomotsugu Goto and Teddy Frederiksen. I also thank Darach Watson, Daniele Malesani Giorgos Leloudas and Dong Xu for discussions on GRB and SNe. I thank my former and present office-mates: Peter Laursen, Stefan Geier, Martin Sparre, Caroline Heneka and Matteo Cataneo.

Without them, work would be much less interesting. I thank all the people at the Dark Cosmology Center for all the help I have got. It is my pleasure to meet you and I am really happy to work with all of you.

Finally some special thanks to my family for all the support and guidance. They are the lights in my heart when I am lonely in the dark. They have faith in me and make me a brave person to face and conquer the difficulties, and move forward.

Many thanks!

CONTENTS

Acknowledgements ii

Contents v

Abstract viii

Acronyms xii

List of Figures xiii

List of Tables xv

1 Introduction 1
- 1.1 Gravitational Lensing . . . 1
  - 1.1.1 theoretical introduction . . . 3
  - 1.1.2 Mass distribution . . . 7
  - 1.1.3 Time delay . . . 8
- 1.2 Supernovae . . . 10
  - 1.2.1 Brief introduction . . . 10
  - 1.2.2 Progenitor models . . . 10
  - 1.2.3 SNe Ia as standard candles . . . 14
  - 1.2.4 GRB-SNe . . . 17
- 1.3 Cosmology . . . 19
  - 1.3.1 cosmological parameters . . . 19
  - 1.3.2 Cosmological distance . . . 21

2 Gravitational lensing and supernovae 23
- 2.1 Introduction . . . 24
- 2.2 Time delay theory . . . 26
- 2.3 Modeling clusters of galaxies . . . 29
  - 2.3.1 The slope of the time-delay distribution . . . 31
  - 2.3.2 An example: Abell 1689 . . . 31
- 2.4 Time delays in 17 clusters . . . 35

2.4.1 Cluster selection and modeling . . . 35
2.4.2 Estimating β . . . 35
2.4.3 Parameter estimation . . . 35
2.5 The rate of lensed supernovae in Abell 1689 . . . 38
2.6 Summary and discussion . . . 43

3 GRB-SNe **46**
3.1 Introduction . . . 47
3.2 Light curves of GRB-SNe . . . 48
3.2.1 Host galaxy . . . 48
3.2.2 Afterglow . . . 49
3.2.3 Extinction, distance modulus, and rest frame time . . . 50
3.2.4 Polynomial function fitting . . . 50
3.2.5 K-correction . . . 51
3.3 Systems of GRB-SNe . . . 55
3.3.1 GRB 980425/SN 1998bw . . . 57
3.3.2 GRB 030329/SN 2003dh . . . 57
3.3.3 GRB 031203/SN 2003lw . . . 60
3.3.4 GRB 050525A/SN 2005nc . . . 60
3.3.5 XRF 060218/SN 2006aj . . . 60
3.3.6 GRB 090618 . . . 63
3.3.7 XRF 100316D/SN 2010bh . . . 63
3.3.8 GRB 120422A/SN 2012bz . . . 65
3.3.9 GRBs not included . . . 65
3.4 Properties of the light curves . . . 68
3.4.1 Luminosity-decline rate relation . . . 76
3.4.2 Time since burst . . . 78
3.4.3 Rescaling of light curves . . . 79
3.4.4 Discussion . . . 79
3.5 Conclusions . . . 81

4 Cosmological parameters with GRB-SNe **82**
4.1 INTRODUCTION . . . 82
4.2 GRB-SNE SYSTEMS . . . 83
4.2.1 Data Analysis . . . 84
4.2.2 Peculiar Velocity and Uncertainty of Distance Modulus of SN 1998bw 84
4.3 GRB-SNE AS STANDARD CANDLES . . . 87
4.4 CONSTRAINTS ON Ω_m and Ω_λ . . . 88
4.5 CONCLUSION . . . 88

5 Conclusions and outlook **92**

A Supplementary materials **95**
A.1 cross-checking of constraining the parameters α, Υ and Ω_m 95
A.2 Code test on scatters 98

B Coauthor statements **101**

Bibliography **106**

ABSTRACT

The most intriguing aspect of studying supernovae associated with gamma-ray bursts (GRB-SNe) is the fact that they are accompanied by the most energetic events in the universe: gamma-ray bursts (GRBs). GRBs are extremely bright, which makes a swift trigger of observation on them. Therefore, a supernova (SN) light curve following a GRB can be detected. In addition, GRB-SN rate does not decline beyond $z > 1.5$, which is a fundamental feature to breakdown degeneracies in the constraint on the equation of state parameter $w(z)$.

Apart from two exceptions, i.e., GRB 060614 and GRB 060505, all other long GRBs have been observed followed by a SN. Hundreds of GRBs are detected yearly though, properties and progenitor mechanism of GRB-SNe remain elusive, due to the difficulties in obtaining the light curves of GRB-SNe. For example, the brightness of a GRB and a host galaxy may conceal a GRB-SN, and dust in the line of sight may also blur the brightness of a GRB-SN.

In this thesis, supernovae (SNe), especially GRB-SNe are extensively explored and used as a tool to study the dark distant universe. We first intend to estimate the rates of observing a lensed SN behind Abell 1689. A function describing time delay distribution of strong gravitational lensing is developed. For Type Ia supernova (SNe Ia), the rate is lower than core-collapse supernovae (CC SNe). The rate of SNe Ia declines beyond $z \sim 1.5$. Based on these reasons, we investigate a potential candidate to measure cosmological distance: GRB-SNe. They are a subclass of CC SNe. Light curves of GRB-SNe are obtained and their properties are studied. We ascertain that the properties of GRB-SNe make them another candidate for standardizable candles in measuring the cosmic distance. Cosmological parameters Ω_M and Ω_Λ are constrained with the help of GRB-SNe.

The first Chapter presents a theoretical background of this thesis divided into three Sections. In the first Section, a theory of gravitational lensing is briefly introduced. The lensing effects are strongly depended on the mass distribution of a lensing cluster. We discussed models of mass distributions of a cluster of galaxies. We also theoretically deduce time delay. The second Section is dedicated to SN. Progenitor models of different types of SNe are investigated. SNe Ia and their application as standard candles are discussed. After that, we introduce updated research on GRB-SNe and difficulties in study their properties. The Chapter ends by discussing cosmological parameters Ω_M and Ω_Λ and cosmological distance.

In the second Chapter, we estimate the chance of observing an image of different types of SN lensed by Abell 1689. We analyze the rates and the time delay distribution of lensed sources with multiple images behind strong lensing galaxy clusters. In total 17 clusters are studied. We deduce a function presenting the probability distribution of time delays. A separation of the mass model of Abell 1689 is investigated to test the effects of different types of mass clumps on time delay distributions. It shows that its dark halo and bright galaxies are responsible for generating large time delays and small time delays are mostly produced by galaxy-scale clumps. We conclude that the chance of SN Ia is smaller than CC SNe, though both of them are low.

The third Chapter is devoted to the investigation of GRB-SNe. We discuss the possibility of generating light curves of GRB-SNe, who have 'strong evidence' to be connected with GRBs. In total 8 light curves are obtained. Based on these light curves, properties of GRB-SNe are explored. We find that the peak magnitudes are strongly correlated to the decline rates. Here the decline rate is defined as the decay of the magnitude after the light curve reaches its peak luminosity. This luminosity-decline rate relation is tighter than the widely discussed relation, i.e., $k-s$ relation, where k and s represent the relative brightness and width of light curves to SN 1998bw. We also stretch the light curve of SN 1998bw to test if it can be used as a light curve template for GRB-SNe. We find out that stretching the curve around the peak luminosity is superior to other methods, e.g., stretch with time since burst or the s factor.

In the fourth Chapter, cosmological parameters Ω_M and Ω_Λ are constrained with GRB-SNe, whose peak magnitudes are corrected with the help of the decline rates. With the standard Monte Carlo method, we simulate the magnitudes and the decline rates of 8 GRB-SNe and find the best cosmological parameters Ω_M and Ω_Λ in flat universe.

Finally, the thesis closes with a short discussion on the summary and potential future works in the fifth Chapter. The luminosity-decline rate relation can help to constrain the progenitor models of GRB and GRB-SNe. Though the progenitors and properties of SN Ia and GRB-SNe are different, GRB-SNe show similar light curve properties as SN Ia, therefore it can be used as standard candles to measure cosmic distance and constrain cosmological parameters Ω_M and Ω_Λ. Considering the rates of GRB-SNe do not decline beyong $z \sim 1.5$, with more GRB-SNe to be discovered, they will become a powerful tool in the study of dark energy through $w(z)$.

摘要

研究与伽玛射线暴相联系的超新星(GRB-SNe)最有趣的地方在于他们总是伴随着宇宙中最具能量的事件：伽玛射线暴(GRB)。伽玛暴极其的明亮，以至于一旦爆发我们可以发现并迅速地观测他们。因此，我们有机会观测到伽玛暴之后的超新星(SN)的光变曲线。另外，在红移z>1.5之外伽玛暴超新星率并不随着红移的增加而降低，这样可以在估算状态方程参数w(z)时破坏其简并性。

除了两个例外：GRB 060614 and GRB 060505, 其他所有长伽玛暴都可以观测到与之相联系的超新星。虽然每年可以观测到几百个伽玛暴，但是关于伽玛暴超新星的性质和前身机制仍不清楚，这是因为观测伽玛暴的光变曲线还是有困难的。比如，伽玛暴和宿主星系的光亮会遮挡住超新星，并且在观测路径上的尘埃也会掩盖超新星。

在这篇论文中，我们主要研究超新星，特别是伽玛暴超新星，并以他们为工具来探测遥远的黑暗宇宙。我们首先计算在Abell 1689背后，观测到被引力透镜放大的超新星的概率。 我们推导出关于强引力透镜的时间延迟分布的公式。Ia型超新星(SNe Ia)可被观测到的机会要小于核坍塌超新星（CC SNe)。 SNe Ia 率在红移z~1.5之外下降。基于此，我们研究一个潜在的可用来测量宇宙距离的候选者:伽玛暴超新星。它是一种次型 CC SNe 。我们得到伽玛暴超新星的光变曲线，并且研究其光变曲线的特点。我们确信他们光变曲线的特点使得伽玛暴超新星也可作为测量宇宙距离的标准烛光。而且我们利用伽玛暴超新星测量了宇宙常数Ω_M, Ω_Λ .

第一章论述了整篇论文的理论背景。分为三个部分。第一部分简要介绍了有关引力透镜的理论。透镜的星系团的质量分布会影响引力透镜效应。我们讨论了几种星系团的质量分布模型，并且介绍了时间延迟理论。第二部分主要介绍了超新星。我们研究了不同类型超新星的前身机制。我们讨论了Ia型超新星以及他们作为标准烛光的应用。之后，我们介绍了关于伽玛暴超新星的最近研究进展，以及研究中遇到的困难。本章的结尾讨论宇宙常数 Ω_M, Ω_Λ和宇宙距离。

在第二章 我们测算了在 Abell 1689背后观测不同类型超新星的像的概率。我们分析了强引力透镜星系团背后可观测到的超新星率和时间延迟分布。总计研究了17个星系团。我们推导出了时间延迟的概率分布。我们分离了 Abell 1689的质量模型来探讨不同类型的质量团对时间延迟分布的影响。结果表明暗物质晕和明亮的星系主产生长的时间延迟，而短的时间延迟主要由星系规模的质量团产生。 我们发现可观测到的Ia型超新星的机会要小于观测到核坍塌的超新星的机会，尽管观测到两种超新星的机会都比较小。

第三章主要研究伽玛暴超新星。我们讨论了得到伽玛暴超新星的光变曲线的可能性，有很强的证据证明这些超新星是与伽玛暴相联系的。总计得到8条光变曲线。基于这些光变曲线，我们研究了伽玛暴超新星的性质。我们发现了光变曲线的峰值和减光率有关联。减光率是指从光度峰值开始光变曲线下降的速度。这个光度－减光率关系比广泛讨论的k-s关系更紧密，这里k和s代表相对于SN 1998bw光变曲线的

亮度和宽度。我们也伸缩了SN 1998bw的光变曲线来测试它是否可作为伽玛暴超新星的光变曲线模板。我们发现在光度峰值附近伸缩比其他方式效果要好，比如优于伽玛暴爆发以来的时间，或者s系数。

第四章，利用被减光率修正了的伽玛暴的光度峰值，我们测量了宇宙常数Ω_M，Ω_Λ。我们用蒙特卡罗方法模拟了8个伽玛暴超新星的光度峰值和减光率，测量了在平坦宇宙中的最佳宇宙常数。

最后，第五章我们总结了本论文的内容，并展望了未来的工作。光度－减光率关系可以帮助我们约束伽玛暴超新星的前身模型。尽管Iα型和伽玛暴超新星的前身机制和性质不同，伽玛暴超新星和Iα型超新星的光变曲线有相同性质，因此它可以作为标准烛光来测量宇宙距离和宇宙常数Ω_M, Ω_Λ。考虑到在红移z>1.5时伽玛报超新星率并不降低，随着更多的伽玛暴超新星被观测到，他们可以用来测量状态方程的参数w(z)，成为研究暗能量的重要工具。

ACRONYMS

GRB-SNe	supernovae associated with gamma-ray bursts
GRBs	gamma-ray bursts
SN	supernova
SNe	supernovae
SNe Ia	Type Ia supernova
CC SNe	core-collaps supernova
SNR	supernova rate
SIS	singular isothermal sphere
dPIE	dual Pseudo Isothermal Elliptical mass distribution
NFW	Navarro-Frenk-White profile
WD	white dwarf
SD model	single degenerate mode
DD model	double degenerate mode
SFR	star formation rate
CMB	cosmic microwave background
XRF	X-Ray Flash

LIST OF FIGURES

1.1 Strong lensing diagram 2
1.2 Schematic view of of a lensing system 3
1.3 Critical lines for Abell 1689 with source at $z = 3$ 4
1.4 Caustic lines for Abell 1689 at $z = 1.83$ 5
1.5 A map of arrival time on the image plane with Lenstool 9
1.6 The crab supernova remnant 11
1.7 Classification of SNe 12
1.8 A schematic onion-like layers of a massive star before core collapse 13
1.9 Phillips relation of SNe Ia 15
1.10 Hubble diagram with 42 SNe Ia 16
1.11 Artist's image of a GRB 17
1.12 A diagram of light curve of GRB-SN 18
1.13 Combined results of constraint on Ω_M and Ω_Λ in ΛCDM model 20
1.14 The distance modulus at different cosmological models with z up to 10 . 22

2.1 The logarithmic probability distribution of the time delays for three density profiles 30
2.2 The time-delay distributions of Abell 1689 with modeled background sources at $z = 3$ 32
2.3 The distribution of parameter β for probability distribution functions of 17 clusters 36
2.4 The logarithmic probability distribution functions for 17 clusters with background sources at $z = 3$ 37
2.5 The cumulative rate ($N_{\rm SN}$) of the leading images of lensed supernovae in Abell 1689 40
2.6 The comparison of the supernova rates 42
2.7 The cumulative rate of observing a leading supernovae image, as a function of magnitude threshold 44

3.1 SN 1998bw peak SED and decline rate templates 52
3.2 The difference of peak magnitude (Δ) estimated via two K-corrections . . 54
3.3 GRB 980425/SN 1998bw 58

3.4 GRB 030329/SN 2003dh and GRB 031203/SN 2003lw 59
3.5 GRB 050525A /SN 2005nc and GRB 090618 61
3.6 XRF 060218 (SN 2006aj) 62
3.7 XRF 100316D/SN 2010bh 64
3.8 GRB 120422A/SN 2012bz 66
3.9 The peak-luminosity and decline rate relation for GRB-SNe with the decline times of 5, 10 and 15 days 69
3.10 Kendal's τ, Spearman's rank, and Pearson's correlation coefficients of the luminosity-decline rate relation and the $k - s$ relation 70
3.11 The relations between logarithmic peak time $\log t_{\rm peak}$, peak magnitude $M_{\rm V,peak}$ and decline rate $\Delta m_{\rm V,15}$ 71
3.12 The relations between the s factor, the k factor, the decline rate $\Delta m_{\rm V,15}$ and the peak magnitude $M_{\rm V,peak}$ 72
3.13 Different rescaling results of the the light curves of the selected systems in rest frame V band 73
3.14 Comparison of the peak magnitudes 74
3.15 Comparison of peak time 75

4.1 Peculiar velocities (line-of-sight component) in the direction of the supernova host galaxy, ESO 184−G82, as a function of the comoving distance from the Local Group formed the constrained simulation 85
4.2 Constraints on α, Υ and Ω_m assuming a flat cosmological model. 89
4.3 Hubble diagram for GRB-SNe 90

A.1 Cross-checking of the resultant parameters α, Υ and Ω_m 96
A.2 Cross-checking of the Hubble diagram for GRB-SNe 97
A.3 Uncertainties of best cosmological parameters as a function of pseudo-scatters of the pseudo-data generated in $\Omega_m = 0.3$ and $\Omega_\Lambda = 0.7$ 99

LIST OF TABLES

2.1 The slopes of the density profiles describing the mass distribution of a galaxy cluster and the slopes of the best-fitting functions to the time-delay distribution 28
2.2 Properties of 17 lensing clusters 34

3.1 The slopes and the break times for GRB 050525A and GRB 090618. 49
3.2 The selected systems and the relevant steps. 56
3.3 A list of unselected systems in class A, B, and C. 67
3.4 The selected systems and relevant results with 1σ uncertainties. 75
3.5 The most frequent values and the percentage of the correlation coefficients at different significance levels. Here we set the bin size equal to 0.01. . . . 77

4.1 Light curve properties of GRB-SNe systems 84

1

INTRODUCTION

The only reason for time
is so that everything
doesn't happen at once.
Albert Einstein

Abstract -
This chapter presents a briefly theoretical introduction of relevant topics studied in this thesis. The topics include gravitational lensing, supernovae and cosmology. For the first topic: gravitational lensing, we first present a brief theory of gravitational lensing, then we talk about the mass distribution of lensing clusters, and the section also presents a discussion of time delay. In the second section, supernovae are introduced. A classification of SNe, progenitor models of different types of SNe and a subclass of SNe: GRB-SNe are discussed. The third topic is about cosmology. We present cosmological parameters and discuss cosmological distance.

1.1 GRAVITATIONAL LENSING

Based on general relativity, a massive object, e.g., a star, a galaxy or a cluster of galaxies, could contort local space-time around it. This so-called gravitational lensing has been developed to a powerful tool in astronomy, astrophysics and cosmology studies.

In gravitational lensing regime, an object emitting the distorted light is denoted by source. A massive object which bend the light is called lens. According to lensing scales, it is divided into three subclasses. They are micro, week and strong lensing. The micro lensing happens where light rays is bent by a compact object, e.g., a star of a planet. In weak and strong lensing, a lens is a galaxy or a cluster of galaxies. In strong lensing, we can observe giant arcs, arclets and multiple images of lensed objects, while weak lensing is characterized by magnified or demagnified images and deformed shapes of a source galaxy. A schematic diagram of strong lensing (Kneib & Natarajan, 2011) is shown in Figure 1.1. This thesis is dedicated to strong lensing.

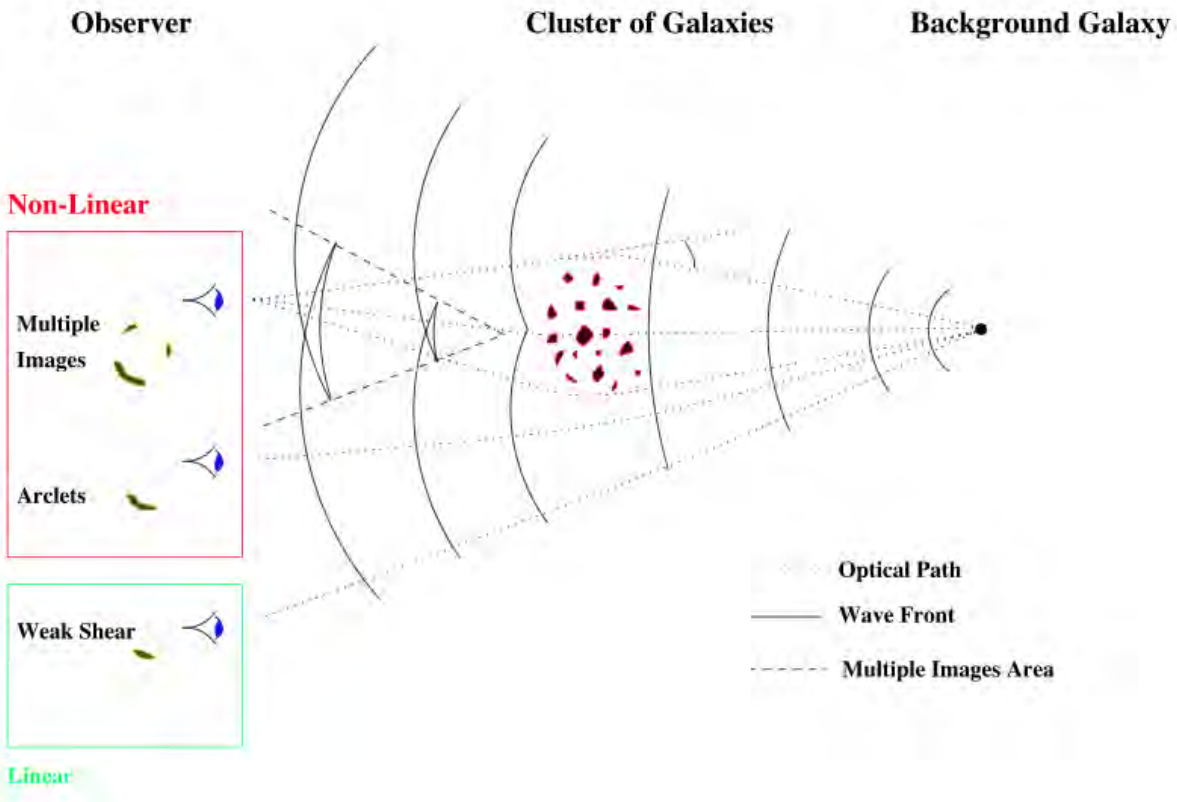

Figure 1.1: Strong lensing diagram (Kneib & Natarajan, 2011).

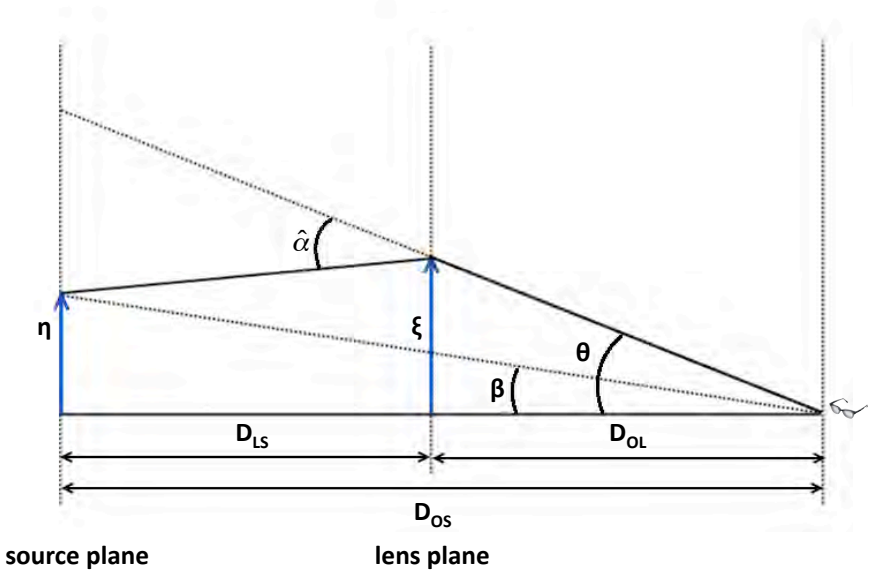

Figure 1.2: Schematic view of of a lensing system.

1.1.1 THEORETICAL INTRODUCTION

In Einstein's general relativity, space-time is distorted by the presence of mass. The Friedmann-Lemaître-Robertson-Walker (FLRW) metric is assumed to describe the universe

$$\mathrm{d}\tau^2 = \mathrm{d}t^2 - a^2(t)\left(\frac{\mathrm{d}r^2}{1-kr^2} + r^2\left(\mathrm{d}\theta^2 + \sin^2\theta\mathrm{d}\phi^2\right)\right), \tag{1.1}$$

where $a(t)$ is the scale factor and k presents curvature of the universe.

A configuration of lensing system is shown in Figure 1.2. When light rays emitted by a source on the source plane pass a lens on the lens plane, they are bent due to the presence of the lens mass. The angular position of the image θ is related to the deflection angle $\hat{\alpha}$ and the angular position of the source β. D_{LS}, D_{OL} and D_{OS} are the angular diameter distances between the observer (O), the lens (L) and the source (S). ξ and η are the positions of the lens and the source. Here the thin lens approximation is valid and optical effects due to the thickness of a lens is ignored. The structure of the lens along the

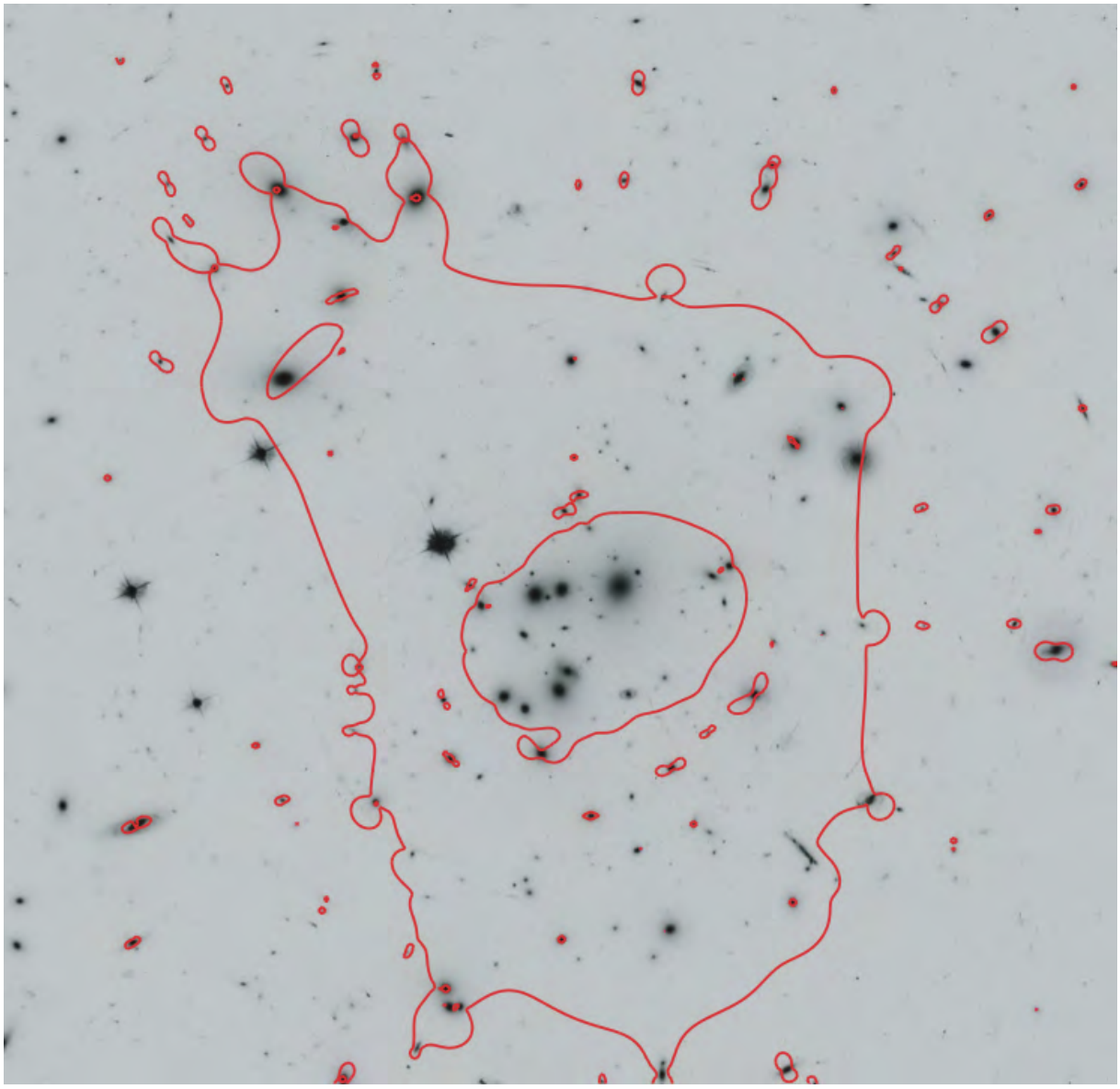

Figure 1.3: Critical lines for Abell 1689 with source at $z = 3$ (Limousin et al., 2007). The field is 485 kpc $\times$ 485 kpc.

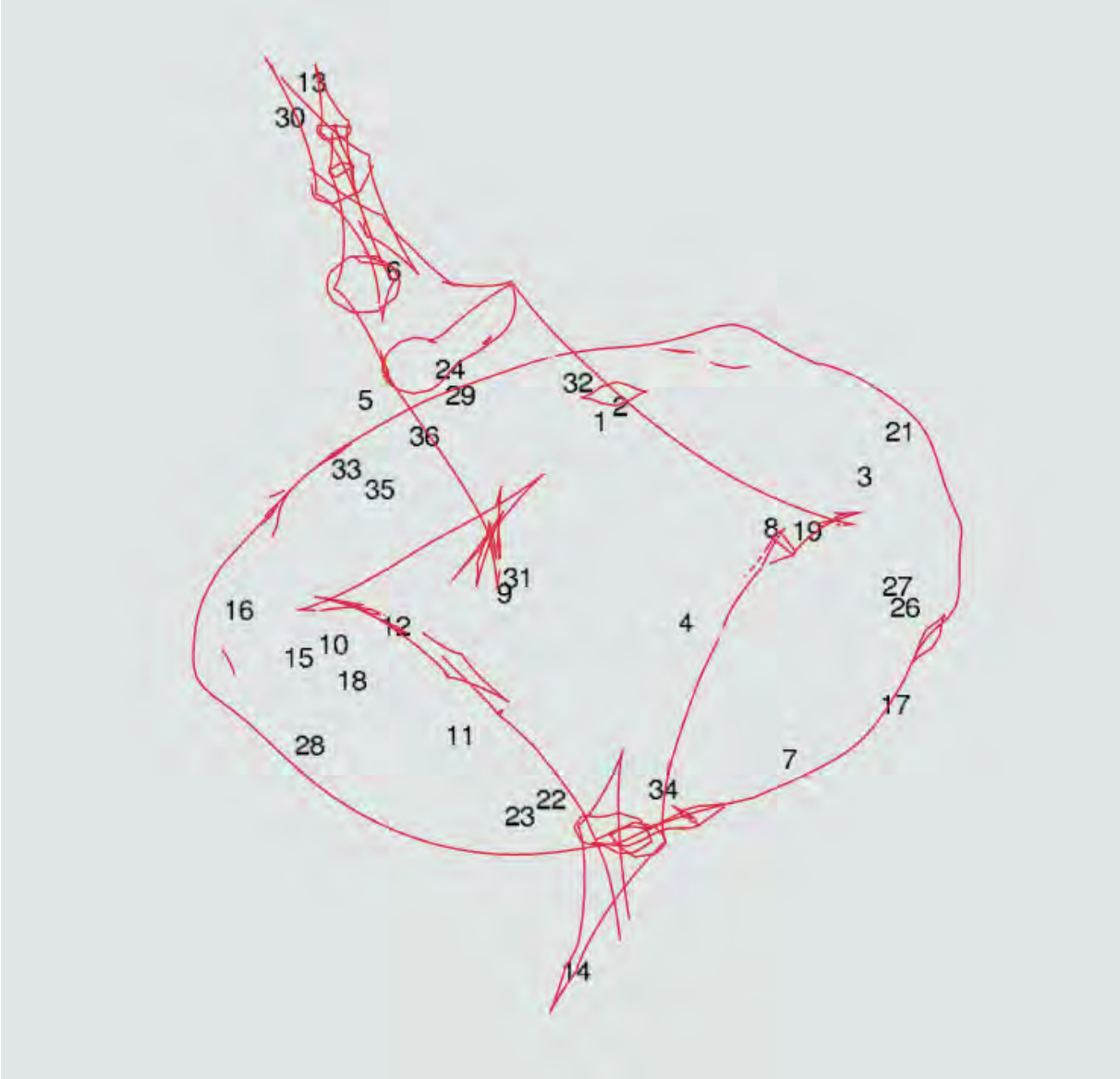

Figure 1.4: Caustic lines for Abell 1689 at $z = 1.83$ (Limousin et al., 2007).

line of sight is negligible and the deflection is governed by the mass distribution of the lens on the lens plane. The angular position of the image is determined by the deflection angle by

$$\theta = \beta + \frac{D_{LS}}{D_{OS}}\hat{\alpha}. \tag{1.2}$$

Deflection angle $\hat{\alpha}$ measures how deeply the light is bent by the lens. It depends on the perturbation of lens mass. According to general relativity, light travels on null geodesics with $\mathrm{d}\tau^2 = 0$ in Eq. 1.1. Combined with Fermat's principle, the deflection angle can be calculated as (Schneider et al., 1992)

$$\hat{\alpha}(\xi) = \int \mathrm{d}^2\xi' \frac{4G\Sigma(\xi')}{c^2}\frac{\xi - \xi'}{|\xi - \xi'|^2}, \tag{1.3}$$

where $\Sigma(\xi')$ represents the surface mass density. we define the characteristic length scale as $\xi_0 = 4\pi(\frac{\theta_v}{c})^2\, D_{OL}D_{LS}/D_{OS}$, with θ_v being the effective velocity dispersion. The corresponding length scale on the source plane is $\eta_0 = \xi_0 D_{OS}/D_{OL}$. Dimensionless vectors are $x = \xi/\xi_0$ and $y = \eta/\eta_0$. Then the lens equation 1.3 can be written as (Schneider et al., 1992)

$$y = x - \frac{D_{OL}D_{LS}}{\xi_0 D_{OS}}\hat{\alpha}(\xi). \tag{1.4}$$

When the image is strongly lensed and multiple images are observed, the surface mass density Σ must be larger than the critical mass density, which is defined as

$$\Sigma_{\mathrm{crit}} = \frac{c^2}{4\pi G}\frac{D_{OS}}{D_{LS}D_{OL}}. \tag{1.5}$$

The effect of gravitational lensing is described by the Jacobian matrix (Narayan & Bartelmann, 1996)

$$\mathcal{A}^{-1} \equiv \frac{\partial\theta}{\partial\beta} = \begin{pmatrix} 1-\kappa-\gamma_1 & -\gamma_2 \\ -\gamma_2 & 1-\kappa+\gamma_1 \end{pmatrix} = \mathcal{M}^{-1}, \tag{1.6}$$

with $\mathcal{M}$ the magnification tensor. Here $\kappa = \nabla^2\varphi/2 = \Sigma/\Sigma_{\mathrm{crit}}$ is convergence with $\nabla^2\varphi$ being the two-dimensional lensing potential. The shear vector γ is a complex number with $\gamma = (\gamma_1, \gamma_2)$. Hence, the magnification is

$$\mu = \det\mathcal{M} = \det\mathcal{A}^{-1} = (1-\kappa)^2\left(1 - \left(\frac{\gamma}{1-\kappa}\right)^2\right). \tag{1.7}$$

Here the magnification factor μ describes the ratio of the image area to the source area. The surface brightness of an image is preserved. The critical lines are collection of positions in the lens plane where it has infinite magnification. The corresponding lines in the source plane is caustic lines. Figures 1.3 and 1.4 show critical lines and caustic lines for cluster Abell 1689 (Limousin et al., 2007). When the observer, the lens and the source are perfectly aligned, the image of the source behaves like a ring. The Einstein radius is

$$\theta_E = \sqrt{\frac{4GM}{c^2}\frac{D_{LS}}{D_{OL}D_{OS}}}. \tag{1.8}$$

1.1.2 MASS DISTRIBUTION

The deflection angle Eq. 1.3 is determined by the surface mass distribution of the lens. Hence, the mass distribution of a cluster of galaxies is critical in gravitational lensing study. According to Newton's theorems, we may calculate the mass distribution of clusters:

Newton's first theorem If the body is a spherically symmetric shell, no net gravitational force is exerted by the shell on any object inside, regardless of the object's location within the shell.

Newton's second theorem A spherically symmetric body affects external objects gravitationally as though all of its mass were concentrated at a point at its center.

In general, the two-dimensional lensing potential is (Schneider et al., 1992)

$$\varphi(x) = \frac{1}{\pi}\int \ln|x-y|\frac{\Sigma(x)}{\Sigma_{\rm crit}}\mathrm{d}y, \tag{1.9}$$

with x and y are dimensionless vectors.

Singular isothermal sphere

The singular isothermal sphere (SIS) profile is the simplest model describing the mass distribution of an massive object, e.g., a galaxy or a cluster of galaxies. The model takes the components, e.g., stars as point mass and they behave like ideal gas. The gravitational potential is assumed to be spherical. With thermal equilibrium and hydrostatic equilibrium, the mass density is

$$\rho(r) = \frac{\sigma_v^2}{2\pi G}\frac{1}{r^2}, \tag{1.10}$$

with σ_v^2 being the velocity dispersion. Hence, the surface mass density is (Narayan & Bartelmann, 1996)

$$\Sigma(\xi) = \frac{\sigma_v^2}{2G\xi}, \tag{1.11}$$

and the Einstein radius from Eq. 1.8 is

$$\theta_E = 4\pi\frac{\sigma_v^2 D_{LS}}{c^2 D_{OS}} = \hat{\alpha}\frac{D_{LS}}{D_{OS}}. \tag{1.12}$$

The SIS profile has singularity at $\rho = 0$.

Dual Pseudo Isothermal Elliptical mass distribution

The dual Pseudo Isothermal Elliptical mass distribution (dPIE) (Elíasdóttir et al., 2007) is another way describing the mass distribution in gravitational lensing. The 3D spherical density distribution is

$$\rho(r) = \frac{\rho_0}{(1+r^2/a^2)(1+r^2/s^2)};\ s > a, \tag{1.13}$$

where ρ_0 is the central density, a is the core radius and s is the scale radius. In the center, the density $\rho \approx \rho_0/(1+r^2/a^2)$. In the region $r \in (a, s)$, $\rho \sim r^{-2}$ and at $r > s$, it has $\rho \sim r^{-4}$ (Elíasdóttir et al., 2007). The surface mass density is (Elíasdóttir et al., 2007)

$$\Sigma(R) = \Sigma_0 \frac{as}{s-a}\left(\frac{1}{\sqrt{a^2+R^2}} - \frac{1}{\sqrt{s^2+R^2}}\right), \tag{1.14}$$

with $\Sigma_0 = \pi\rho_0 sa/(s+a)$. Hence, the mass is (Elíasdóttir et al., 2007)

$$M(R) = 2\pi\Sigma_0 \frac{as}{s-a}\left(\sqrt{a^2+R^2} - a - \sqrt{s^2+R^2} + s\right). \tag{1.15}$$

The dPIE profile is used in modeling the mass distribution of Abell 2218 (Elíasdóttir et al., 2007).

Navarro-Frenk-White profile

The mass distribution of dark matter halos is usually in the Navarro-Frenk-White profile (NFW) (Navarro et al., 1996). It is a two-power density model. In general, for elliptical galaxies, the dark matter halos behave like

$$\rho(r) \propto \frac{\rho_0}{(r/a)^m(1+r/a)^{n-m}}, \tag{1.16}$$

with ρ_0 and a being the free parameters. When $(m, n) = (1, 3)$, the model is called the NFW model. The mass of NFW profile is (Binney & Tremaine, 2008)

$$M(r) = 4\pi\rho_0 a^3\left(\ln\left(1+\frac{r}{a}\right) - \frac{r}{a+r}\right). \tag{1.17}$$

1.1.3 TIME DELAY

In strong gravitational lensing, light rays are bent and light paths are different. The time between the light is emitted by the source and the light reaches the observer is called arrival time. Light along different paths produces different arrival times. The arrival time is

$$\tau(x, y) = \frac{\xi_0^2}{c}\frac{D_{OS}}{D_{OL}D_{LS}}(1+z)\left(\frac{(x-y)^2}{2} - \varphi(x)\right), \tag{1.18}$$

where z is the lens redshift. The difference between the arrival times of multiple images is time delay. There are two effects contributing to the time delay. The geometrical time delay is caused by the bent light path. The potential of the gravitational field contributes to the potential time delay (Schneider et al., 1992). A geometrical time delay is

$$c\Delta t_{\rm geom} = (1+z)\frac{D_{OL}D_{OS}}{2D_{LS}}(\theta-\beta)^2, \tag{1.19}$$

while a potential time delay is calculated as

$$c\Delta t_{\rm poten} = -(1+z)\hat{\varphi}(\xi) + \text{const}, \tag{1.20}$$

Figure 1.5: A map of arrival time on the image plane with *Lenstool*.

with $\hat{\varphi}(\xi) = D_{OS}\xi_0^2\ \varphi/D_{OL}D_{LS}$. A time delay is a combination of a geometrical time delay and a potential time delay

$$\Delta t = \Delta t_{\rm geom} + \Delta t_{\rm poten}, \tag{1.21}$$

So time delay can be calculated as (Schneider et al., 1992)

$$c\Delta t(x,y) = \frac{D_{OL}D_{OS}}{2cD_{LS}}\left[(x-\xi)^2 + (y-\eta)^2 - 2\phi(x-y)\right], \tag{1.22}$$

where $\phi(x-y)$ is the Fermat potential with $\phi(x-y) = (x-y)^2/2 - \varphi(x-y)$. With *Lenstool* Jullo et al. (2007), a map of arrival time is produced in Figure 1.5. The lens is Abell 1689. The source is located at $z = 3$.

1.2 SUPERNOVAE

Supernovae (SNe) are stellar explosions that emit energy and materials into nearby interstellar space. SN explosion is energetic that it can be as bright as a whole galaxy. SN is a primary source of heavy elements in the universe. Figure 1.6 shows a SNe remnant.

1.2.1 BRIEF INTRODUCTION

A classification of SNe is based on their spectra (Smartt, 2009).

Type I SNe There is no emission or absorption of H in their spectra. **Type Ia SNe (SNe Ia)** have Si absorption line in the spectra. **SNe Ib** (**SNe Ic**) show a presence (absence) of He in the spectra.

Type II SNe They show strong H lines. Among them, a subclass of Type II SNe with a plateau phase after peak luminosity in their light curves are **II-P SNe**, while **II-L SNe** exhibit a decay after peak luminosity.

Based on the progenitor mechanism, all SNe Ib, SNe Ic and Type II SNe are core-collapse SNe. Figure 1.7 shows a diagram of classification mentioned above.

1.2.2 PROGENITOR MODELS

SN Ia comes from the thermonuclear explosion of white dwarf (WD). A WD is a low luminous but hot stellar remnant. They are very dense, whose mass can be comparable to the Sun and radius are in earth-size. Because of its high density, in a stable WD core, the electron degeneracy pressure is balanced to the gravitational force to resist the star from collapsing. The maximum mass of a stable WD is $\sim 1.39\ M_\odot$. This is called the Chandrasekhar limit. If a WD's mass is above the Chandrasekhar limit, e.g., by accretion from its companion star or merge of two WDs, the electron degeneracy pressure can no longer resist to the gravitational force, and the WD will undergo further collapse.

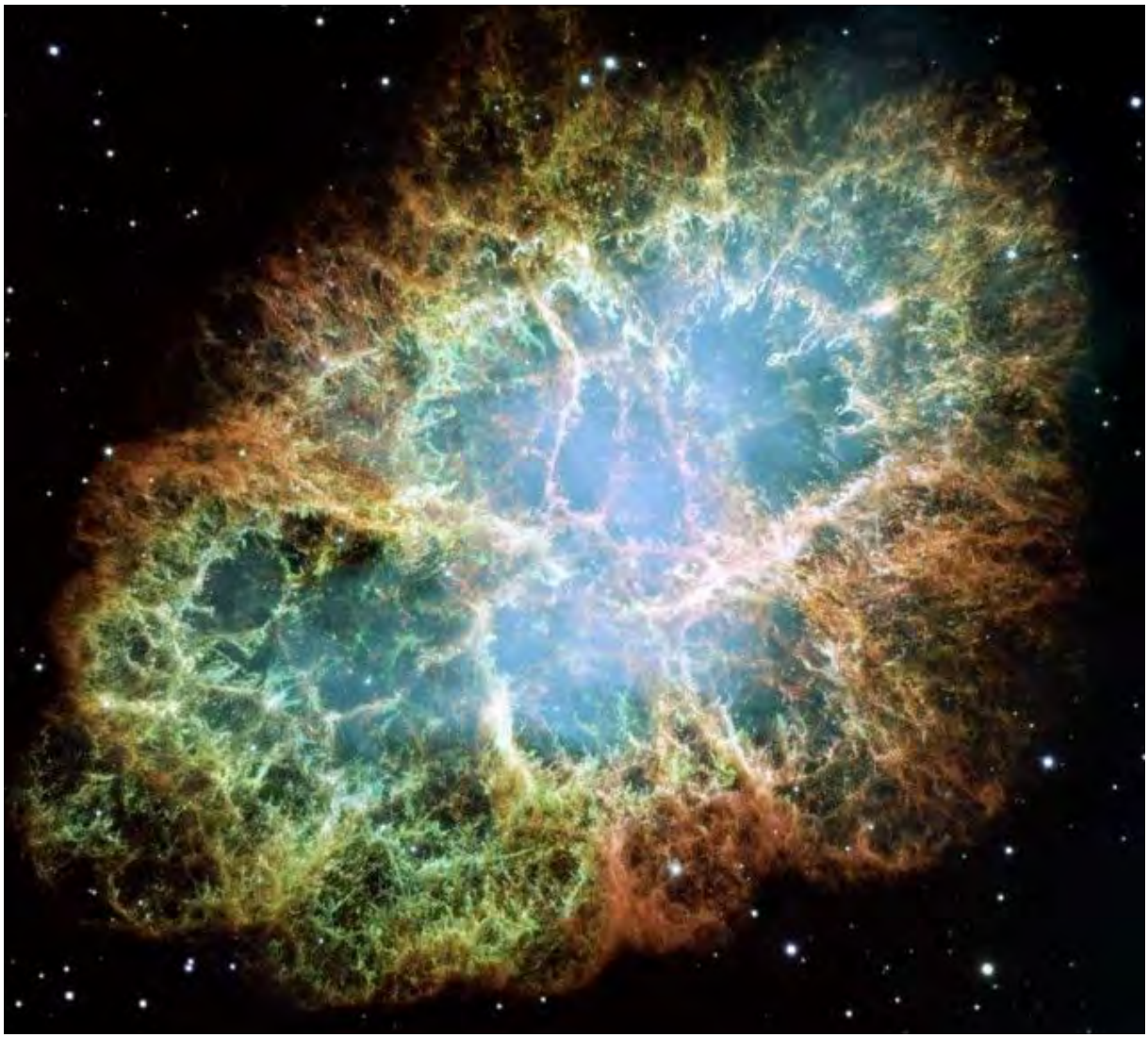

Figure 1.6: The crab supernova remnant, photoed by Hubble Space Telescope (2005). It is a supernova remnant in the constellation of Taurus.

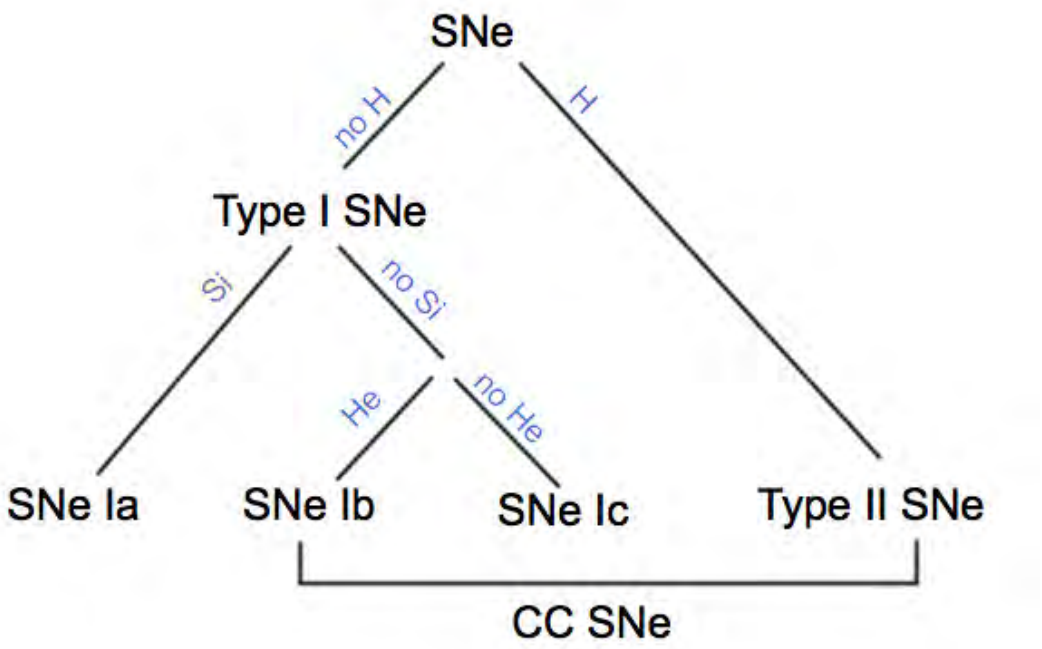

Figure 1.7: Classification of SNe.

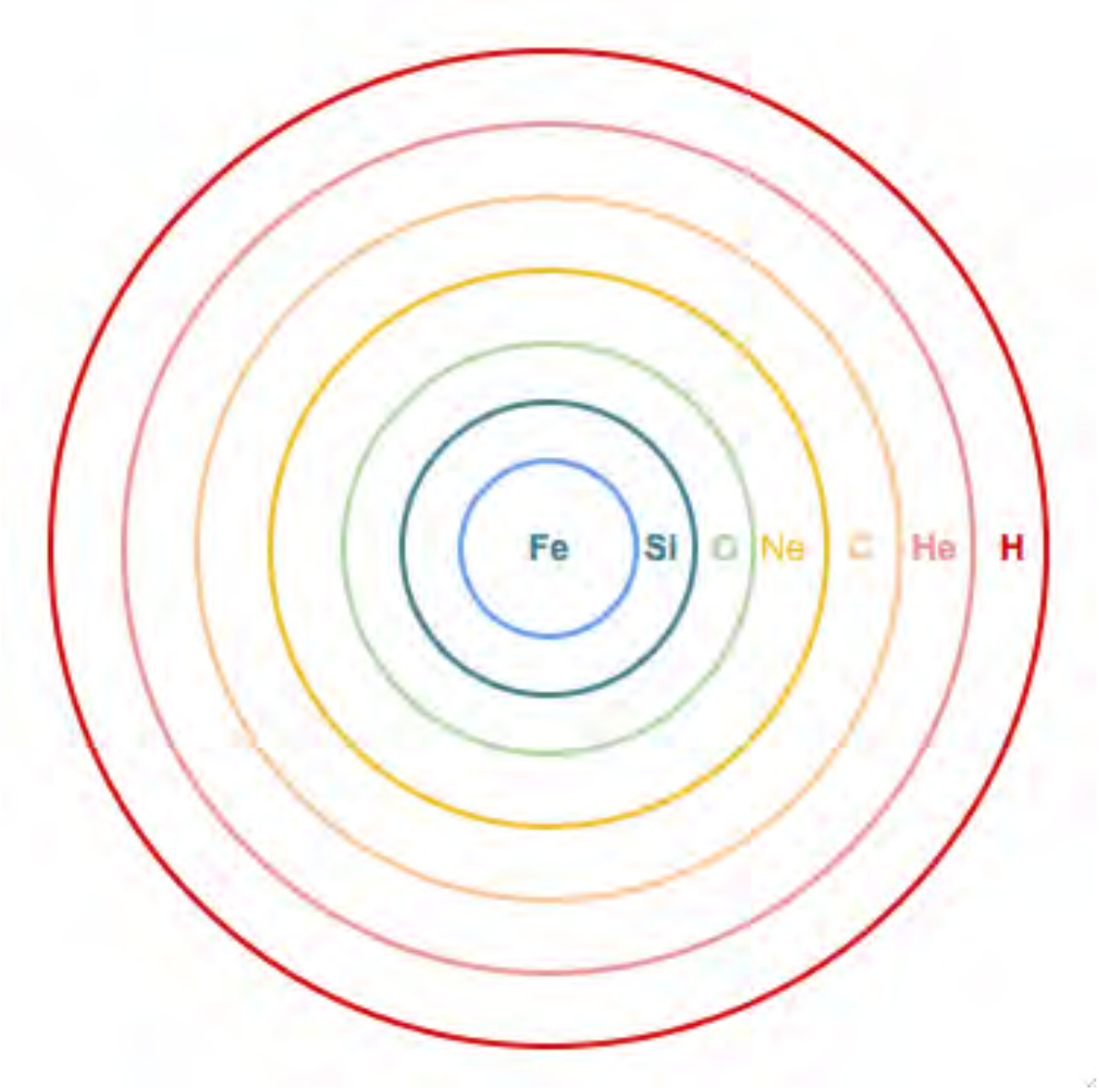

Figure 1.8: A schematic onion-like layers of a massive star before core collapse.

There are some models to explain the SN progenitor scenarios so far. But the progenitor picture of SNe Ia are somehow uncertain. For SNe Ia, there are three major progenitor models. In the single degenerate (SD) model (Whelan & Iben, 1973), a carbon-oxygen WD accretes mass from a non-degenerate stellar companion, e.g., a red giant, a main sequent star, a subgiant and etc, and gains mass up to the Chandrasekhar limit, which results in a thermonuclear explosion. A double degenerate (DD) model (Webbink, 1984) has two WDs merging to approach the Chandrasekhar mass limit. The third scenario (Bildsten et al., 2007; Fink et al., 2007; Guillochon et al., 2010) describes the explosion with detonation. In a double WD system, the detonation ignites the He shell of one WD, then the shock waves reaches the other WD and another detonation begins.

But any progenitor model has their problems either in theory and/or in observation (Maoz & Mannucci, 2011). SD model allows only a narrow range of mass accretion rate to guarantee stable hydrogen burning. Too low or too high rate will lead to a nova event or a red-giant-like expansion. An explanation to solving this problem is that the accretion is regulated by strong winds from the accreting WD (Hachisu et al., 1999). But this wind-regulation picture is conflict with the observed results (Badenes et al., 2007; Leonard, 2007). Whether or not the wind-regulation is effective is still under debate (Kobayashi & Nomoto, 2009). The DD model has been questioned as well. The merging of two massive carbon-oxygen degenerate dwarfs will lead to the formation of neutron star and ignite an explosion of a CC SN instead of SN Ia (Darbha et al., 2010; Guerrero et al., 2004; Nomoto & Iben, 1985; Shen et al., 2012).

The CC SNe are formed by massive stars heavier than $\sim 8M_{\odot}$ (Smartt, 2009). Hydrogen is converted to helium, and then helium is burning, which leads to a carbon-oxygen core. If the star is massive, it may provide enough temperature and pressure to fuse carbon and oxygen at the end of helium burning. Hence the core of the star becomes onion-like with heavier elements being accumulated in the center. This burning stage may circulate up to iron since iron has highest binding energy per nucleon, so by iron fusion, energy cannot be produced. When there is no further fusion reaction to keep the high temperature, the gravitational pressure exceeds the electron degeneracy pressure, and the core collapses inwards rapidly. As the density of the core increases, electrons is merged into proton to form neutrons. The outer core falls due to the shrink . The collapse happens so quickly to leave the outer layers suspend above the core. When the collapse ends by the neutron degeneracy, and the outer core rebounds and a shock wave is produced. As the shock wave expands, the supernova explosion starts. Depending on the mass of the star, the remnant may be a neutron star ($M < 20\,M_{\odot}$) or a black hole ($20M_{\odot} < M < 50M_{\odot}$). A more massive star with $M > 50M_{\odot}$ will collapse to a black hole without SN explosion.

1.2.3 SNe Ia as standard candles

SNe Ia shine the deep sky when they explode, while the research on SNe Ia shines our knowledge on the universe and also wins a shining Nobel prize medal.

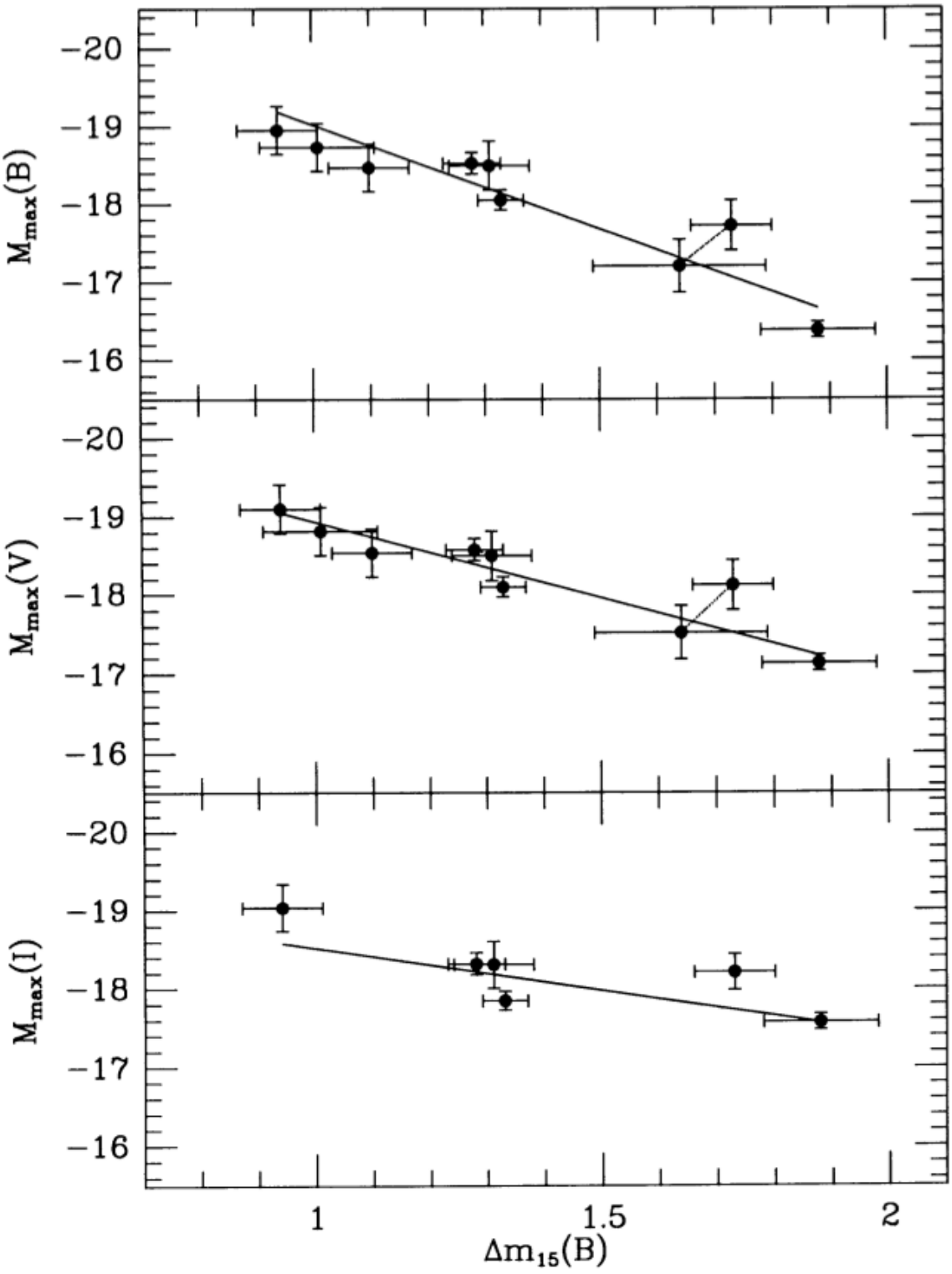

Figure 1.9: Phillips relation of SNe Ia. Δm_{15} represents the decline of the light curves in magnitude 15 days since it reaches the peak brightness (Phillips, 1993).

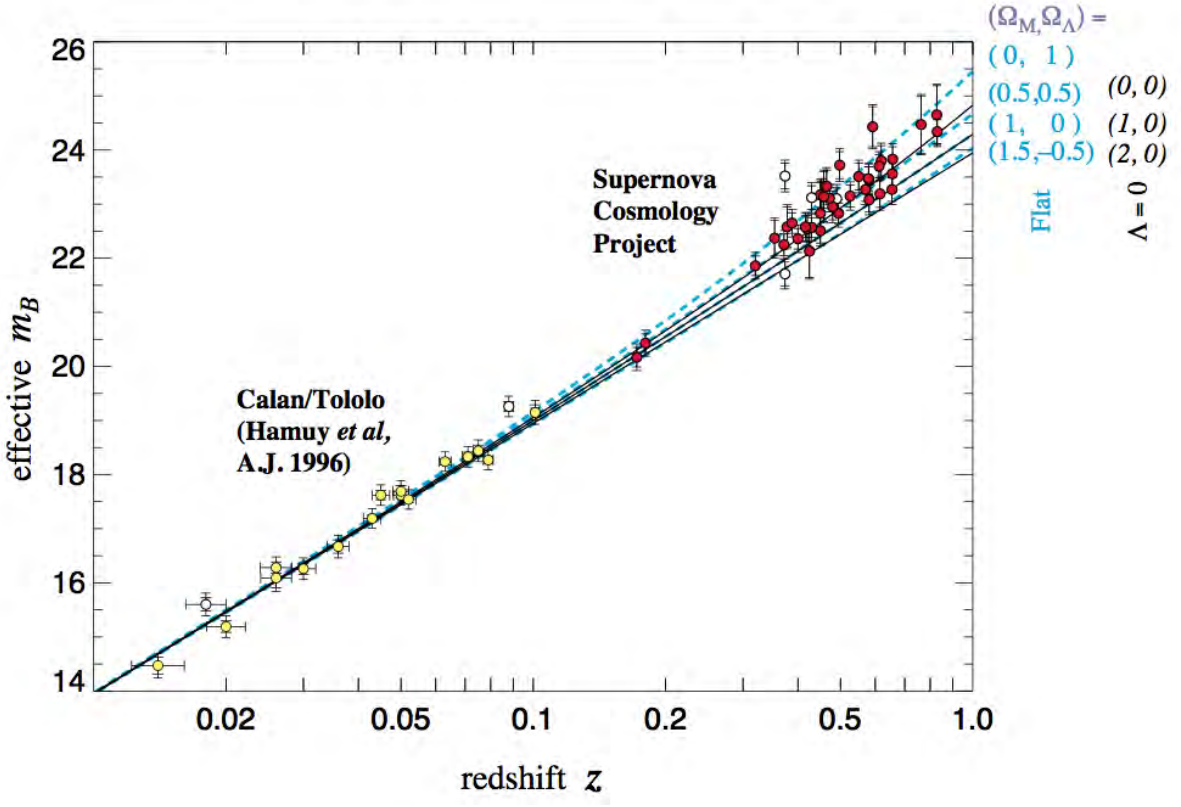

Figure 1.10: Hubble diagram with 42 SNe Ia (Perlmutter et al., 1999).

Figure 1.11: Artist's image of a GRB from wikipedia.

In 2011, the Nobel Prize in Physics was awarded to Saul Perlmutter, Brian P. Schmidt and Adam G. Riess "for the discovery of the accelerating expansion of the Universe through observations of distant supernovae". They used SNe Ia to measure the cosmic distance with the help of light curves (LCs) of SNe Ia, whose peak magnitudes are strongly correlated with LC width. This relation is so-called the Phillips relation (Phillips, 1993), as shown in Figure 1.9. After correcting the peak magnitudes of SNe Ia due to the Phillips relation, the corrected peak magnitudes are uniform and SNe Ia can be used as standard candles. Figure 1.10 shows the Hubble diagram with SNe Ia (Perlmutter et al., 1999). With the Hubble diagram, we can constrain the the matter density parameters Ω_m and Ω_Λ.

1.2.4 GRB-SNE

Discovered by Vela series of military Satellites (Klebesadel et al., 1973), Gamma-ray bursts (GRBs) are energetic explosions with narrow beams of flashes of gamma rays. They are the most luminous phenomena in the universe. Energies of gamma-ray photons may be up to some GeV. The duration of the bursts less than 2 seconds is classified as short GRBs, and those last longer than 2 seconds are called long GRBs. GRB is thought to be triggered

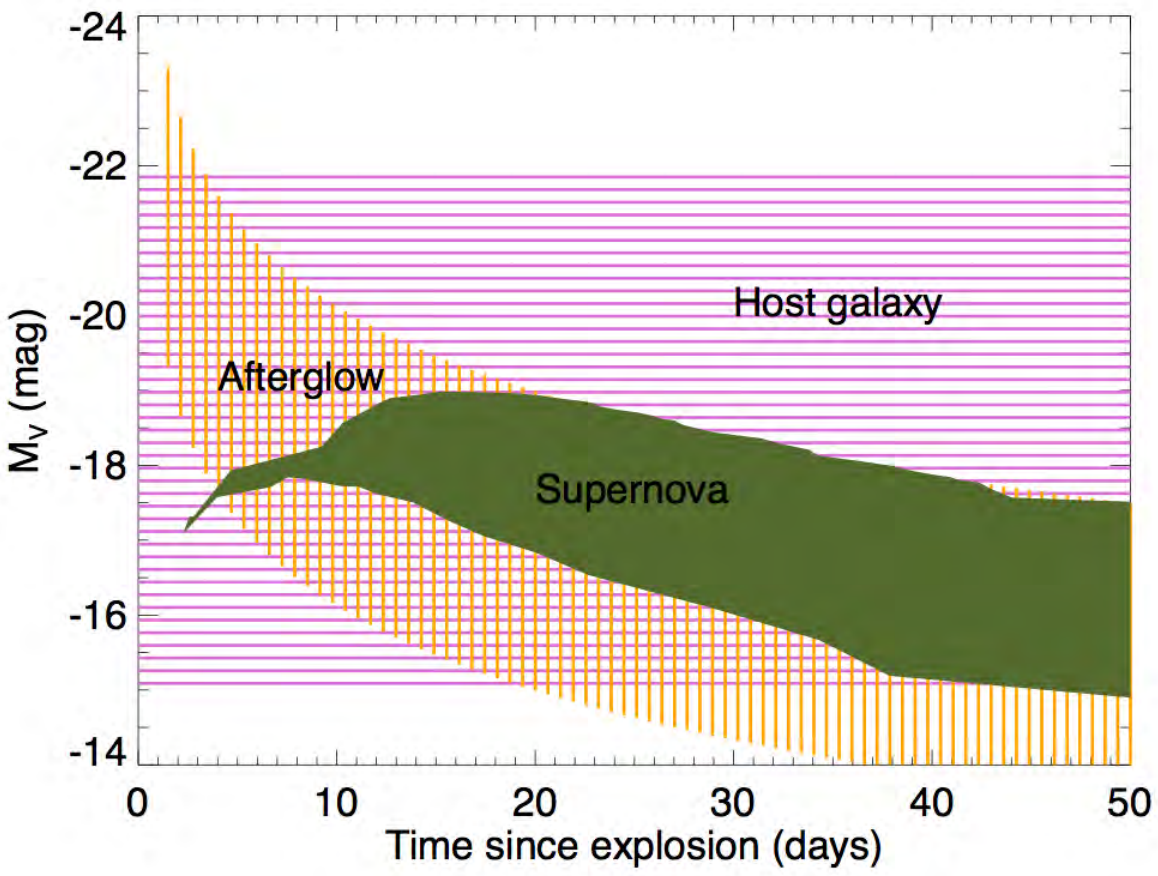

Figure 1.12: A diagram of light curve of GRB-SN (Hjorth, 2013). A bright afterglow or host galaxy may contaminate the luminosity of a GRB-SN.

by a collapse of a massive star forming a neutron star or a black hole. They are associated with supernova explosions. Figure 1.11 shows an image of a GRB.

Supernovae associated with GRBs are Type Ibc SNe (SNe Ibc), whose spectra lack hydrogen line but show weak silicon line. A collapsar model provides a theoretical explanation to the connection between GRBs and SNe (MacFadyen & Woosley, 1999; MacFadyen et al., 2001). But the there are some questions still under debate, e.g., the progenitor scenario of GRBs, the distinct properties of long and short GRBs, etc. A crucial key to solve these and other relevant questions are the light curves of GRB-SNe. But their light curves are not easy to get. A schematic diagram is shown in Figure 1.12 (Hjorth, 2013). An afterglows of GRB decays rapidly, but considering its high energy, if it is still bright enough after a few days since the burst, the associated SN may not be able to be observed. SNe Ibc are form in star-forming and dust-rich galaxies. Host galaxy may conceal a GRB-SN to be discovered. In addition, dust in the Milky Way and the host region may also prevent a SN light to be seen.

1.3 COSMOLOGY

The standard candles of SNe Ia and GRB-SNe can be used measure the cosmological distance (Li & Hjorth, 2014; Li et al., 2014; Perlmutter et al., 1997, 1999; Riess et al., 1998), hence they can be used to constrain the matter density parameters Ω_m and Ω_Λ. In this Section, we briefly introduce some basic concepts of cosmology.

1.3.1 COSMOLOGICAL PARAMETERS

The expansion of the universe can be expressed as

$$l(t) \propto a(t), \tag{1.23}$$

where $l(t)$ represents the distance and $a(t)$ is the scale factor. When Hubble parameter H is involved, the scale factor can be written as

$$H = \frac{\dot{a}}{a}. \tag{1.24}$$

Derived from Einstein's field equation, the Friedmann equation, describing the expansion of a homogeneous and isotropic universe, is written as (Peebles & Ratra, 2003)

$$\left(\frac{\ddot{a}}{a}\right)^2 = H_0^2 \left(\Omega_{M0}(1+z)^3 + \Omega_{R0}(1+z)^4 + \Omega_{\Lambda 0} + \Omega_{K0}(1+z)^2\right), \tag{1.25}$$

where H_0 is Hubble's constant, and the dimensionless density parameters $\Omega_{i0} = 8\pi G\rho_{i,0}/(3H_0^2)$, with $\rho_{i,0}$ being the mass density. ρ_{M0} denotes the present mass density of nonrelativistic matter, ρ_{R0} represents the present mass in the thermal cosmic microwave background (CMB), $\rho_{\Lambda 0}$ is a measure of present dark energy, and ρ_{K0} describes the curvature of the universe. The sum of the density parameters satisfies

$$\Omega_{M0} + \Omega_{R0} + \Omega_{\Lambda 0} + \Omega_{K0} = 1. \tag{1.26}$$

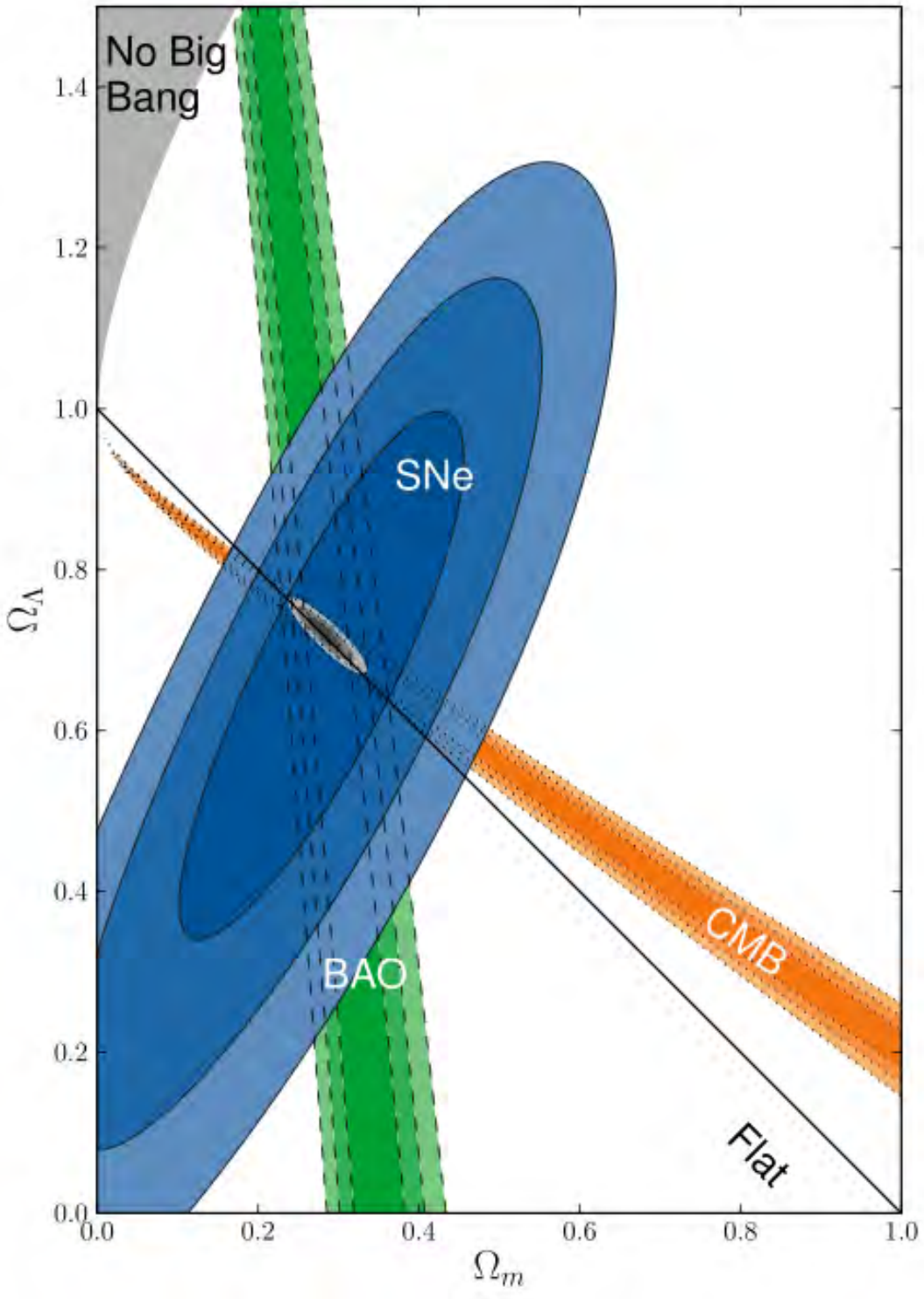

Figure 1.13: Combined results of constraint on Ω_M and Ω_Λ in ΛCDM model (Suzuki et al., 2012).

In a flat universe, $\Omega_M + \Omega_\Lambda = 1$. Derived from general relativity, a standard as well as simple model, so-called ΛCDM model is developed, in which a cosmological constant (Λ) is associated with dark energy and cold dark matter. Figure 1.13 shows a recent result of constraint on density parameters Ω_M and Ω_Λ (Suzuki et al., 2012) in ΛCDM model. It is a combined result with SNe Ia (Suzuki et al., 2012), CMB (Dunkley et al., 2009; Komatsu et al., 2011) and baryon acoustic oscillations (BAO; Eisenstein et al., 2005; Percival et al., 2010). In 2013, *Planck* measurement gives the matter density parameter $\Omega_M = 0.315 \pm 0.017$ (Planck Collaboration et al., 2013) with CMB temperature survey.

1.3.2 COSMOLOGICAL DISTANCE

The universe is expanding at an increasing rate. The presence of mass in the universe changes the curvature of the universe. The cosmological distance measurement is based on general relativity.

Light travels at the speed of c, and the Hubble distance D_H is defined as (Hogg, 1999)

$$D_H = \frac{c}{H_0}. \tag{1.27}$$

The line-of-sight comoving distance D_C is the distance between two points measured along a path defined at the present cosmological time, which is also the distance that we would measure locally between the events if two points were moving with the Hubble flow,

$$D_C = D_H \int_0^z \frac{\mathrm{d}z'}{E(z')}, \tag{1.28}$$

where $E(z)$ is a function of cosmological parameters with (Hogg, 1999)

$$E(z) = \sqrt{\Omega_m(1+z)^3 + \Omega_K(1+z)^2 + \Omega_\Lambda}. \tag{1.29}$$

The transverse comoving distance is defined as

$$D_\mathrm{M} = \begin{cases} D_\mathrm{H} \frac{1}{\sqrt{\Omega_k}} \sinh\left[\sqrt{\Omega_k}\, D_\mathrm{C}/D_\mathrm{H}\right] & \text{for } \Omega_k > 0 \\ D_\mathrm{C} & \text{for } \Omega_k = 0 \\ D_\mathrm{H} \frac{1}{\sqrt{|\Omega_k|}} \sin\left[\sqrt{|\Omega_k|}\, D_\mathrm{C}/D_\mathrm{H}\right] & \text{for } \Omega_k < 0. \end{cases} \tag{1.30}$$

The angular diameter distance, which is commonly used in gravitational lensing, is calculated as

$$D_A = \frac{D_M}{1+z}, \tag{1.31}$$

and the luminosity distance is

$$D_L = (1+z) D_M. \tag{1.32}$$

With the luminosity distance, the distance modulus in the conversion between the apparent magnitude and the absolute magnitude is

$$DM = 5 \log\left(\frac{D_L}{10\ \mathrm{pc}}\right). \tag{1.33}$$

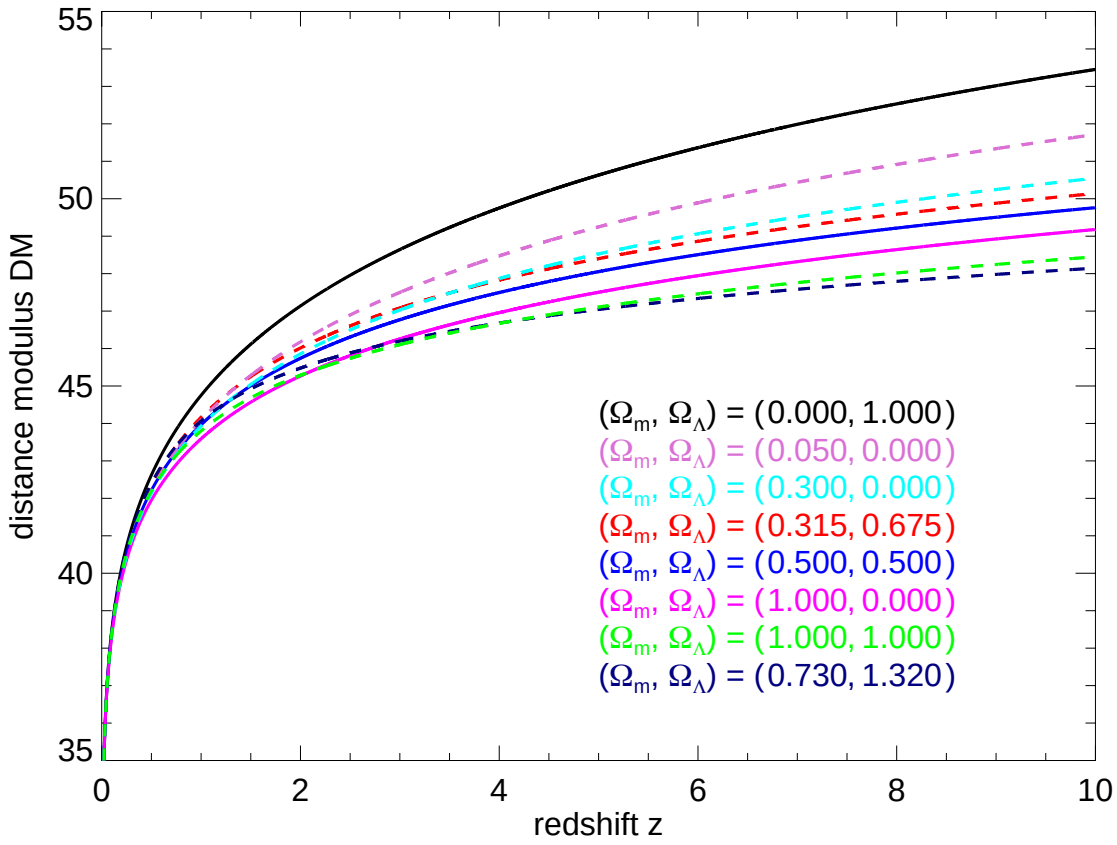

Figure 1.14: The distance modulus at different cosmological models with z up to 10. The solid lines show DM in flat universe with $\Omega_M + \Omega_\Lambda = 1$, while dash lines are in curved space. Here $H_0 = 67.3$ km s^{-1} Mpc^{-1} (Planck Collaboration et al., 2013).

Figure 1.14 shows the distance modulus in different cosmological models with different Ω_M and Ω_Λ. Different estimates of the matter density parameters have the distance modulus curves. This is why we want to constrain the parameters Ω_M and Ω_Λ, and trace the evolution history of the universe.

2

GRAVITATIONAL LENSING AND SUPERNOVAE

I was like a boy
playing on the sea-shore,
and diverting myself now and then
finding a smoother pebble or a prettier shell than ordinary,
whilst the great ocean of truth lay all undiscovered before me.
Isaac Newton

Abstract -
Time delays of gravitationally lensed sources can be used to constrain the mass model of a deflector and determine cosmological parameters. We here present an analysis of the time-delay distribution of multiply imaged sources behind 17 strong lensing galaxy clusters with well-calibrated mass models. We find that for time delays less than 1000 days, at $z = 3.0$, their logarithmic probability distribution functions are well represented by $P(\log \Delta t) = 5.3 \times 10^{-4} \Delta t^{\widetilde{\beta}} / M_{250}^{2\widetilde{\beta}}$, with $\widetilde{\beta} = 0.77$, where M_{250} is the projected cluster mass inside 250 kpc (in $10^{14} M_{\odot}$), and $\widetilde{\beta}$ is the power-law slope of the distribution. The resultant probability distribution function enables us to estimate the time-delay distribution in a lensing cluster of known mass. For a cluster with $M_{250} = 2 \times 10^{14} M_{\odot}$, the fraction of time delays less than 1000 days is approximately 3%. Taking Abell 1689 as an example, its dark halo and brightest galaxies, with central velocity dispersions $\sigma \geqslant 500$ km s^{-1}, mainly produce large time delays, while galaxy-scale mass clumps are responsible for generating smaller time delays. We estimate the probability of observing multiple images of a supernova in the known images of Abell 1689. A two-component model of estimating the supernova rate is applied in this work. For a magnitude threshold of $m_{AB} = 26.5$, the yearly rate of Type Ia (core-collapse) supernovae with time delays less than 1000 days is 0.004 ± 0.002 (0.029 ± 0.001). If the

Published as: Xue Li, Jens Hjorth, Johan Richard – *The rates and time-delay distribution of multiply imaged supernovae behind lensing clusters*, Journal of Cosmology and Astroparticle Physics, Issue 11, article id. 015 (2012).

magnitude threshold is lowered to $m_{AB} \sim 27.0$*, the rate of core-collapse supernovae suitable for time delay observation is* 0.044 ± 0.015 *per year.*

2.1 INTRODUCTION

An object in our universe, such as a galaxy or a galaxy cluster, could bend light rays passing it and act as a lens to magnify or demagnify sources behind it (Zwicky, 1937). This effect is known as gravitational lensing and has been developed into a powerful cosmological tool in recent decades (Cooke & Kantowski, 1975) (Blandford & Narayan, 1992) (Efstathiou et al., 1990) (Kneib & Natarajan, 2011). With the help of gravitational lensing, we can observe distant galaxies behind galaxy clusters which would otherwise be too faint to be observed, and analyze their properties. We can also measure the cosmological parameters that describe the geometry and the expansion rate of the universe (Refsdal, 1964) (Jullo et al., 2010). In addition, we can analyze the total mass distribution in lensing galaxy clusters (Kochanek & Schechter, 2004), regardless of the differences between luminous and dark matter (Massey et al., 2010).

In strong gravitational lensing systems, multiple images are produced. Light travels along the stationary paths between two points in space time. A massive object, like a galaxy or cluster of galaxies located along the light path, in general affects and perturbs the light trajectory (Schneider et al., 1992). When lensed by a galaxy or a cluster of galaxies, light emitted by a source may travel along different light paths and be observed as different multiple images. Light from these images is received at different times. Thus, multiple images have different arrival times to the observer. The difference of arrival times between multiple images of the same source is called the time delay.

So far, time delays have been studied and applied in many ways: to constrain the Hubble parameter H_0 (Saha et al., 2006) (Paraficz & Hjorth, 2010) (Suyu et al., 2012); to study the galaxy mass profile with Monte Carlo simulations (Rusin, 2000); to measure the cosmological parameter w (Paraficz & Hjorth, 2009) (Coe & Moustakas, 2009) (Suyu et al., 2010) (Linder, 2011) (Suyu et al., 2012); to improve the mass models of galaxies with the time delays of quasars (Goicoechea & Shalyapin, 2010).

Compared to quasars, light curves of type Ia supernovae (SNe Ia) evolve regularly with time, and have been extensively studied (Hamuy et al., 1996) (Hillebrandt & Niemeyer, 2000). Hence, they are potentially very useful as standard sources for constraining time delays in gravitational lens systems. In principle, they can also be used to constrain the Hubble constant through the measurement of the time delays (Oguri & Kawano, 2003). SNe Ia play a key role as standard candles in distance measurements on cosmological scales. Supernovae provide direct evidence that the low-redshift universe is accelerating (Riess et al., 1998) (Perlmutter et al., 1999) (Nordin et al., 2011). They act as the primary sources of heavy elements and potentially dust in the universe (Gall et al., 2011). However, there is still debate on the progenitor models of SNe Ia (Hillebrandt & Niemeyer, 2000) (Maoz & Mannucci, 2011). There are two major progenitor scenarios to explain the mechanism of Type Ia progenitor. In the single degenerate model (Whelan & Iben, 1973),

a carbon-oxygen white dwarf accretes mass from a companion star, a subgiant, a helium star or a red giant, and reaches the Chandrasekhar mass limit, resulting in a thermonuclear explosion (Hoyle & Fowler, 1960) (Branch et al., 1995). In the double degenerate scenario (Webbink, 1984), two white dwarfs merge, approach the Chandrasekhar mass limit, and ignite. Recently, a third model gives another explanation of the possible SN progenitor scenarios. Instead of accreting the mass to the Chandrasekhar mass limit, the detonation ignites to the accreted He shell of one white dwarf, then the detonation shock wave comes to the core or near the center, and a second detonation happens (Fink et al., 2007) (Bildsten et al., 2007) (Guillochon et al., 2010).

The rate of supernovae (SNR) reflect their formation mechanism. For example, core-collapse SNe (Type II and Ibc supernovae) arising from massive stars help us trace the star formation and may be used to constrain the star formation rate (SFR) (Anderson et al., 2011). A well established model of estimating the SNR for Ia SNe ($\mathrm{SNR_{Ia}}$) is a "two-component" model (Scannapieco & Bildsten, 2005) (Mannucci et al., 2005) (Sullivan et al., 2006), with one component dependent on the recent star formation in the host galaxy and the other component dependent on the host stellar mass. The SN type Ia rate is a combination of these two components. The $\mathrm{SNR_{Ia}}$ at intermediate redshift has been constrained using the SDSS-II dataset to $z \leqslant 0.12$ (Dilday et al., 2008), and extended analysis to $z < 0.3$ (Dilday et al., 2010). At high redshift, the SN Ia rate is also tested and constrained, using the SNLS dataset to $z \approx 0.5$ (Neill et al., 2006) and $0.1 \leq z \leq 1.1$ (Perrett et al., 2012), the *HST*/GOODS survey up to $z < 1.8$ (Dahlen et al., 2004) (Dahlen et al., 2008), and the Subaru Deep Field (SDF) to $z < 2$ (Graur et al., 2011). The core-collapse supernova rate is also tested and estimated up to $z \sim 0.7$, using the GOODS survey. With these data and the SNR model, we can estimate the lensed SNR in a cluster lensing system (Riehm et al., 2011).

The aim of this paper is to (1) develop a general function to describe the time-delay distributions in gravitational lensing systems; (2) estimate the lensed SNR as a function of time delay and magnitude in Abell 1689 to assess the feasibility of constraining mass models and cosmological parameters with lensed supernovae observationally.

The outline of the paper is as follows. In section 2.2, we develop a theoretical formalism for describing the time-delay distribution. The analysis and discussion of parameters for the distribution function are developed in section 2.3. In section 2.4, we model time-delay distributions of 17 massive lensing clusters. We analyze and fit the parameters of the distribution function, based on the results from modeling. In section 2.5, using the "two-component" model, we calculate the probability of observing supernovae in 35 known multiply imaged galaxies behind Abell 1689. Finally, we summarize our investigation and discuss future prospects in section 2.6. Throughout this paper, we assume a cosmological model with $\Omega_m = 0.3, \Omega_\Lambda = 0.7, h = 0.7$. Magnitudes are in the AB system.

2.2 TIME DELAY THEORY

A light ray is deflected when it passes a cosmic massive object. In a lensing system, the light path from the source to the observer is changed according to the gravitational field near the lens. In the case of a multiple image system, lensing generally causes a difference in the arrival time of a galaxy image pair and hence generates a time delay. The time delay, Δt, can be calculated as (Schneider et al., 1992)

$$c\Delta t(y) = \xi_0^2 \frac{D_{\rm OS}}{D_{\rm OL} D_{\rm LS}} (1+z_L)[\phi(x_1,y) - \phi(x_2,y)], \tag{2.1}$$

where $\xi_0 = 4\pi(\frac{\sigma_v}{c})^2 \frac{D_{\rm OL} D_{\rm LS}}{D_{\rm OS}}$ is the characteristic length scale in the lens plane. Here σ_v is the value of an effective velocity dispersion, $D_{\rm OS}$ is the angular diameter distance between the observer and the source, $D_{\rm OL}$ is the angular diameter distance between the observer and the lens, $D_{\rm LS}$ is the angular diameter distance between the lens and the source, and z_L is the lens redshift. We denote the image position in the lens plane by $\boldsymbol{\xi}$ and the source position in the source plane by $\boldsymbol{\eta}$. Here $y = |\boldsymbol{\eta}|/\eta_0$, is the source position in the source plane, with $\eta_0 = \frac{\xi_0 D_{\rm OS}}{D_{\rm OL}}$ being the maximal distance to the caustic line. We define $x_i (i = 1, 2)$ as two image positions in the lens plane with $x = |\boldsymbol{\xi}|/\xi_0$. Here x, y are dimensionless vectors. The Fermat potential is defined as $\phi(x_i, y)(i = 1, 2)$. For a two-image system, the larger the difference of their Fermat potentials, the larger time delay they will generate. The Fermat potential $\phi(x, y)$ can also be described by the lensing potential $\varphi(x)$ (Narayan & Bartelmann, 1996),

$$\phi(x,y) = \frac{(x-y)^2}{2} - \varphi(x). \tag{2.2}$$

We assume spherically symmetric lenses in what follows.

Generally, for a lens with density distribution $\rho \propto r^{-\delta}$, the time delay can be expanded as (Kochanek & Schechter, 2004) (Witt et al., 2000)

$$\Delta t(\delta) \approx (\delta - 1)\Delta t_{\rm SIS} \left[1 - \frac{(2-\delta)^2}{12} \left(\frac{\Delta r}{\langle r \rangle} \right)^2 \cdots \right], \tag{2.3}$$

where $\Delta t_{\rm SIS}$ represents the time delay for the Singular Isothermal Sphere (SIS; $\delta = 2$), and $\langle r \rangle = (r_i + r_j)/2$. If the term $\frac{\Delta r}{\langle r \rangle}$ is small, the higher order terms can be ignored.

For real clusters, tidal perturbations from objects near the lens or along the line of sight (Keeton et al., 1997) (Witt & Mao, 1997) may affect the images as well. An external shear can be added to the lens (Witt et al., 2000), whose potential is

$$\phi(\gamma) = -\frac{1}{2}[\gamma_1(\zeta_1^2 - \zeta_2^2) + 2\gamma_2\zeta_1\zeta_2], \tag{2.4}$$

where γ is the strength of the shear, $\gamma_1 = \gamma \cos 2\theta_\gamma$ and $\gamma_2 = \gamma \sin 2\theta_\gamma$, with θ_γ being the angle between the direction of the shear and the major axis of the lens. Here ζ_1, ζ_2 represent the components of the lens coordinate. Then more than 2 multiple images may

be produced by each source, and the time delay between images i and j is (Witt et al., 2000)

$$c\Delta t = \frac{D_{\rm OL}D_{\rm OS}}{2D_{\rm LS}}(1+z_L)\{(r_j^2-r_i^2)+\gamma[r_j^2\cos 2(\theta_j-\theta_\gamma)-r_i^2\cos 2(\theta_i-\theta_\gamma)]\}, \tag{2.5}$$

where $r_k=(\zeta_k^2+\zeta_k^2)^{1/2}$ with $k=i,j$ is the distance of the image from the center. The shear affects the time delay in two-image lenses with $r_i\neq r_j$ only slightly, while in four-image lenses with $r_i\approx r_j$, the shear may play a significant role.

For a lens in a general quadrupole with total shear $\Gamma=\gamma_{int}+\gamma_{ext}$, the time delay can be estimated as (Kochanek & Schechter, 2004) (Kochanek, 2002)

$$\Delta t \simeq 2\Delta t_{\rm SIS}(1-\langle\kappa\rangle)\frac{\sin^2(\Delta\theta_{ij}/2)}{1-4f_{int}\cos^2(\Delta\theta_{ij}/2)}, \tag{2.6}$$

where $\langle\kappa\rangle$ is the average surface density in the annulus bounded by the images in units of the critical surface density and $f_{int}=\gamma_{int}/\Gamma$ is the fraction of the quadrupole. Here $\Delta\theta_{ij}$ represents the angle between the images $\Delta\theta_{ij}=\theta_1-\theta_2$.

To discuss the time-delay distribution in a lensing cluster, we start from a simple situation, in which the mass distribution of a lensing cluster is described by a SIS profile and no more than two multiple images are generated from each source. With the density $\rho(r)=\frac{\sigma_v^2}{4\pi Gr^2}$, the time delay is (Oguri et al., 2002)

$$c\Delta t_{\rm SIS}=32\pi^2\left(\frac{\sigma_v}{c}\right)^4\frac{D_{\rm OL}D_{\rm LS}}{D_{\rm OS}}(1+z_L)y, \tag{2.7}$$

from which it follows that $\Delta t\propto y$, i.e., the time delay is proportional to the location of the source. If the source is located within the strong lensing area enclosed by the caustic line, two images will be created. In this case, the normalized probability that the source is located between η and $\eta+{\rm d}\eta$ is (Samsing, 2010)

$$p(\eta,\eta+{\rm d}\eta)=\int_\eta^{\eta+{\rm d}\eta}2\frac{\eta}{\eta_0^2}{\rm d}\eta; \qquad \eta\leqslant\eta_0. \tag{2.8}$$

Hence, the normalized time delay probability distribution function can be simplified as

$$f(\Delta t)=2\frac{\Delta t}{\Delta t_{\rm peak}^2}; \qquad \Delta t\leqslant\Delta t_{\rm peak}. \tag{2.9}$$

Here $f(x)$ denotes a probability distribution function throughout this paper and $\Delta t_{\rm peak}$ is the time delay which has the largest probability. With $f(\Delta t){\rm d}(\Delta t)=P(\log\Delta t){\rm d}(\log\Delta t)$, and ${\rm d}(\Delta t)=\ln 10\cdot 10^{\log\Delta t}d(\log\Delta t)$, it follows that $P(\log\Delta t)=\ln 10\cdot 10^{\log\Delta t}f(\Delta t)$, i.e., the probability distribution function of the logarithmic time delay for the SIS profile is

$$P(\log\Delta t)=\frac{2\ln 10}{\Delta t_{\rm peak}^2}10^{2\log\Delta t}; \qquad \log\Delta t\leqslant\log\Delta t_{\rm peak}. \tag{2.10}$$

	inner δ	intermediate δ	outer δ	β
SIS	-2	-2	-2	2.00
NFW	-1	-2	-3	1.20
dPIE	0	-2	-4	0.83

Table 2.1: The slopes of the density profiles describing the mass distribution of a galaxy cluster and the slopes of the best-fitting functions to the time-delay distribution. More details of the best-fitting function and slope β are described in subsection 2.3.1.

The time-delay distribution is sensitive to the slope of the density profile (Keeton & Madau, 2001) (Wyithe et al., 2001). Steeper inner slopes tend to produce larger time delays (Oguri et al., 2002). There are several theoretical profiles established to describe the mass distribution of a cluster: the SIS profile, the dPIE profile (dual pseudo isothermal elliptical profile) (Elíasdóttir et al., 2007), and the NFW profile (Navarro-Frenk-White profile) (Navarro et al., 1996), etc. For a density distribution described as $\rho \propto r^{-\delta}$, the density slopes δ for these three profiles are listed in table 2.1. The slope of the density profile may affect the distribution of the time delay in this way: compared to the SIS profile, the NFW profile has shallower inner density slope, but steeper outer density slope, which means that on small time delay scales, the distribution of the time delay will be stretched out to a higher probability, but on large time-delay scales, it will be lower than the distribution of a SIS profile. The dPIE profile has even shallower inner density slope but steeper outer density slope than the NFW profile, so the time-delay distribution of dPIE profile has the shallowest slope among the three profiles. Equations (2.9) (2.10) show that the time-delay probability distribution function is a power law for the SIS profile. Motivated by the discussion above, we make the simple ansatz that the time-delay probability distribution function can be approximated as: $f(\Delta t) \propto \Delta t^{\beta-1}$ and $P(\log \Delta t) \propto 10^{\beta \log \Delta t}$, or $P(\log \Delta t) \propto \Delta t^{\beta}$. More details on the comparison of the ansatz and simulation results are presented in section 2.3.1.

This ansatz is based on the assumption of the time-delay distribution generated by a two-multiple-image system. For clusters with complicated structures, as shown in equations (2.3), (2.5), (2.6), e.g., clusters whose mass distributions are described by clumps of potentials, the situation is more complicated because more images are produced so more time delays are generated. Fortunately, the simulations described in section 2.3.2 and figure 2.2 show that the distribution of time delays generated by multiple images still obey a power-law distribution.

After normalization, the probability distribution functions can be written as:

$$f(\Delta t) = \frac{\beta}{\Delta t_{\rm peak}^{\beta}} \Delta t^{\beta-1}; \qquad \Delta t \leqslant \Delta t_{\rm peak}, \tag{2.11}$$

$$P(\log \Delta t) = \frac{\beta \ln 10}{\Delta t_{\rm peak}^{\beta}} \Delta t^{\beta}; \qquad \Delta t \leqslant \Delta t_{\rm peak}, \tag{2.12}$$

$$\log P(\log \Delta t) = \beta \log(\Delta t) + \log(\beta \ln 10) - \beta \log \Delta t_{\rm peak}; \qquad \Delta t \leqslant \Delta t_{\rm peak}. \tag{2.13}$$

We can also write the cumulative probability distribution as

$$f(<\Delta t) = \int_0^{\Delta t} f(x)dx = \begin{cases} \frac{\Delta t^\beta}{\Delta t^\beta_{\rm peak}} & \Delta t \leqslant \Delta t_{\rm peak}, \\ 1 & \Delta t > \Delta t_{\rm peak}. \end{cases} \tag{2.14}$$

If we set $\beta = 2$, the probability distribution functions (2.11) and (2.12) reduce to the expressions for the SIS case, i.e., functions (2.9) and (2.10).

According to the virial theorem(Binney & Tremaine, 2008), for a fixed radius, the enclosed mass is proportional to the velocity dispersion, $M \propto \sigma_v^2$. From equation (2.7), for the SIS profile, $\Delta t_{\rm peak,\,SIS} \propto \sigma_v^4 \propto M^2$. More generally, for a general profile with density distribution described as $\rho \propto r^{-\delta}$, the expression for the time delay can be well approximated as $\Delta t \propto \Delta t_{\rm SIS}(\delta - 1)$ (2.3), i.e., $\Delta t \propto (\delta - 1)M^2$. Hence, we can write the probability distribution function (2.13) as

$$\log P(\log \Delta t) = \beta \log(\Delta t) + \log(\beta^{C_1} \ln 10) - 2\beta \log M_{250} + C_2, \tag{2.15}$$

where C_1, C_2 are constants to be determined. Here M_{250} is defined as the projected mass within $R < 250\,$kpc, in units of $10^{14}\,{\rm M}_\odot$. In this equation, β and M_{250} are parameters. If the value of β is fixed, on the right hand of the equation (2.15), the second and the fourth terms (i.e., $\log(\beta^{C_1} \ln 10)$ and C_2) will be reduced to one constant: $C_2^{'} = C_2 + \log(\beta_{\rm fix}^{C_1} \ln 10)$. In this case, there will be only one constant $C_2^{'}$ to be determined. So the logarithmic probability distribution function can be reduced to

$$\log P(\log \Delta t) = \beta \log(\Delta t) - 2\beta \log M_{250} + C_2^{'}. \tag{2.16}$$

We will discuss β and $C_2^{'}$ in section 2.3.

2.3 MODELING CLUSTERS OF GALAXIES

In this section, we discuss how β depends on different mass profiles, and the effect of the mass on the time-delay distribution. Considering the time required for a realistic observation, small time delays, i.e., time delays no longer than 1000 days, are more suitable for an actual time-delay measurement in a reasonable amount of time. In this paper, we therefore focus on time delays less than 1000 days. We treat all time delays as independent from each other and the time delays are taken from all images pairs.

To get the time-delay distribution, we create an input catalog of sources. Time delays are created when there are multiple images, so we need to make sure that the input source plane covers the area enclosed by the caustic line(s) and includes all potential multiply lensed sources. On the other hand, the input source plane should be sufficiently well sampled so as to be sensitive to the mass distribution and potential differences in the lens. This is to make sure that small time delays are also produced. In this work, we choose an input source plane covering an area of 60 $\times$ 60 arcsec with 200 $\times$ 200 pixels in

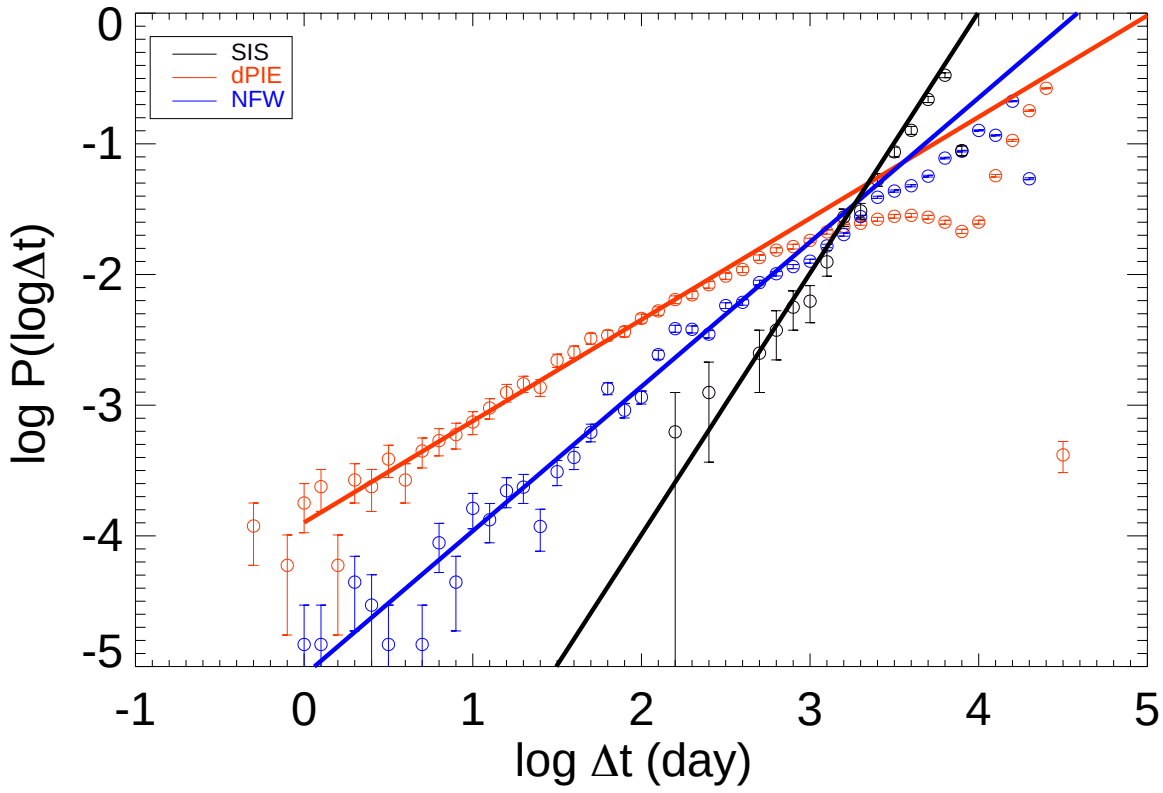

Figure 2.1: The logarithmic probability distribution of the time delays for three density profiles. They are the SIS profile (black), the dPIE density profile (red) and the NFW density profile (blue). The background sources are at $z = 3$. The open circles and their poisson error bars are obtained from a numerical representation of the potentials. The best-fitting functions for each cluster are also plotted. The slopes of the best-fitting functions for the SIS profile, the NFW profile and the dPIE profile are $\beta_{\rm SIS} = 2.0$, $\beta_{\rm NFW} = 1.11$, $\beta_{\rm dPIE} = 0.78$.

the source plane at $z = 3$. With the help of *Lenstool* (Jullo et al., 2007), we can obtain a list of all images of every source in the source plane. Then we compute the differences in the arrival times between multiple images from each source. For example, for a source with 3 multiple images: image1, image2, image3, we compute the differences of arrival times between each two of these three images. Then we get 3 time delays in total.

2.3.1 THE SLOPE OF THE TIME-DELAY DISTRIBUTION

The time-delay distributions for the SIS, the NFW and the dPIE profiles are simulated and computed. In simulating the time-delay distributions, we choose parameters similar to those of mass models of real clusters. We adjust the parameters of the profiles to make their distributions overlap. The results are shown in figure 2.1. In the NFW mass model, the velocity dispersion is 1810 km/s, the concentration is 3.579 and the scale radius is 618 kpc. In the dPIE mass model, the velocity dispersion is 1500 km/s, the core radius is 72 kpc, and the cut radius is 2000 kpc. For the mass model described by the SIS profile, we set the velocity dispersion to 400 km/s. A change in the velocity dispersion will shift the distribution horizontally but keep the slope unchanged. So for computational convenience, we keep the velocity dispersion and shift the distribution horizontally to make the results for three profiles overlap. All three profiles are circular. With time delays less than 1000 days, the slopes of the logarithmic probability distribution functions for the SIS profile, the NFW profile and the dPIE profile, are $\beta_{\text{SIS}} = 2.0$ as expected, $\beta_{\text{NFW}} = 1.11$, $\beta_{\text{dPIE}} = 0.78$, respectively (see also table 2.1). The difference in slopes of the distributions arises from the difference in the density slopes of the mass profiles, as discussed in section 2.2. This shows that the slope of the time-delay distribution is strongly affected by the mass distribution, especially the density slope of the cluster.

2.3.2 AN EXAMPLE: ABELL 1689

With the help of deep Hubble Space Telescope (*HST*) imaging, Abell 1689 ($z = 0.183$) displays a large number of multiple image systems at the center of the cluster. Using information from these systems, the mass model of Abell 1689 has been extensively studied. We base our work on the mass model consisting of 35 plausible lensed sources and 116 multiple images (Limousin et al., 2007) (Richard, 2011) (Jullo et al., 2010). Among them, 25 sources have confirmed spectroscopic redshifts, the other 10 systems have lensing modeling redshifts or/and photometric redshifts.

To check how the time-delay distribution depends on the mass distribution, we split the mass model of Abell 1689 into two parts. The first part (massive components) consists of a dark halo and the three brightest galaxies with central velocity dispersions $\sigma \geqslant 500\,\mathrm{km\,s^{-1}}$. The second part includes all other substructures (subcomponent), that is, all other gravitational potentials with velocity dispersions σ smaller than $500\,\mathrm{km\,s^{-1}}$. We compute the time-delay distribution in two different ways: First, we produce all time delays for Abell 1689 with the full mass model. Second, we compute time delays of Abell

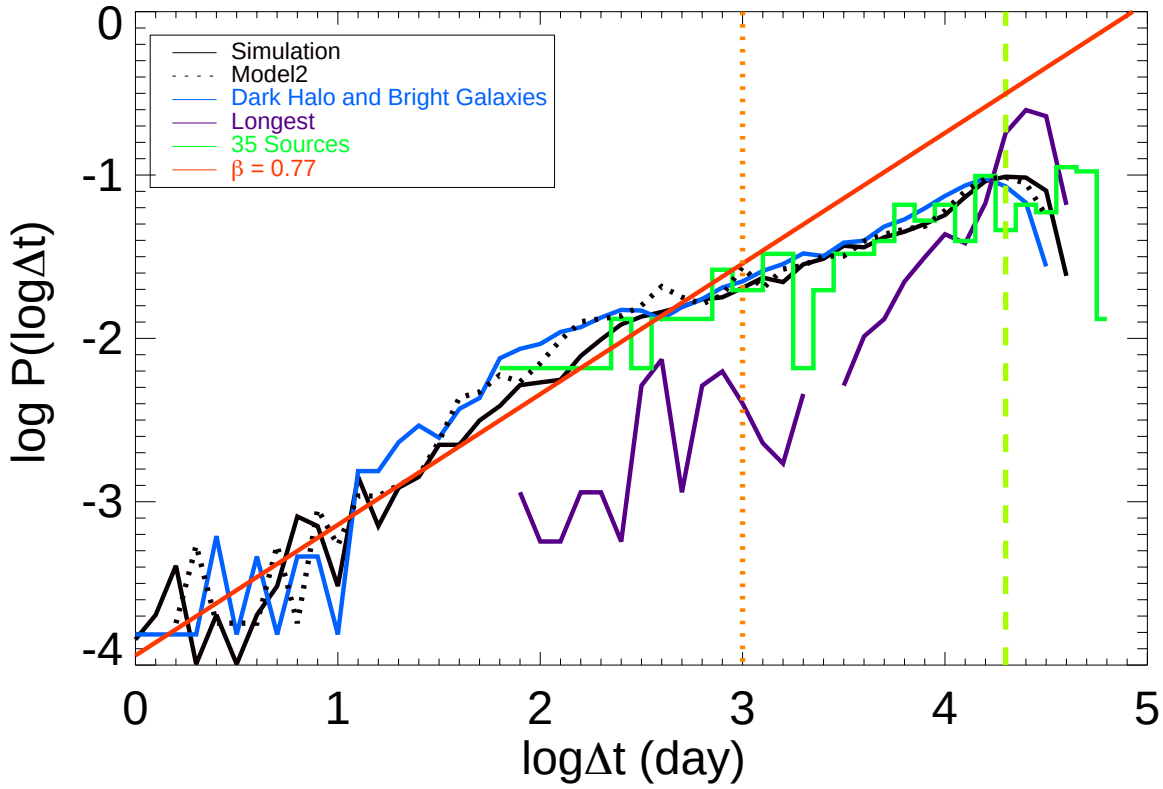

Figure 2.2: The time-delay distributions of Abell 1689 with modeled background sources at $z = 3$. The time-delay distribution produced by the cluster with the full mass model is in black. The blue curve represents the time-delay distribution produced by the dark halo and a few bright galaxies (massive components), which fails to reproduce small time delays. The distribution of the selected longest time delays from each source is in purple. The red curve represents the logarithmic probability distribution function with $\beta = 0.77$. The histogram in green represents the distribution of the time delays of 35 known multiply imaged sources. We are mainly interested in small time delays, i.e., those located to the left of the dotted orange line at 1000 days ($\log \Delta t$ = 3.0). The dashed line in olive represents $\Delta t_{\rm peak}$.

1689 with only the mass model of the first part (massive components). The second part (subcomponent) itself produces only two multiple images, i.e., only one time delay. This is because most substructures do not gain enough mass to surpass the critical surface mass density, which is required for the structure to produce multiple images.

The time-delay distribution for Abell 1689 is shown in figure 2.2. The histogram in green represents the distribution of the time delays of the 35 known sources. It is consistent with the simulation of the grid of hypothetical sources. A logarithmic probability distribution function (2.13) with slope $\beta = 0.77$ in red is also plotted. The blue curve represents the time delay distribution generated by the first part (massive components). From the figure, it is evident that the first part (massive components) succeeds in reproducing most relatively 'large' time delays, e.g., time delays larger than around 30 days. We conclude that small time delays are predominantly generated by substructures in the mass model.

The typical offset between the observed and modeled images is about $\sim 1''$ (Kneib & Natarajan, 2011). Therefore, the individual time delays are affected. To test how the position offset affects the time-delay distribution, we plot the time delay distributions generated by two different mass models for Abell 1689. The result is shown in figure 2.2. The black curve represents the time-delay distribution applied in this paper, while the dotted curve is the result when another mass model (Richard, 2010) is used. Though different models may produce different time delays, the slope of the distribution of the time delays is not strongly affected.

The time-delay distribution of a real cluster may be more complicated than the ones discussed in section 2.2. The structure of the lensing cluster may consist of more clumps of potentials with more complicated mass distribution, thus each source may produce more than 2 multiple images. To check how these extra multiple images affect the time-delay distribution and whether the distributions for real clusters can also be fitted with the power-law functions, we also plot the distribution of the longest time delays generated by each source in figure 2.2. The figure shows firstly that compared to the 'longest' time delays, the total time-delay distribution can be fitted to a power-law function. Secondly, for small time delays, though none of them belong to the 'longest' time delays and there is no direct connection between the ansatz motivated by two image systems and those non-longest time delays, the distribution of the small time delays may also be fitted with a power-law function, which is implied by the simulation result of the total time delays. Finally, even though more multiple images are generated and more time delays are produced, the time-delay distribution still can be fitted well with a power-law function. Therefore, we proceed to apply the ansatz of the power-law functions (2.11) (2.12) deduced from two-image system to the real clusters with more multiple images.

Cluster	z	RA (J2000.0) [deg]	Dec (J2000.0) [deg]	M_{250} (10^{14}M$_\odot$)	β
Abell 2204	0.152	248.195540	5.575825	2.29 ± 0.50	0.79 ± 0.03
Abell 868	0.154	146.359960	-8.651994	1.97 ± 1.11	0.57 ± 0.03
RXJ 1720	0.164	260.041860	26.625627	1.18 ± 0.59	0.64 ± 0.04
Abell 2218	0.171	248.954604	66.212242	3.00 ± 0.24	0.89 ± 0.04
Abell 1689	0.183	197.872954	-1.341006	4.53 ± 0.13	0.79 ± 0.03
Abell 383	0.188	42.014079	-3.529040	1.87 ± 0.26	0.85 ± 0.09
Abell 773	0.217	139.472660	51.727024	3.01 ± 0.58	0.86 ± 0.04
RXJ 2129	0.235	322.416510	0.089227	1.37 ± 0.37	0.74 ± 0.03
Abell 1835	0.253	210.258650	2.878470	2.83 ± 0.41	0.89 ± 0.05
Abell 1703	0.280	198.771971	51.817494	2.98 ± 0.09	0.77 ± 0.08
MACS 2135	0.325	323.800390	-1.049624	2.64 ± 0.04	0.83 ± 0.02
MACS 1319	0.328	200.034880	70.077501	2.28 ± 0.26	0.41 ± 0.06
MACS 0712	0.328	108.085460	59.538994	1.29 ± 0.27	0.63 ± 0.05
MACS 0947	0.345	146.803230	76.387101	2.96 ± 0.94	0.59 ± 0.09
SMACS 2248	0.348	342.183260	-44.530966	2.87 ± 0.06	0.80 ± 0.06
MACS 1133	0.389	173.304880	50.144436	1.52 ± 0.23	0.91 ± 0.05
MACS 1347	0.451	206.877570	-11.752643	3.86 ± 0.02	0.77 ± 0.05

Table 2.2: Properties of 17 lensing clusters. The redshifts of the selected clusters range from 0.15 to 0.30 for models from LoCuSS and from 0.30 to 0.45 for MACS clusters. Here M_{250} denotes the projected lensing mass inside 250 kpc (Richard et al., 2010) (Richard, 2010). The slopes of β in function (2.16) are also listed.

2.4 TIME DELAYS IN 17 CLUSTERS

2.4.1 CLUSTER SELECTION AND MODELING

To further analyze the logarithmic probability distribution function of time delays and constrain the parameter and the constant in equation (2.13), we compute time-delay distributions by modeling 17 lensing clusters. The cluster selection procedure is based on two criteria: First, each lensing cluster system should have at least one image with a spectroscopically-confirmed redshift. Furthermore, the range of redshifts of the selected clusters should be as large as possible. The redshifts of the selected clusters range from 0.15 to 0.30 for models from LoCuSS (Richard et al., 2010) and from 0.30 to 0.45 for MACS models (Richard, 2010). The selected clusters are listed in table 2.2.

The modeling procedure is the same as described in section 2.3. To make a reasonable comparison, the input source file for each cluster should have the same number of sources. Moreover, the whole source area should have the same size and be sufficiently sampled to cover the multiple image areas described by the caustic lines.

2.4.2 ESTIMATING β

As for Abell 1689 (section 2.3.2), we fit power-law distribution functions to time-delay distributions generated from the 17 cluster models. The functions are fitted to the data with time delays less than 1000 days. The cluster masses (Richard, 2011) (Richard et al., 2010) and the fitting values of β are shown in table 2.2. The distribution of the parameter β is shown in figure 2.3. The mean value is $\bar{\beta} = 0.75$, and the median value is $\dot{\beta} = 0.79$. With the least squares method, if the clusters are weighted equally to each other, we determine that the best-fitting slope is $\widetilde{\beta} = 0.77$ for the 17 clusters, with standard deviations in $\log P(\Delta t)$ in the range [0.11, 0.30]. As a consequence, to a good approximation, β can be fixed in equation (2.16).

2.4.3 PARAMETER ESTIMATION

We fix the value of $\widetilde{\beta} = 0.77$ in the logarithmic probability distribution function (2.16) and fit the function to the simulated data, and then find the best-fitting value for constant C_2'. With smallest deviations, we find that the best-fitting value is $C_2' = -3.28$. So the logarithmic probability distribution function (2.16) can be written as

$$\log P(\log \Delta t) = \widetilde{\beta} \log \Delta t - 2\widetilde{\beta} \log M_{250} - 3.28, \tag{2.17}$$

or

$$P(\log \Delta t) = 5.27 \times 10^{-4} \Delta t^{\widetilde{\beta}} / M_{250}^{2\widetilde{\beta}}. \tag{2.18}$$

If we introduce $\widetilde{\beta} = 0.77$, then the logarithmic probability distribution function is simply

$$\log P(\log \Delta t) = 0.77 \log \Delta t - 1.54 \log M_{250} - 3.28. \tag{2.19}$$

For a cluster with $M_{250} = 2 \times 10^{14}$ $M_\odot$, the probability of a time delay less than 1000 days is about 0.025. In figure 2.4, we present modeled time-delay distributions for all

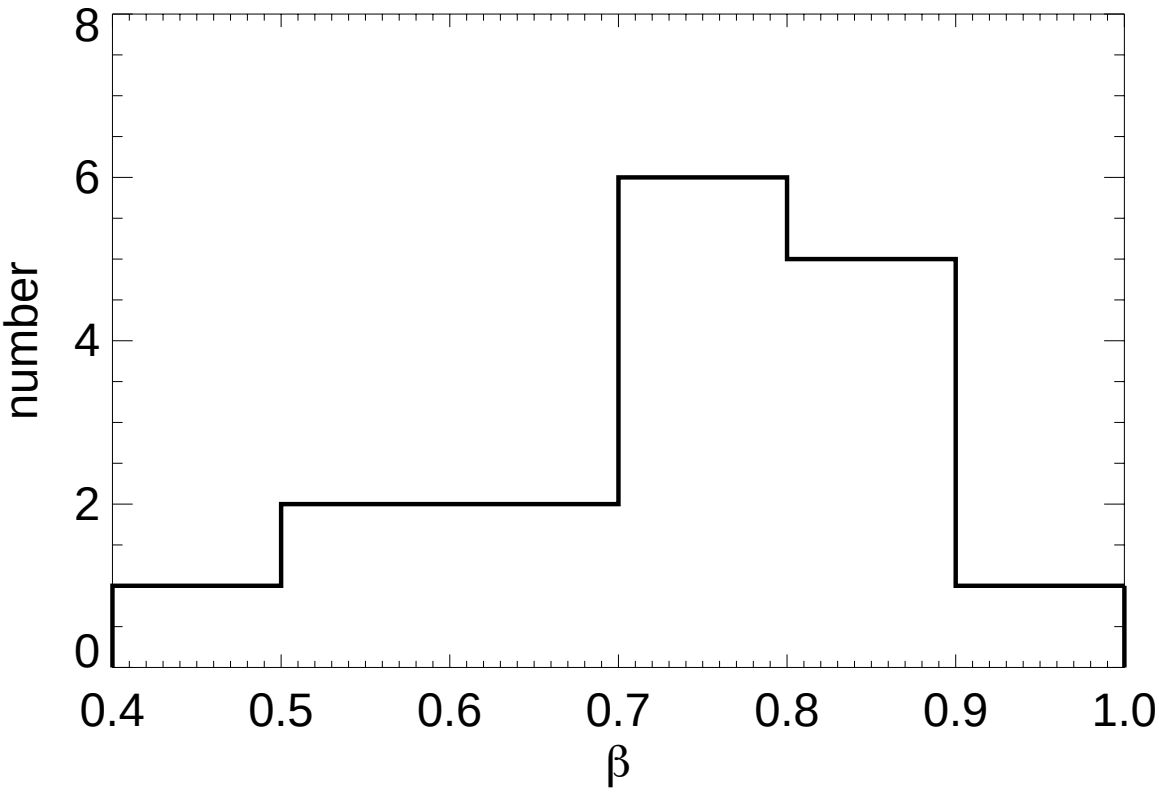

Figure 2.3: The distribution of parameter β for probability distribution functions of 17 clusters. The modeling sources are at $z = 3$. The probability distribution functions are fitted to the modeling data of time delays within 1000 days. The parameter range is $\beta \in [0.41, 0.91]$.

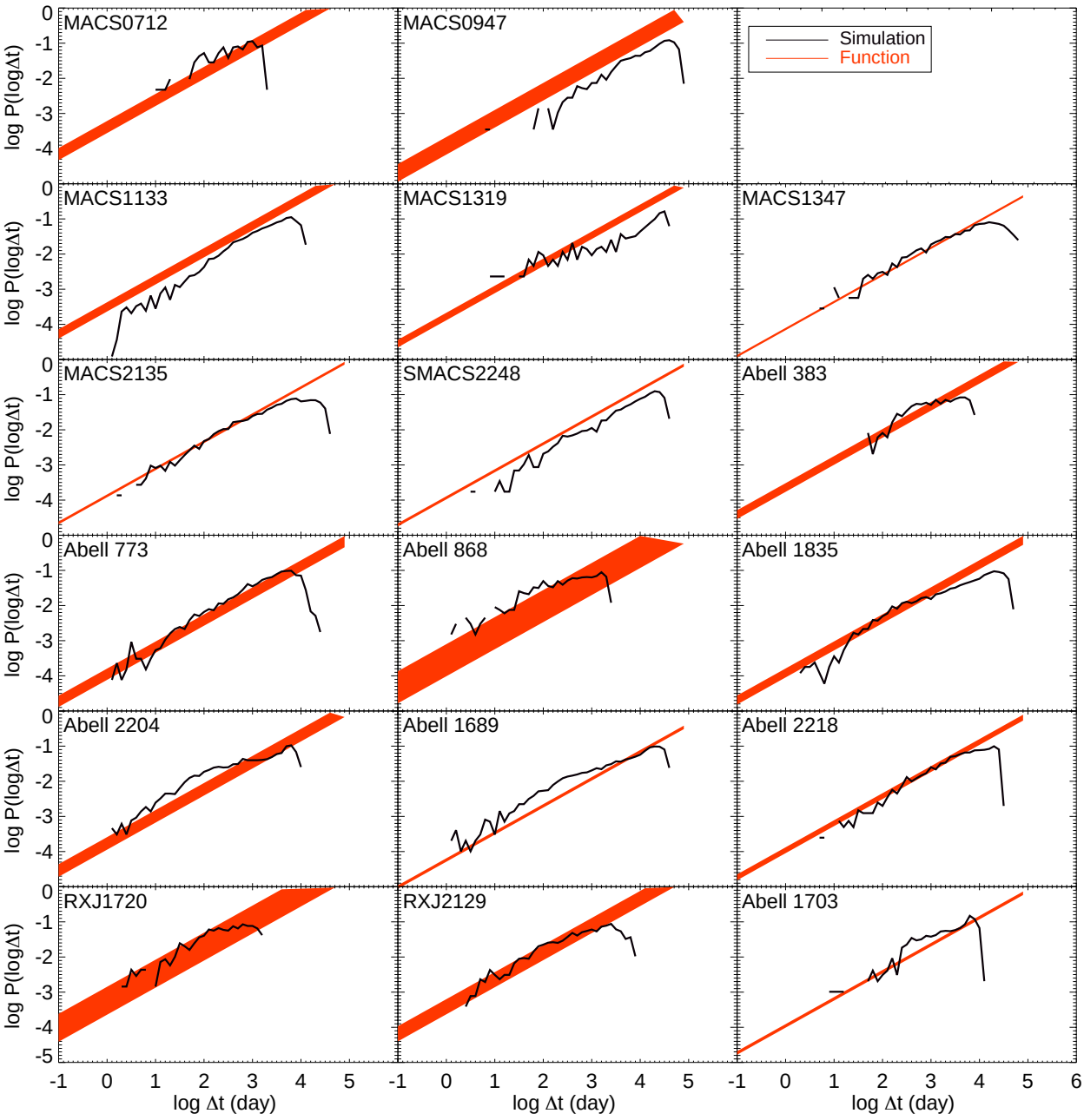

Figure 2.4: The logarithmic probability distribution functions for 17 clusters with background sources at $z = 3$. The solid curves represent the modeling results of time-delay distribution of 17 clusters. The red shaded regions represent the logarithmic probability distribution function from equation (2.19). The uncertainties of the distribution functions arise from the uncertainties in the mass. For MACS1133, the input source area is 10×10 arcsec. For other clusters, the input source areas are 60×60 arcsec.

17 clusters and their logarithmic probability distribution functions (2.19) with sources at $z = 3$. Among the 17 systems, MACS1133 has much smaller multiple-image area enclosed by the caustic lines. To make the small time delays detectable, for MACS1133, we change the input source area to 10×10 arcsec. For other clusters, we keep the input source as 60×60 arcsec.

2.5 THE RATE OF LENSED SUPERNOVAE IN ABELL 1689

With the help of the gravitational lensing amplification, we can potentially observe supernovae which would otherwise be too faint for detection. If a source is located inside the multiply imaged surface defined by the caustic line, two or more images will be generated. We may therefore observe multiple images of a supernova in the source galaxies.

For Abell 1689, we know 35 multiply imaged sources and 116 corresponding multiple images. For each multiple-image pair producing a time delay, we call the image arriving first to the observer the *leading image*. For example, for a source with 3 multiple images: image1, image2, image3, assuming the images have arrival times $\tau_{image1} < \tau_{image2} < \tau_{image3}$, there are three image pairs: pair12, pair13 and pair23. The corresponding leading images are image1, image1 and image2, accordingly. So in this three-image system, only the image with the longest arrival time (in this case, it is image3) cannot be the leading image. That is, for 1 source having 3 multiple images, the number of the leading images are $3-1 = 2$. Therefore, in a lensing system with m sources and n corresponding multiple images, the number of the leading images are $n-m$. According to this definition, in Abell 1689, there are $(116 - 35 =)$ 81 leading images in total.

To estimate the probability of observing a leading supernovae image in Abell 1689, we need to know the supernova rate. The models for describing the supernova rate are dependent on the types of the supernova. The rate of core-collapse supernovae ($\mathrm{SNR_{cc}}$) can be obtained from the star-formation rate:

$$\left(\frac{\mathrm{SNR_{cc}}}{\mathrm{yr}^{-1}}\right) = k_{\mathrm{cc}} \cdot 10^{-3} \left(\frac{\mathrm{SFR}}{\mathrm{M}_{\odot}\ \mathrm{yr}^{-1}}\right), \tag{2.20}$$

where the parameter k_{cc} can be determined by measuring the $\mathrm{SNR_{cc}}$ and SFR. Here the factor of 10^{-3} is multiplied into the function to simplify the parameter k_{cc}. We also multiply factors in the following functions (2.21) (2.26) for the same reason. The $\mathrm{SNR_{cc}}$ and SFR can be derived from observational data (Dahlen et al., 2004) (Giavalisco et al., 2004). By using the core-collapse SN rate density and comparing it against the SFR density, the parameter is constrained to be $k_{\mathrm{cc}} = 7.5 \pm 2.5$ (Scannapieco & Bildsten, 2005). Alternatively, by using a Salpeter IMF and a progenitor mass ranging between 8 and 50 solar masses, the parameter is estimated to be $k_{\mathrm{cc}} = 7$ (Riehm et al., 2011). In this paper, we choose $k_{\mathrm{cc}} = 10$ as the upper limit, and $k_{\mathrm{cc}} = 5$ as the lower limit.

For Type Ia supernovae, we use the popular "two-component" model to estimate the Type Ia supernova rate ($\mathrm{SNR_{Ia}}$) (Scannapieco & Bildsten, 2005) (Mannucci et al., 2005)

(Sullivan et al., 2006):

$$\left(\frac{\mathrm{SNR_{Ia}}}{\mathrm{yr}^{-1}}\right) = \hat{A}\cdot 10^{-10}\left(\frac{M_\star}{\mathrm{M}_\odot}\right)^{\alpha} + \hat{B}\cdot 10^{-3}\left(\frac{\mathrm{SFR}}{\mathrm{M}_\odot \mathrm{yr}^{-1}}\right), \tag{2.21}$$

where $M_\star$ is the host stellar mass, and α denotes the exponent of the stellar mass. The first component describes the stellar mass contribution. The second component describes the host galaxy star-formation contribution. For parameters $\hat{A}$ and α, we choose $\hat{A} = 1.05 \pm 0.16$ and $\alpha = 0.68 \pm 0.01$ (Smith et al., 2011). The parameter $\hat{B}$ can be related to the $\mathrm{SNR_{cc}} - \mathrm{SFR}$ relation (2.20),

$$\hat{B} = k_{\mathrm{cc}}\Theta, \tag{2.22}$$

where $\Theta = \mathrm{SNR_{Ia}}/\mathrm{SNR_{cc}}$. The value of Θ has been estimated at redshift up to $z \sim 1.5$ (Dahlen et al., 2004). At redshift $z < 1$, the ratio of $\mathrm{SNR_{Ia}}/\mathrm{SNR_{cc}}$ approximately ranges between $\Theta = 1/2$ and $\Theta = 1/4$, which is consistent with the result $\Theta = 0.35 \pm 0.08$ in nearby galaxies (Mannucci et al., 2005). At higher redshift $z > 1.0$, inspired from figure 3 of (Dahlen et al., 2004), we assume

$$\Theta = \frac{1}{15}; \qquad 1.0 \leq z. \tag{2.23}$$

Considering all sources in Abell 1689 have redshifts $z > 1.0$, in this work, $\hat{B} = 0.5 \pm 0.17$. This value is consistent with $\hat{B} = 0.39 \pm 0.07$ (based on redshift $0.2 < z < 0.75$ (Sullivan et al., 2006)).

From their magnitude in F775W, we estimate the flux and the luminosity and then constrain their SFR (Kennicutt, 1998) as

$$\left(\frac{\mathrm{SFR}}{\mathrm{M}_\odot\ \mathrm{yr}^{-1}}\right) = 1.4\times 10^{-28}\left(\frac{\bar{L}_\nu}{\mathrm{erg\ s^{-1}\,Hz^{-1}}}\right). \tag{2.24}$$

This conversion between UV flux and the SFR is for rest wavelengths, ranging from 1500 Å to 2800 Å, while our data (Limousin et al., 2007) have observed wavelength in the range 6900 Å to 8600 Å. We assume these galaxies have flat spectra, as is typical for star-forming galaxies, so we can calculate the luminosity from the flux.

Note that multiple images from the same source should have the same inferred luminosity. To infer the luminosity of each image, we need to know their fluxes. With magnitudes of 116 images (Limousin et al., 2007) (Richard, 2011), we can estimate their fluxes. Using *Lenstool*, we can get a magnification map on the image plane then read the values of the magnification on the map. Considering the gravitational magnification effect and *k correction* (Hogg et al., 2002) (van Dokkum & Franx, 1996), the flux can be calculated as

$$\log(F_\nu) = [m_{\mathrm{AB}} + 2.5\log(|\mu|) + 2.5\log(1+z) + 48.6]/(-2.5), \tag{2.25}$$

where μ is the gravitational magnification factor, and z is the source redshift. When images are located close to the caustics, their gravitational magnification factors (μ) may

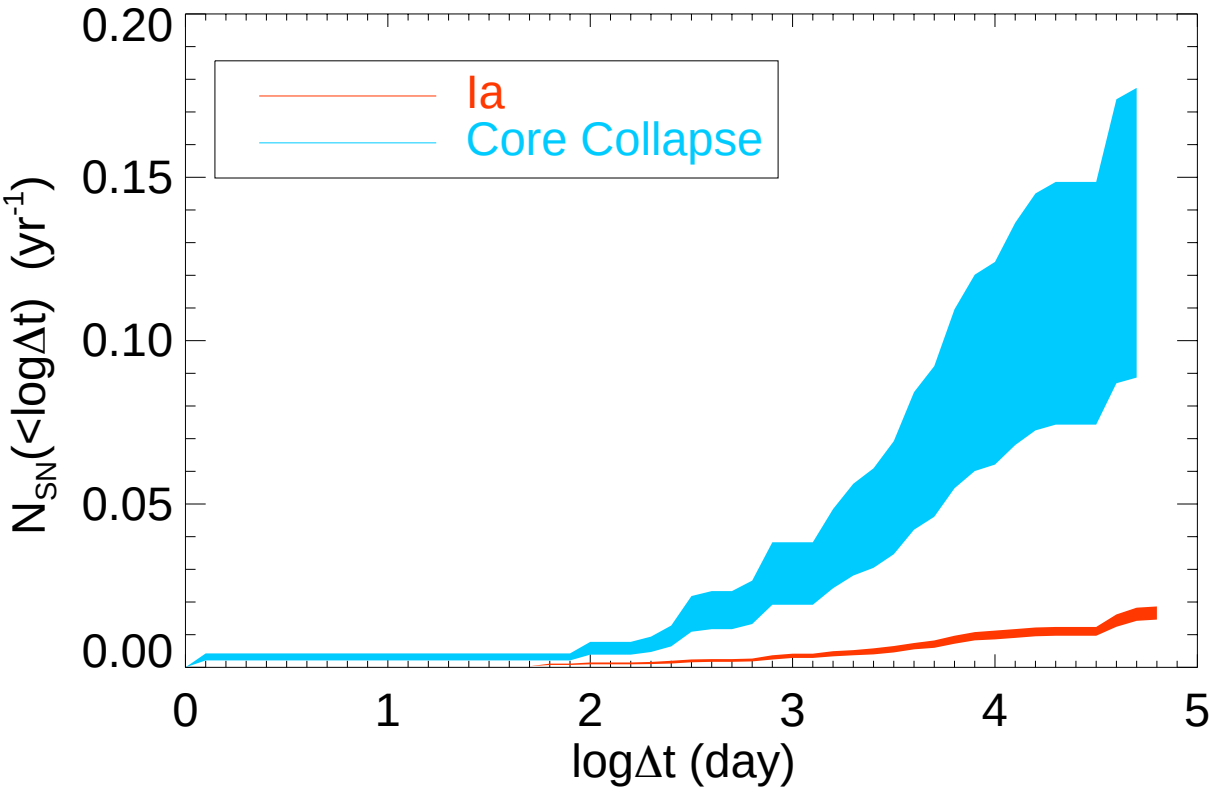

Figure 2.5: The cumulative rate ($N_{\rm SN}$) of the leading images of lensed supernovae in Abell 1689, derived from equations (2.20) and (2.26). The magnitude threshold is 26.5 and a total number of 70 among the 72 leading images are included because of the magnitude threshold. The time delays are calculated based on the modeled source positions. The red curve represents the estimated cumulative $\rm SNR_{Ia}$, while the cumulative $\rm SNR_{cc}$ is plotted in blue curve. The uncertainties of $N_{\rm SN}$ arise from the upper and lower limits of the parameters in the functions (2.20) (2.21) (2.26).

be very large. Thus, the values of fluxes of these images derived from equation 2.25 are uncertain, and their luminosities estimated from the fluxes may not be reliable. So we neglect these images and average other luminosity values of images of the same source to constrain $\bar{L}_\nu$. When we know their luminosities, from equation (2.24), we can calculate their SFR, and then $\mathrm{SNR_{Ia}}$ (2.26) and $\mathrm{SNR_{cc}}$ (2.20).

We also need to calculate the stellar masses and the star-formation rates for each galaxy. To estimate the stellar-mass contribution to the SNR, we separate the images into two groups. In group one, with data of photometry from *HST*/ACS in bands B, V, I, Z, ground-based near-infrared imaging and *Spitzer*/IRAC photometry (Richard, 2011), we derive their stellar mass from SED fitting (Walcher et al., 2011). In group two with insufficient photometric data, we estimate the mass contribution based on the ratio of mass and star-formation contribution to the SNR derived from group one. The median value of this ratio, is only 2.9% (4.2%) of the upper (lower) limits of the star-formation part. In this paper, we choose its median value and assume the mass part contributes 3.5 % of the star-formation part. Therefore, for group two, the $\mathrm{SNR_{Ia}}$ may be estimated as

$$\left(\frac{\mathrm{SNR_{Ia}}}{\mathrm{yr}^{-1}}\right) = 1.035 \cdot \hat{B} \cdot 10^{-3} \left(\frac{\mathrm{SFR}}{\mathrm{M_\odot yr}^{-1}}\right). \tag{2.26}$$

We assume Type Ia supernovae have absolute magnitude $M = -19.3$ mag (Dahlen et al., 2004), and core-collapse supernovae have $M = -17.0$ mag (D'Andrea et al., 2010). With their absolute magnitudes, considering the *k correction*, we calculate the apparent magnitudes for each supernova. Their apparent magnitudes of a supernova can be expressed as:

$$m = M + 5\log_{10}(D_L/10\ \mathrm{pc}) - 2.5\log_{10}(|\mu|) - 2.5\log_{10}(1+z). \tag{2.27}$$

Here D_L denotes the luminosity distance. This equation is used to constrain the magnitude when considering the magnitude thresholds in figures 2.5 and 2.7.

The cumulative rate of observing the leading images of the lensed supernovae in Abell 1689 is shown in figure 2.5. Among the total 81 leading images, we exclude 14 images from 5 sources with insufficient magnitude data (Limousin et al., 2007), so there are 72 leading images to be considered. Here $N_{\mathrm{SN}}(< \log \Delta t)$ represents the cumulative rate of the supernova images observable in one year. We set the detection threshold to 26.5 mag in all bands. In that case, a total number of 70 of the 72 leading images are included. The resulting probabilities are 0.004 ± 0.002 for the Type Ia supernovae and 0.029 ± 0.001 for the core-collapse supernovae in one year, assuming time delays less than 1000 days.

We also compare our results to the results from other groups (Riehm et al., 2011). The result is shown in figure 2.6. The difference in supernovae rates may arise from the difference in the lens model and/or the SNR prescription. For example, different lens models may produce different magnification factors for each images, and then produce different luminosities, and SFR. In addition, the different parameters chosen in the SNR model (2.21), e.g., k_{cc}, $\hat{A}$, α, $\hat{B}$ may also affect the constraint on SNR. In this paper, we

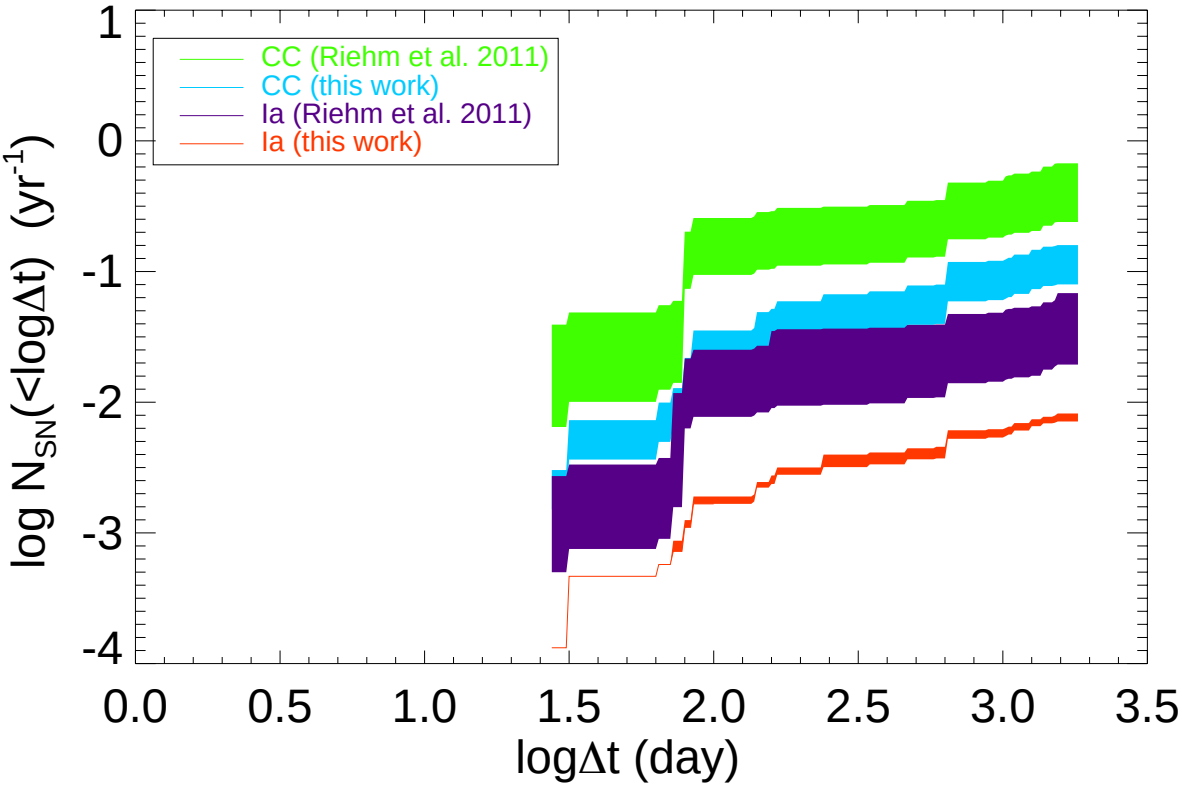

Figure 2.6: The comparison of the supernova rate estimated from functions (2.20) and (2.26), and the supernova rate from (Riehm et al., 2011), with time delays less than 5 years. The green and purple curves represent the logarithmic cumulative $\mathrm{SNR_{cc}}$ and $\mathrm{SNR_{Ia}}$ from (Riehm et al., 2011). Our results are shown in blue for $\mathrm{SNR_{cc}}$ and in red for $\mathrm{SNR_{Ia}}$. The uncertainties of $\log N_{SN}$ arise from the upper and lower limits of the parameters in the functions (2.20) (2.21) (2.26). At $\log \Delta t \sim 1.8$, there is a fast increase in the $\log N_{\mathrm{SN}}$. Firstly, in this region, there are more leading images included, so both our results and the results from (Riehm et al., 2011) raise quickly. Secondly, the leading images have much larger SNR and uncertainties in their result. This causes an even faster raise and higher upper limit in their curves.

choose $k_{cc} = 7.5 \pm 2.5$, $\hat{A} = 1.05 \pm 0.16$, $\alpha = 0.68 \pm 0.01$, $\hat{B} = 0.5 \pm 0.17$, while in (Riehm et al., 2011), the parameters are $k_{cc} = 7.0$, $\hat{A} = 4.4^{+1.6}_{-1.4}$, $\alpha = 1.0$, $\hat{B} = 2.6 \pm 1.1$. Larger values of $\hat{A}$, α, $\hat{B}$ chosen will cause a higher SNR estimate. We applied the parameters of (Riehm et al., 2011) to the functions (2.20) (2.21) (2.26), in an attempt to reproduce their results. The results fit well to their SNR_{Ia}, but a significant discrepancies remain for SNR_{cc}.

We estimate the probability of observing the leading supernova images as a function of magnitude threshold in figure 2.7. The figure shows the cumulative rates of observable leading supernova images as a function of magnitude threshold, with time delays less than 1000 days. For a magnitude threshold of 27.0, we can observe 0.044 ± 0.015 core-collapse supernovae per year, with time delays less than 1000 days. Under the conditions of small time-delay scales and limited magnitude threshold, the probability of observing a leading supernova image is quite low.

2.6 SUMMARY AND DISCUSSION

We analyzed the time-delay distributions in strong lensing systems. We found that we can describe the probability distribution of time delays as a power law function (2.16). In the function, there are two parameters, M_{250}, β, and a constant $C_2^{'}$. Modeling with mass profiles of SIS, NFW and dPIE (in figure 2.1), we found that the parameter β is strongly affected by the slopes of the mass profiles of the lensing clusters. The shallower the inner density profile and the steeper the outer density profile are, the more the time-delay distribution will be stretched out to both the higher and the lower end, causing a lower β. By modeling Abell 1689, we found that the massive galaxies and halos mainly produce large time delays, while small time delays are predominated produced by substructures (galaxies) in the cluster. We also simulated and verified that the time-delay distribution generated by 'real' clusters with more than 2 multiple images from the same sources also obey the power-law distribution in figure 2.2.

To estimate the parameter and the constant in the logarithmic probability distribution function, we modeled 17 strong lensing clusters as shown in figure 2.4, using their well calibrated mass models. With the fixed best-fitting slope $\widetilde{\beta} = 0.77$, we determined the best-fitting value of $C_2^{'}$ to the function (2.16). The resultant logarithmic probability distribution function (2.19) enables us to estimate the time-delay distribution of a cluster with known mass.

We also calculated the probability of observing the leading images of the lensed supernovae in Abell 1689. The SNR_{cc} can be derived from the SFR (2.20). The "two component" model was applied to constrain the SNR_{Ia}. We constrained the parameters in the function (2.21), and calculated the SNR for Type Ia supernova. We estimated the luminosity from magnitudes of images in Abell 1689 (2.25), derived the SFR from the luminosity (2.24), and then estimated the probability of observing a leading supernova image in the system as shown in figure 2.5. Considering a typical magnitude limit of observations with $m_{AB} = 26.5$, we can observe 0.004 ± 0.002 Type Ia supernovae and 0.029 ± 0.001

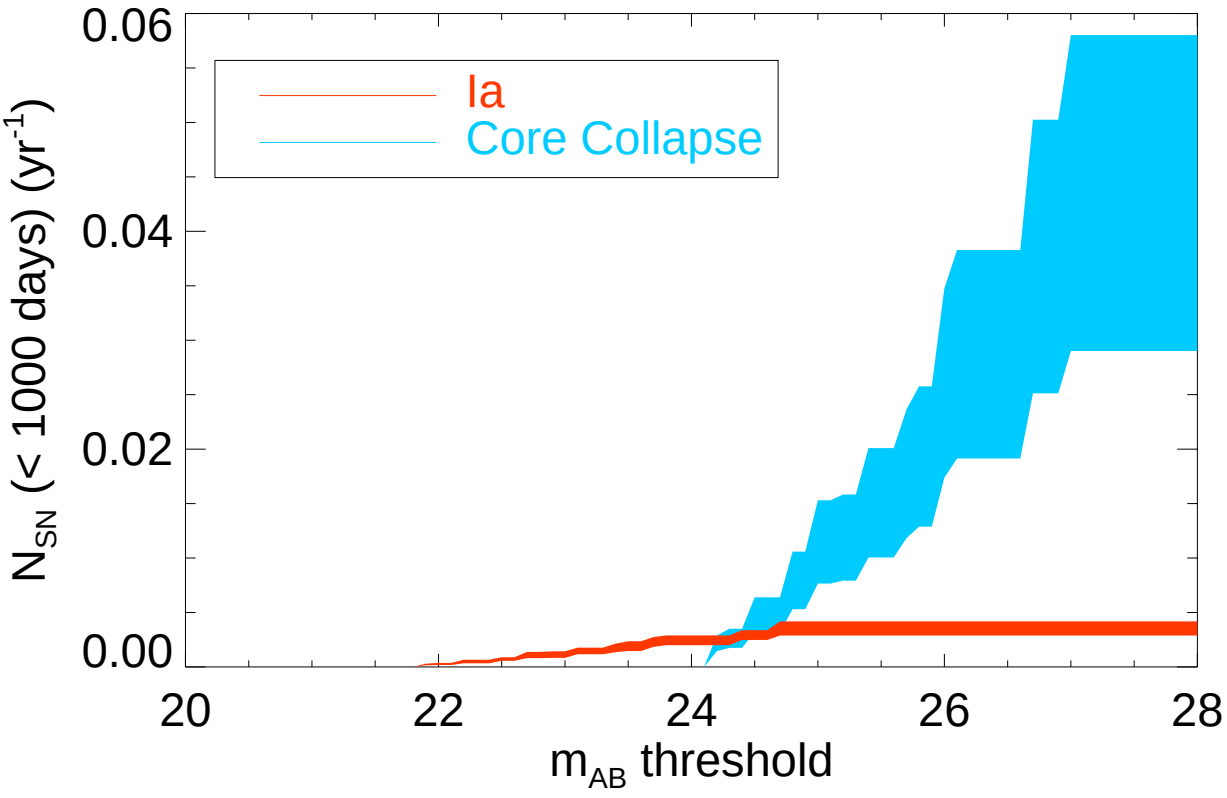

Figure 2.7: The cumulative rate of observing a leading supernovae image, as a function of magnitude threshold. The images have time-delay separations less than 1000 days. The uncertainties of $N_{\rm SN}$ arise from the upper and lower limits of the parameters in the functions (2.20) (2.21) (2.26). The Type Ia supernovae involved are much brighter than those of the core-collapse supernovae. This causes a 'shift' in the distributions of the rates of Type Ia supernovae. At $m_{\rm AB}$ around 24.7 for Type Ia supernovae, the curve flattens out. This is because all the Type Ia supernovae involved in the calculation have magnitudes smaller than about 24.7. The *HST* telescope has the magnitude limit in detecting the lensed sources. The *James Webb Space Telescope* may detect fainter lensed sources behind Abell 1689. As a sequence, Type Ia supernovae fainter than 24.7 will be detected, and the cumulative rate of observing a leading Type Ia supernovae ($N_{\rm SN}$) will increase at $m_{\rm AB} > 24.7$ as well. This is also the case for the core-collapse supernovae when $m_{\rm AB} > 27.0$.

core-collapse supernovae per year. We compared the results in this work to (Riehm et al., 2011) as shown in figure 2.6, and discussed the possible reasons which may cause the differences.

We also constrained the cumulative rate of observing a leading supernovae image, as a function of the magnitude threshold (in figure 2.7). If the magnitude limit is lowered to 27.0, the probability of observing the leading images of the core-collapse supernovae will be up to 0.044 ± 0.015 per year, with image separations within 1000 days. This probability is quite low, which means that detecting time delays from lensed supernovae will be challenging with current facilities.

We thank Johan Samsing for discussions on his work on time-delay distributions. We thank Danuta Paraficz and Árdís Elíasdóttir for many helpful discussions on gravitational lensing. We also thank Claudio Grillo, Andrew Zirm and Teddy Frederiksen for their helpful comments on the paper, and Enrico Ramirez-Ruiz for discussion on Type Ia supernova progenitor models. The Dark Cosmology Centre is funded by the Danish National Research Foundation.

3

GRB-SNe

Prediction is very difficult,
especially
if it's about the future.
Niels Bohr

Abstract -

Context. *Little is known about the diversity in the light curves of supernovae (SNe) associated with gamma-ray bursts (GRBs), including whether the light curve of SN 1998bw can be used as a representative template or whether there is a luminosity-decline rate relation akin to that of SNe Ia.*

Aims. *In this paper, we aim to obtain well-constrained light curves of GRB-SNe without the assumption of empirical or parametric templates and to investigate whether the peak brightness correlates with other parameters such as the light curve shape or the time of peak.*

Methods. *We select eight SNe in the redshift range 0.00857 to 0.606, which are firmly associated with GRBs. The light curves of these GRB-SNe are well sampled across the peak. Afterglow and host galaxy contributions are subtracted and dust reddening is corrected for. Low-order polynomial functions are fitted to the light curves. A K-correction is applied to transform the light curves into the rest frame V band.*

Results. *GRB-SNe have fairly uniform peak luminosities, similar to SNe Ia. Moreover, GRB-SNe follow a luminosity-decline rate relation similar to the Phillips relation for SNe Ia. The relation between the peak magnitude $M_{\rm V,peak}$ and the decline rate $\Delta m_{\rm V,15}$ in V band is $M_{\rm V,peak} = 1.57^{+0.25}_{-0.28}\Delta m_{\rm V,15} - 20.58^{+0.22}_{-0.20}$ mag, with $\chi^2 = 5.51$ for 6 degrees of freedom and dispersion $\sigma = 0.18$ mag. This luminosity-decline rate relation is tighter than the $k - s$ relation, where k and s are the factors describing the relative brightness and width to the light curve of SN 1998bw. The peak luminosities of GRB-SNe are also weakly correlated with the time of peak: the brighter the GRB-SN, the longer the rise time.*

Submitted for publication as: Xue Li, Jens Hjorth – *Light Curve Properties of Supernovae Associated With Gamma-ray Bursts*, Astronomy & Astrophysics.

Conclusions. *The light curve of SN 1998bw, stretched around the time of explosion, can be used as a template for GRB-SNe with reasonable confidence, but stretching around the peak produces better results. GRB-SNe exhibit a luminosity-decline rate relation, similar to SNe Ia, both in normalization and slope. The existence of such a relation provides a new constraint on GRB explosion models. Considering the usefulness of SNe Ia in measuring cosmological distances, it is possible that GRB-SNe can be used as standardizable candles to measure cosmological distances and constrain cosmological parameters.*

3.1 INTRODUCTION

Gamma-ray bursts (GRBs) were first observed by the Vela Satellites in 1967 (Klebesadel et al., 1973). Being flashes of narrow beams of intense electromagnetic radiation observed in distant galaxies (Metzger et al., 1997) with peak energies in the gamma ray energy range, they are the most luminous phenomena in the universe. The bursts are usually separated into two classes: long and short (Kouveliotou et al., 1993). The long GRBs have a duration of more than two seconds, while the short events last less than two seconds. Since the first discovery of the connection between SN 1998bw and GRB 980425 (Galama et al., 1998; Iwamoto et al., 1998; Kulkarni et al., 1998; Woosley et al., 1999), many SNe have been found to be associated with long GRBs (Hjorth & Bloom, 2012; Hjorth et al., 2003; Stanek et al., 2003; Woosley & Bloom, 2006).

A collapsar model (MacFadyen & Woosley, 1999; MacFadyen et al., 2001) has been developed to explain the GRB-SN connection. The luminosities of GRB-SNe are in a small range (Mazzali et al., 2014, 2013). But the properties of GRB-SNe, as well as GRBs are still under debate, e.g., what are the progenitors for long and short GRBs? Can GRB-SNe be used as standard candles? To answer these and other relevant questions, light curves of GRB-SNe are required.

In previous studies, the light curves of SN 1998bw in the U, B, V, R, I bands were used as a template to model the light curves of GRB-SNe (Bloom et al., 1999; Cano, 2013; Ferrero et al., 2006). The light curves of SN 1998bw were shifted to the corresponding redshift and scaled to the peak luminosity and stretched in time (Cano et al., 2011b). Some work used semi-analytical models (Richardson et al., 2006) to constrain GRB-SN light curves (Richardson, 2009). But whether the semi-analytical models or the light curve of SN 1998bw can be used as a stretchable template is still unknown. We do not know if there is a better way to stretch the template other than stretching with factor s (Cano et al., 2011b). We do not even know if the luminosities of GRB-SNe can be corrected with properties of their light curves and used as standard candles to measure cosmological distance (Stanek et al., 2005). To test this, it is important to obtain light curves instead of using the SN 1998bw light curve as a template.

It is not easy to obtain light curves of GRB-SNe. Sometimes a GRB is so bright that even though its afterglow declines rapidly (van Paradijs et al., 1997), it may still exceed the brightness of its associated SN, in which case no SN will be detectable. This is also the case when a host galaxy is brighter than a GRB-SNe (Hjorth, 2013). Dust along the line

of sight will extinguish the SN light. Moreover, any constraint we impose on the light curves e.g., afterglow modeling or SN light curve modeling, may bias the study.

Our task is to find a way to obtain light curves of GRB-SNe without using light curve templates. With such light curves, we may test if peak luminosities of GRB-SNe are correlated with other properties of the light curves, such as is the case for SNe Ia (Phillips, 1993; Phillips et al., 1999; Riess et al., 1998). We may further test if the light curve of SN 1998bw can be used as a general light curve template for GRB-SNe, and, if so, how to stretch this light curve template.

The outline of this paper is as follows. In section 3.2, we discuss the general steps in obtaining light curves of GRB-SNe from published data. In section 3.3, we present the data and obtain light curves for GRB-SNe. Then in section 3.4 we analyze the properties of the light curves of GRB-SNe. We present a luminosity-decline rate relation and other properties of the light curves for GRB-SNe. We also test if the light curve of SN 1998bw can be used as a general light curve template and if there is a better way to stretch it than the commonly used approach. In section 4.5, we summarize our investigation and discuss future prospects.

3.2 LIGHT CURVES OF GRB-SNE

Our goal is to obtain light curves of GRB-SNe in the rest frame V band. This is because, as shown in Figure 3.1, the spectral energy distribution (SED) peaks around the V band. In addition, the K-correction procedure (section 3.2.5) relies on using a redder band to correct to the rest-frame flux and we rely on the availability of suitable data. After the light curves are obtained, we measure peak magnitudes ($M_{\mathrm{V,peak}}$) and decline rates ($\Delta m_{\mathrm{V},\alpha}$). Here $\Delta m_{\mathrm{V},\alpha}$ is defined as the decline of the V-band magnitude α days after the SN has reached its peak brightness.

For error estimation, we use a standard Monte Carlo method to resimulate the data throughout the paper. The resimulated data are gaussian distributed. The resulting uncertainties are quoted as 68.3% ($\pm 1\sigma$) of the total resimulated results. In general, to obtain a light curve, we account for the effects of the host galaxy and the afterglow, and subtract their contributions from the total flux. We correct for extinction and fit low-order polynomial functions to the resimulated data. A K-correction is used to get the peak magnitude and decline rate in the rest frame V band. To do so, we either apply a multi-band K-correction, or use the SN 1998bw peak SED and decay properties to correct the values of the peak magnitude and the decline rate in bands obtained in a wavelength close to the rest frame V band.

3.2.1 HOST GALAXY

The brightness observed is the total flux of the GRB-SN, the afterglow, and the host galaxy. In some cases, the host galaxy is sufficiently faint compared to the SN that the host contribution is negligible. But for other systems, the host galaxy will contaminate

the SN light curve. In these cases, to obtain the intrinsic SN luminosity, the contribution of the host galaxy must be subtracted.

The brightness of a host galaxy is constant. It is usually observed when the SN has faded away. In this paper, we take the host brightness from the literature. The host brightness is resimulated with the standard Monte Carlo method, and subtracted from the total brightness.

3.2.2 AFTERGLOW

Table 3.1: The slopes and the break times for GRB 050525A and GRB 090618.

GRB/XRF/SN	smooth function[a]				broken power-law		reference
	$\bar{t}_{\rm break}$ (day)	$\bar{\beta}_1$	$\bar{\beta}_2$	$\widehat{\beta}^b$	$t_{\rm break}$ (day)	β_2	
050525A/2005nc	0.3	1.1	1.8	1.63	0.3	$1.74^{+0.11}_{-0.15}$	(1), (2)
090618	0.48 ± 0.08	0.79 ± 0.01	1.74 ± 0.04	$1.52^{+0.06}_{-0.05}$	0.5	$1.56^{+0.07}_{-0.08}$	(3)

[a]: An afterglow fitting method with $m(t) = -2.5 \times \left(\left(\left(\frac{t}{t_{\rm break}} \right)^{\bar{\beta}_1} + \left(\frac{t}{t_{\rm break}} \right)^{\bar{\beta}_2} \right)^{-1} \right) + B$ (Cano et al., 2011a).

[b]: Post-break slope fitted to the smooth function with broken power-law method.

(1) Blustin et al. (2006), (2) Della Valle et al. (2006), (3) Cano et al. (2011a)

Except for two long GRBs, i.e., GRB 060614 (Fynbo et al., 2006; Gal-Yam et al., 2006; Gehrels et al., 2006) and GRB 060505 (Fynbo et al., 2006; McBreen et al., 2008; Ofek et al., 2007), for which no associated SNe were detected, there are no other known cases of long duration GRBs for which the limits on detecting a SN rules out something that is about as bright as SN 1998bw (Hjorth & Bloom, 2012).

GRBs are very luminous and energetic with isotropic energies up to $E_{\gamma,iso} \sim 10^{54}$ erg (Hjorth & Bloom, 2012; Xu et al., 2013). Soon after the burst, the flux of the GRB afterglow dominates the light, but it declines rapidly. In some cases, after a few days, the brightness of an afterglow will have decreased significantly and is no more a major contributor to the photometry. At this time, if the host galaxy is not brighter than the SN, usually we can observe the light from the SN.

We assume that the afterglow behaves as a power law or a broken power-law decay $f(t) = c_1 t^{\beta_1}$ for $t < t_{\rm break}$ and $f(t) = c_2 t^{\beta_2}$ for $t \geqslant t_{\rm break}$, where $f(t)$ is the flux of an afterglow, β_1 and β_2 are the decay slopes and $t_{\rm break}$ is the time for the change of the slopes from pre-break β_1 to post-break β_2. We choose $t_{\rm break}$ based on the data or from the literature. This method is different from the broken power-law fits (Cano et al., 2011a; Zeh et al., 2004), but the effect is similar. The slopes, the break time for systems GRB 050525A and GRB 090618 (see section 3.3 for more discussion on each system) are listed in Table 3.1. The values of $\bar{t}_{\rm break}$, $\bar{\beta}_1$ and $\bar{\beta}_2$ in the column of 'smooth function' are from the literature, while in the 'broken power-law' column, the value of β_2 is used in this paper.

When the results of the smooth function are fitted with a broken power-law way, $\widehat{\beta}$ is the fitted post-break slope. Compare $\widehat{\beta}$ and β_2, we conclude that the broken power-law fits is consistent with the results of broken power-law fits.

In this paper, we resimulate the afterglow data with the standard Monte Carlo method and fit the resimulated data with broken power-law functions. We remove the contribution of the afterglow by subtracting the fitted power-law functions.

3.2.3 EXTINCTION, DISTANCE MODULUS, AND REST FRAME TIME

Dust in galaxies reddens light emitted from GRB-SNe. There are two main contributing sources: dust in the host galaxy, where the GRB-SN is located, and dust in the Milky Way. In this paper, we take the values of host extinction, e.g., $A(V)_{\rm host}$ or $E(B-V)_{\rm host}$, from the literature. Schlafly & Finkbeiner (2011) found that the Galactic extinction is overestimated by DIRBE/IRAS dust map (Schlegel et al., 1998) and calculated the correction coefficients if the dust map is used. In this paper, with $R_V = 3.1$, we use the DIRBE/IRAS dust map (Schlegel et al., 1998) to get $E(B-V)$, then the coefficients (see Table 6 in Schlafly & Finkbeiner (2011)) are multiplied to correct the value.

The distance modulus is calculated and subtracted to obtain the absolute magnitude. In this paper, we adopt the cosmological parameters $\{\Omega_m, \Omega_\Lambda\} = \{0.315, 0.685\}$ and $H_0 = 67.3$ km s^{-1} Mpc^{-1} in a flat universe (Planck Collaboration et al., 2013). The absolute magnitude is determined as

$$M = m - 5\log_{10}(D_L/10{\rm pc}) - \Delta K_{\rm total} - \Delta A, \tag{3.1}$$

where D_L denotes the luminosity distance, $\Delta K_{\rm total}$ represents the total effect of the K-correction (section 3.2.5 and Eq. 3.7) and ΔA represents the correction for dust extinction.

Peculiar velocities may affect the estimate of the distance modulus, especially for nearby SNe. Except for SN 1998bw which has peculiar velocity $v_p = -65 \pm 75$ km s^{-1} (Li et al., 2014), for the other systems we assume the peculiar velocity is 0 and the uncertainty is $\delta v_p = 300$ km s^{-1} (Davis , 2013). Therefore, the uncertainty in the distance modulus is $(5/2.3)\,\delta v_p\,(cz)^{-1}$, where c is the speed of light and z is the redshift of a GRB-SN.

It is straightforward to convert the observational time into the rest frame time by dividing the observational time by $(1+z)$.

3.2.4 POLYNOMIAL FUNCTION FITTING

After the steps discussed above, polynomial functions are fitted to the data. We fit the data with the lowest possible order. The most suitable order is to some extent subjective, but as discussed below, in most cases the polynomial functions are of 3rd or 4th order. Data on both sides of the peak are needed. This is to ensure that parameters dependent on sampling the peak, such as the time of peak, the peak brightness, and the decline rate past peak, are robustly determined.

3.2.5 K-CORRECTION

The observational data of GRB-SNe may be in U, B, V, R, I and other bands. After subtracting the host and afterglow brightness and fitting polynomial functions to the results, light curves of SNe are obtained in the observed bands. Then a K-correction is applied to correct light curves from the observed band(s) into the rest frame V band. If the systems have been observed in two or more bands and two bands are close to the redshifted V band for interpolation, then a 'multi-band K-correction' (Hogg et al., 2002; van Dokkum & Franx, 1996) is applied. For the other systems, which have data in only one band or the other bands are not close to the redshifted V band, we correct their peak magnitude and decline rate with peak SED and decline rate templates based on SN 1998bw. We use broad-band data because we do not have useful spectra around (before and after) the peak of the light curve. We stress that we do not use SN 1998bw as a template for the light curve or the SED. We use SN 1998bw to obtain a 2nd order correction once a model independent magnitude close to the V band has been obtained. This effect does not require that the overall light curves or spectra are perfectly identical to those of SN 1998bw.

Multi-band K-correction

The multi-band K-correction is a method to constrain the light curves in the rest frame V band by interpolating two light curves in adjacent observed bands (Hogg et al., 2002; van Dokkum & Franx, 1996). The method is based on the assumption that flux densities are correlated in contiguous bands. For example, if a GRB-SNe has $z \in (0.26, 0.60)$, then we can interpolate the magnitude in the R and I bands into the redshifted V band. The flux density in the V band can be estimated as: $F(\nu_V(z)) = F(\nu_R)^c F(\nu_I)^{1-c}$. The magnitude in the redshifted V band is then

$$V_z = kR + (1-k)I, \tag{3.2}$$

where V_z, R and I are magnitudes in the AB system. The parameter k is calculated as a function of central wavelength of the observed bands and the SN redshift (van Dokkum & Franx, 1996). Here $k = (\lambda_I - \lambda_V(1+z))/(\lambda_I - \lambda_R)$ with λ_R and λ_I being the observational R and I band wavelengths and $\lambda_V(1+z)$ being the redshifted V band wavelength. In this step, the selected two bands should fulfill the conditions: 1) the two bands must be adjacent; 2) the parameter should be $c \in (0, 1)$ to make sure one is not extrapolating beyond the observed bands.

SN 1998bw peak SED and decline rate templates

When useful light curve data is available only in one band, or the other observed bands are too far away from the redshifted V band to do a meaningful multi-band K-correction, we resort to using the light curves of SN 1998bw as a template to obtain V-band values from data close to the redshifted V band, typically within a few hundred Å. The observed

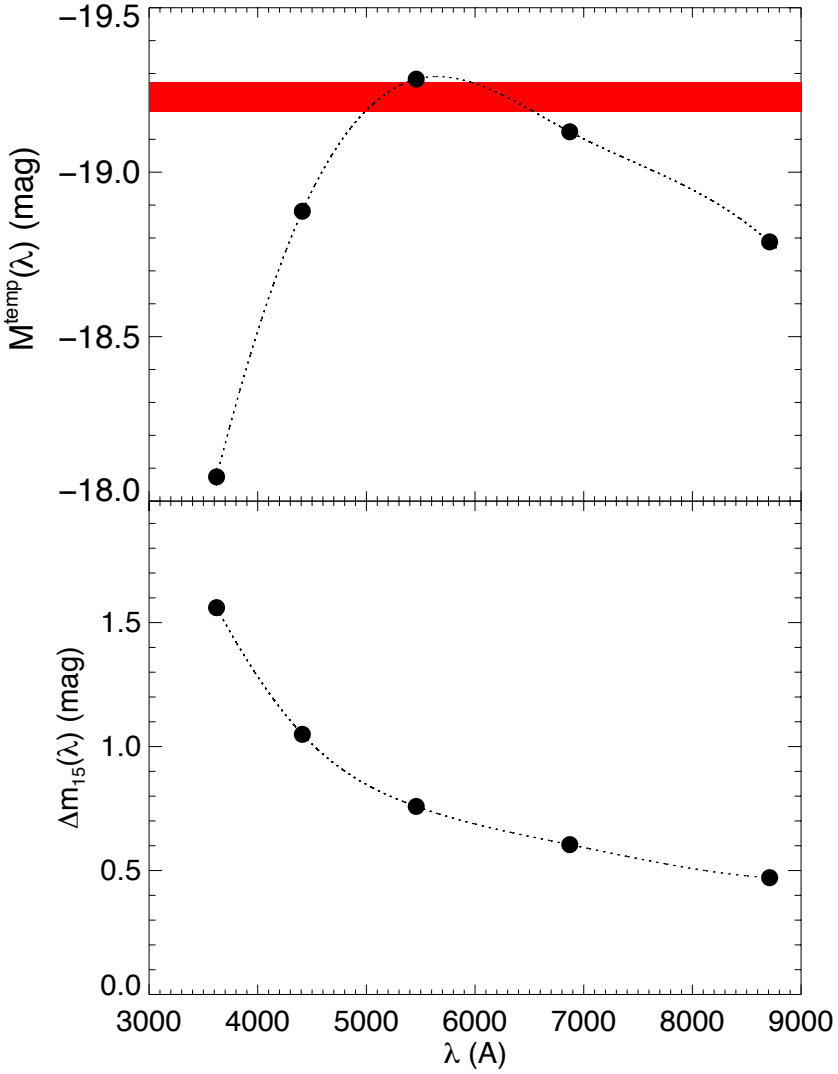

Figure 3.1: SN 1998bw peak SED and decline rate templates. The black points represent values in the U, B, V, R, I bands (Clocchiatti et al., 2011; Galama et al., 1998; Sollerman et al., 2002). The dotted lines are the 4th order polynomial functions fitted to the templates. The upper panel shows the relation between the wavelength λ and the peak magnitude $M^{\rm temp}(\lambda)$. The rectangular region in red marks the difference Δ (Eq. 3.4) between the two K-correction methods used in this paper. More details are in Section 3.2.5 and Figure 3.2. In the lower panel, the relation between the wavelength λ and the decline rate $\Delta m_\alpha(\lambda)$ is plotted. Here we show values for $\alpha = 15$. $M^{\rm temp}(\lambda)$ values have errors < 0.02 mag while Δm_{15} values have errors < 0.026 mag in the V, R and I bands.

band which is closest to the redshifted V band is chosen to obtain the light curves and measure the values of the peak magnitude and the decline rate. After that, according to the wavelength of the chosen band, $M_{\rm V,peak}$ and $\Delta m_{{\rm V},\alpha}$ are corrected to the rest frame V band using the light curves of SN 1998bw as a template.

The SN 1998bw peak SED and decline rate templates describe the relations of $M_{\rm peak}$ and Δm_α, as a function of wavelength λ. It is based on the assumption that the behavior of the light curves in different bands are similar for all GRB-SNe.

Here we use the observational data of SN 1998bw (Clocchiatti et al., 2011; Galama et al., 1998; Sollerman et al., 2002) to establish the template (see section 3.3.1 for details on SN 1998bw). The light curves are well defined by the observational data. Therefore, peak magnitudes $M_{\rm peak}$ and the decline rates Δm_α are constrained in the U, B, V, R, I bands. Then we fit 4th order polynomial functions to the relations between $M_{\rm peak}$, Δm_α and λ. The resulting templates are shown in Figure 3.1. The relation between $M_{\rm peak}$ and wavelength λ is

$$\begin{aligned} M^{\rm temp}(\lambda) &= -4.51 - 6.8\cdot 10^{-3}\lambda + 1.05\cdot 10^{-6}\lambda^2 \\ &\quad - 5.75\cdot 10^{-11}\lambda^3 + 6.09\cdot 10^{-16}\lambda^4, \end{aligned} \tag{3.3}$$

where λ represents the wavelength in $\mathring{A}$. With the templates, the peak magnitude of a GRB-SN is corrected as $M_{\rm V,peak} = M_\lambda^{\rm data} - M_\lambda^{\rm temp} + M_V^{\rm temp}$, where $M_\lambda^{\rm data}$ represents the peak magnitude at the wavelength $\lambda = \lambda_{\rm obs}/(1+z)$, with $\lambda_{\rm obs}$ being the observational wavelength, while $M_\lambda^{\rm temp}$ and $M_V^{\rm temp}$ denote the measured values at the wavelength λ and in the V band respectively, obtained from the SN 1998bw peak SED and decline rate templates. The decline rate $\Delta m_{{\rm V},\alpha}$ is corrected in the same way.

Comparing the two K-correction methods

The difference between the two K-correction methods is

$$\Delta = M_{\rm V,peak}^{\rm temp} - M_{\rm V,peak}^{\rm multi}, \tag{3.4}$$

where $M_{\rm V,peak}^{\rm temp}$ denotes the peak magnitude estimated via the SN 1998bw peak SED and decline rate templates, and $M_{\rm V,peak}^{\rm multi}$ is the value obtained from the multi-band K-correction. We define $d_{\rm wave}^{\rm obs}$ as the distance from the bluer observed band to the redshifted V band in units of $\mathring{A}$, so $d_{\rm wave}^{\rm rest} = d_{\rm wave}^{\rm obs}/(1+z)$, where $d_{\rm wave}^{\rm rest}$ denotes the distance from the rest frame bluer band to the rest frame V band. Therefore, from Eq. 3.2, the peak magnitude estimated from the multi-band K-correction is

$$\begin{aligned} M_{\rm V,peak}^{\rm multi} &= kM_{\rm peak}(V_{\rm wave}^{\rm rest} - d_{\rm wave}^{\rm rest}) \\ &\quad + (1-k)M_{\rm peak}\left(V_{\rm wave}^{\rm rest} + \frac{k}{1-k}d_{\rm wave}^{\rm rest}\right), \end{aligned} \tag{3.5}$$

where $V_{\rm wave}^{\rm rest}$ is the wavelength of the rest-frame V band in units of $\mathring{A}$. Here $M_{\rm peak}(V_{\rm wave}^{\rm rest} - d_{\rm wave}^{\rm rest})$ is the peak magnitude in the rest-frame bluer band, with the band having $d_{\rm wave}^{\rm rest}$

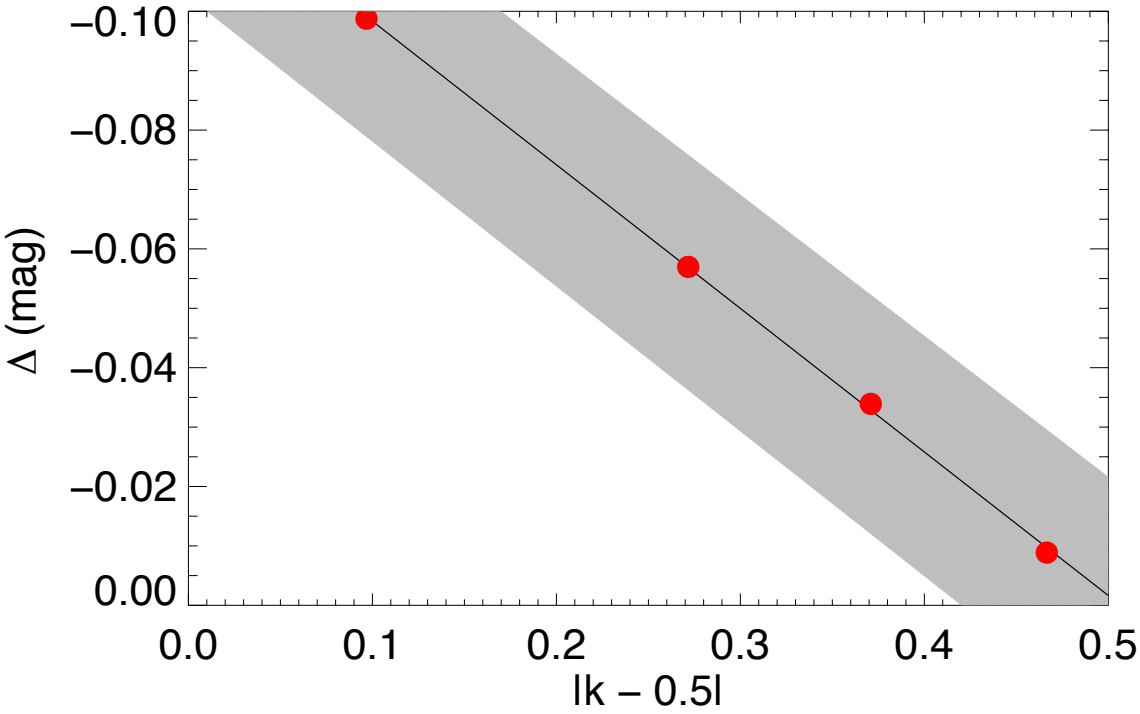

Figure 3.2: The difference of peak magnitude (Δ) estimated via two K-corrections as a function of K-correction factor k (Eqs. 3.2 and 3.6) for four systems: SN 1998bw, SN 2006aj, SN 2010bh and SN 2012bz (see section 3.3 for details). The shaded area shows the systematic uncertainty of 0.02 mag in the K correction procedure.

distance to the rest-frame V band ($V^{\rm rest}_{\rm wave}$). The value of $M_{\rm peak}(V^{\rm rest}_{\rm wave} + kd^{\rm rest}_{\rm wave}/(1-k))$ represents the peak magnitude in the rest-frame redder band, where $kd^{\rm rest}_{\rm wave}/(1-k)$ is the distance between the rest-frame redder band and the rest-frame V band.

Combining the results in Figure 3.1 and Eqs. (3.4) and (3.5), Δ is dependent on two parameters: k and $d^{\rm rest}_{\rm wave}$. The value of Δ may get larger as k is closer to 0.5 and $d^{\rm rest}_{\rm wave}$ is larger, i.e., the redshifted V band is closer to the middle point of two observed bands, as well as the distances between two observed bands and the redshifted V band is larger. In this paper, $kd^{\rm rest}_{\rm wave} < 270\mathring{A}$. Within this small range, a linear relation between Δ and $|k-0.5|$ is

$$\Delta = 0.24 \cdot |k - 0.5| - 0.12. \tag{3.6}$$

Figure 3.2 shows that two methods lead to small differences with $|\Delta| \leqslant 0.1$ mag for four systems: SN 1998bw, SN 2006aj, SN 2010bh and SN 2012bz (see section 3.3 for more discussion on each system). For these four systems, the difference Δ is small and $kd^{\rm rest}_{\rm wave} < 270\mathring{A}$. When $k = 0.5$, the redshifted V band is exactly the average of two observed bands. In that case, the difference between the two K-correction methods is the largest.

The peak of $M^{\rm temp}(\lambda)$ on the SN 1998bw peak SED and decline rate templates is around 5500 $\mathring{A}$, which is close to the V band. Therefore, the multi-band K-correction, obtained by interpolating magnitudes on each side of the peak, may underestimate the value of $M_{\rm V,peak}$. We therefore apply the modification (Eq. 3.6) to the multi-band K-correction. We adopt a systematic uncertainty of 0.02 mag in quadrature in the K-correction after applying this modification, as shown in the shaded area in Figure 3.2. The total K-correction is defined as

$$\Delta K_{\rm total} = \Delta K_{\rm corr} - 2.5\log(1+z), \tag{3.7}$$

where $\Delta K_{\rm total}$ is the total K-correction, $\Delta K_{\rm corr}$ represents the multi-band K-correction or the correction from the SN 1998bw peak SED and decline rate templates.

3.3 SYSTEMS OF GRB-SNE

Based on the degree of observational evidence of a GRB having an associated SN (Hjorth & Bloom, 2012), GRB-SNe are graded from class *A* to class *E*, where class *A* has 'strongest spectroscopic evidence', while class *E* has the weakest evidence. In this paper, we select GRB-SN candidates in classes *A*, *B*, and *C*. In total 21 systems are collected (see Table 9.1 in Hjorth & Bloom 2012), including SN 2012bz (Schulze et al., 2014) which is classified as a class *A* system and GRB 120714B/SN 2012eb (Klose et al., 2012) which is classified as a class *C* system.

We have studied all the 21 GRB-SN systems and evaluated the feasibility of constraining model-independent peak magnitudes and decline rates for them. Among them, we succeed to measure $M_{\rm V,peak}$ and $\Delta m_{{\rm V},\alpha}$ for 8 systems, as listed in Table 4.1, along with the corrections made in each case. We address the other systems and the reasons why they are not selected in section 3.3.9.

Table 3.2: The selected systems and the relevant steps.

GRB/XRF/SN	afterglow[a]	host[b]	k/t[c]	class	reference
980425/1998bw	-	-	k	A	(1), (2), (3)
030329/2003dh	-	-	t	A	(4), (5)
031203/2003lw	-	$\surd$	t	A	(6), (7), (8)
050525A/2005nc	$\surd$	$\surd$	t	B	(9), (10)
060218/2006aj	-	$\surd$	k	A	(11), (12), (13), (14), (15)
090618	$\surd$	$\surd$	t	C	(16)
100316D/2010bh	-	-	k	A	(17), (18), (19)
120422A/2012bz	$\surd$	-	k	A	(20), (21)

[a]: Subtraction of afterglow brightness.
[b]: Subtraction of host galaxy brightness.
[c]: Multi-band K-correction (denoted 'k') or shift based on the SN 1998bw peak SED and decline rate templates (denoted 't').
(1) Galama et al. (1998), (2) Sollerman et al. (2002), (3) Clocchiatti et al. (2011), (4) Hjorth et al. (2003), (5) Matheson et al. (2003), (6) Malesani et al. (2004), (7) Mazzali et al. (2006), (8) Malesani (2013), (9) Blustin et al. (2006), (10) Della Valle et al. (2006), (11) Sollerman et al. (2006), (12) Ferrero et al. (2006), (13) Šimon et al. (2010), (14) Guenther et al. (2006), (15) Poznanski et al. (2012), (16) Cano et al. (2011a), (17) Cano et al. (2011b), (18) Olivares E. et al. (2012), (19) Bufano et al. (2012), (20) Melandri et al. (2012), (21) Schulze et al. (2014).

3.3.1 GRB 980425/SN 1998BW

SN 1998bw was the first SN discovered to be connected with a GRB, GRB 980425 (Galama et al., 1998). Combined with the peculiar velocity $v_p = -65 \pm 75$ km s^{-1} (Li et al., 2014) and the CMB velocity $v_{\rm CMB} = 2505 \pm 14$ km s^{-1} (Foley et al., 2006), it has $v_z = 2570 \pm 76$ km s^{-1}. The redshift is $z = v_z/c = 0.00857 \pm 0.00025$. It is by far the lowest redshift of GRB-SNe. A lot of work have been done on this system, which is why we have built the peak SED and decline rate templates based on this system. This system is a class A GRB-SNe.

We collect the data in the V and R bands (Clocchiatti et al., 2011; Galama et al., 1998; Sollerman et al., 2002). We assume that the host galaxy and afterglow contributions to the total brightness are negligible and fit 4th order polynomials to the light curves. We have enough data in the V and R bands and these two bands are close to the redshifted V band, so the multi-band K-correction is applied. The parameter in the K-correction is $k = 0.97$. We assume that the host extinction is negligible. Unless stated otherwise, we treat GRB-SNe in the same way and neglect the contributions from the host galaxy, the afterglow or the host extinction, if they are not mentioned in the literature. The Galactic extinction is estimated to be $E(B-V) = 0.06$ mag. The distance modulus is $\mu = 32.94 \pm 0.08$. The uncertainty in the distance modulus is dominated by the uncertainty in the peculiar velocity.

Figure 3.3 shows the light curves of SN 1998bw. In the upper panel, the observational data, the resimulated data and the fitting functions to the resimulated data in the V (left) and R (right) bands are plotted. In the lower panel, the left plot shows the light curves in the V and R bands, after correcting for the Galactic extinction and converting into the absolute magnitude. On the right, after the K-correction, the light curves in the rest frame V band are plotted. The temporal axes in the four panels have been corrected into the rest frame. The uncertainties in the resimulated data and the fitting light curves are plotted as 68.3% ($\pm 1\sigma$) of the total resimulated results. In this section, the similar figures show 100 out of the 1000 resimulated light curves.

3.3.2 GRB 030329/SN 2003DH

The GRB 030329/SN 2003dh system was the first solid spectroscopic association between a cosmological GRB and a SN (Hjorth et al., 2003; Stanek et al., 2003). The redshift is $z = 0.1685$. It is a class A system. The data is collected in the V band (Hjorth et al., 2003). The spectra was decomposed, and the SN spectra was obtained (Hjorth et al., 2003). With an SMC extinction law, Matheson et al. (2003) estimated the host extinction to be $A_{\rm V,host} = 0.12 \pm 0.22$ mag. The Galactic extinction is $E(B-V)_{\rm MW} = 0.025$ mag and the distance modulus is $\mu = 39.63 \pm 0.01$. Due to the small number of data points, we fit 2nd order polynomial functions to the resimulated data. The $M_{\rm V,peak}$ and $\Delta m_{\rm V,15}$ for this system are corrected with the SN 1998bw peak SED and decline rate templates. The results are shown in Figure 3.4 (left).

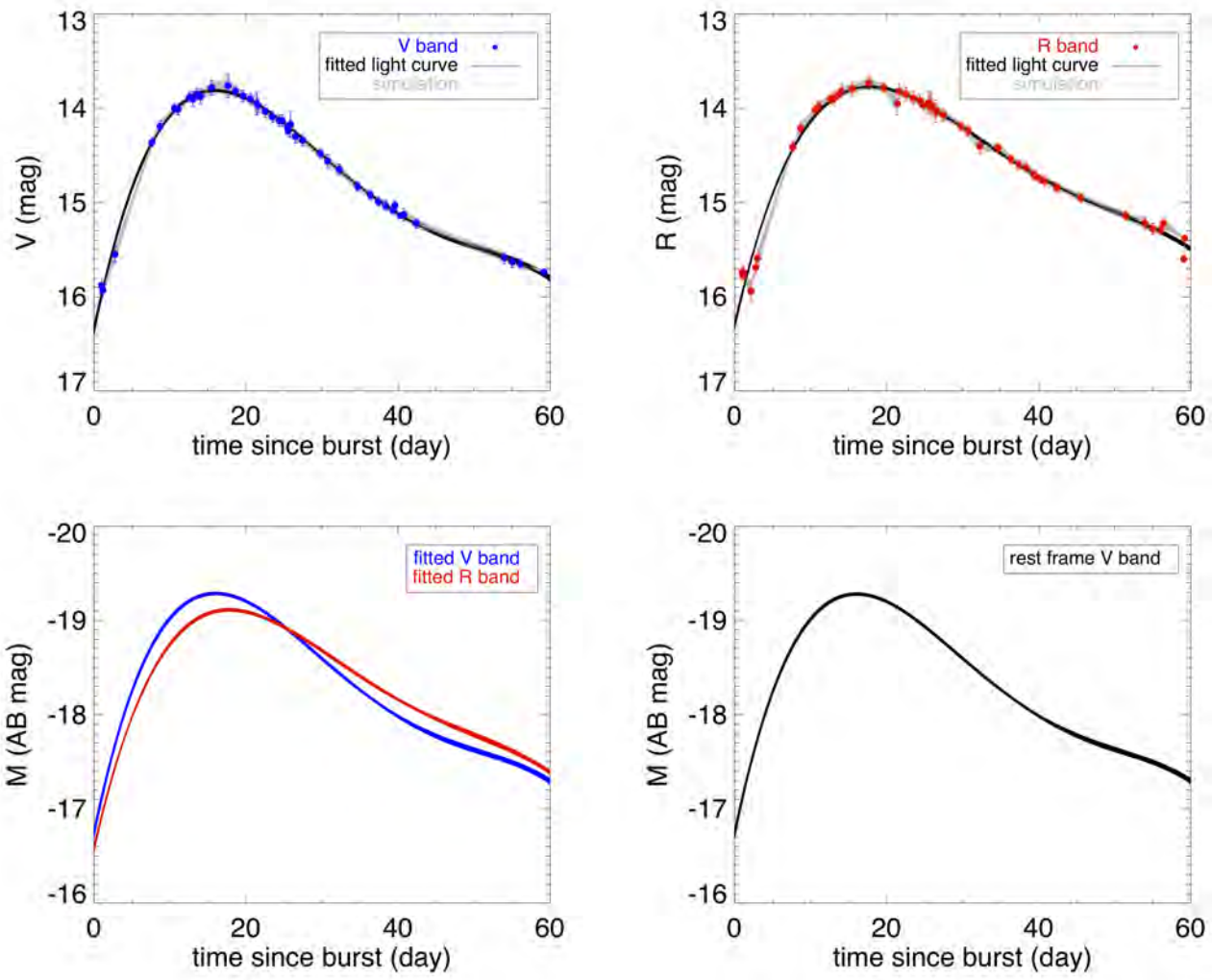

Figure 3.3: GRB 980425/SN 1998bw. The upper panels show the photometric data points (blue/red), the resimulated data (gray) and the polynomial functions fitted to the resimulated data in V (*left*) and R (*right*) bands. In the lower left panel, the light curves after the extinction, the K-correction and the distance modulus correction are plotted in V band (blue) and R band (red) in AB magnitude. In the lower right panel, the final light curves after the multi-band K-correction (Eq. 3.2) in the rest frame V band are plotted. The uncertainties in the resimulated data and the fitting light curves are plotted as 68.3% ($\pm 1\sigma$) of the total resimulated results.

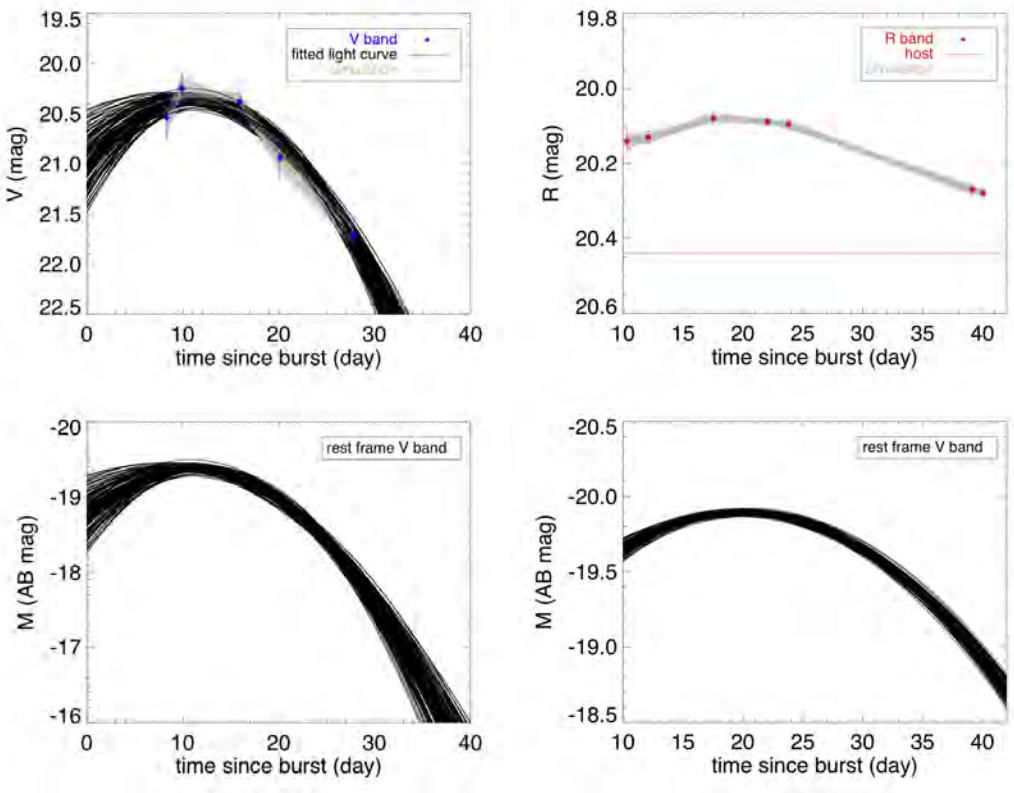

Figure 3.4: GRB 030329/SN 2003dh (*left*) and GRB 031203/SN 2003lw (*right*). The line styles are the same as in Figure 3.3.

3.3.3 GRB 031203/SN 2003LW

GRB 031203 (SN 2003lw) had a very faint afterglow and a relatively bright host galaxy with $\mathrm{V_{host}} = 20.57 \pm 0.05$ mag and $\mathrm{R_{host}} = 20.44 \pm 0.02$ mag (Malesani, 2013; Mazzali et al., 2006). It is a class A system.

The redshift is $z = 0.1055 \pm 0.0001$ (Prochaska et al., 2004). We collect data in the V and R bands (Malesani et al., 2004; Mazzali et al., 2006).

The observed fluxes are corrected for the significant host contribution. After that, we fit 2nd order polynomial functions to the resimulated data. Unfortunately, the V band data do not cover the rising part of the light curve. Therefore, only the R band data is used to generate the light curves. This system has uncertain extinction. From Prochaska et al. (2004), a lower Galactic extinction is adopted to be $E(B-V)_{\mathrm{MW}} = 0.78$ mag, and total extinction is $E(B-V)_{\mathrm{total}} = 1.17 \pm 0.1$ mag, through Balmer line ratio study. Through spectral modeling, (Mazzali et al., 2006) favors a value of the host extinction $E(B-V)_{\mathrm{host}} = 0.25$ mag and $A_{\mathrm{V,host}} = 0.78 \pm 0.16$ mag (Cardelli et al., 1989) and total reddening $E(B-V)_{\mathrm{total}} \sim 1.07 \pm 0.05$ mag. We adopt the Galactic extinction to be $E(B-V)_{\mathrm{MW}} = 1.06$ mag and the host extinction to be $A_{\mathrm{V,host}} = 0.78 \pm 0.16$ mag from Mazzali et al. (2006). We consider the peak magnitudes are uncertain values, because the host extinction is uncertain. The distance modulus is $\mu = 38.52 \pm 0.02$. The $M_{\mathrm{V,peak}}$ and $\Delta m_{\mathrm{V},15}$ for this system are corrected with the SN 1998bw peak SED and decline rate templates. The results are shown in Figure 3.4 (right).

3.3.4 GRB 050525A/SN 2005NC

GRB 050525A (SN 2005nc) is a long GRB with redshift $z = 0.606$ (Blustin et al., 2006). It is a class B system.

We collect data from Della Valle et al. (2006). Only R band data is available. Therefore, the SN 1998bw peak SED and decline rate templates are applied. We subtract the host contribution with $\mathrm{R_{host}} = 25.2 \pm 0.1$ mag (Della Valle et al., 2006). Then we resimulate and subtract the afterglow data, fitted as a broken power-law, to get the intrinsic SN flux. After that, we fit 3rd order polynomial functions to the resimulated data. The host extinction is estimated to be $A_{\mathrm{V,host}} = 0.26 \pm 0.12$ mag (Blustin et al., 2006; Cardelli et al., 1989; Pei, 1992), assuming an SMC extinction curve. For the Galactic extinction, the foreground extinction is $E(B-V)_{\mathrm{MW}} = 0.094$ mag. The distance modulus is $\mu = 42.84 \pm 0.004$. Figure 3.5 (left) shows the results for SN 2005nc.

3.3.5 XRF 060218/SN 2006AJ

The X-Ray Flash (XRF; Heise et al., 2001) 060218 is a long GRB. The redshift is $z = 0.03342$. This system is another class A GRB-SN.

We collect data from Sollerman et al. (2006), Ferrero et al. (2006), and Šimon et al. (2010) in the V and R bands. SN 2006aj is an extreme case (Šimon et al., 2010) because before a normal SN peak, there is an early peak and these two peaks are equally bright.

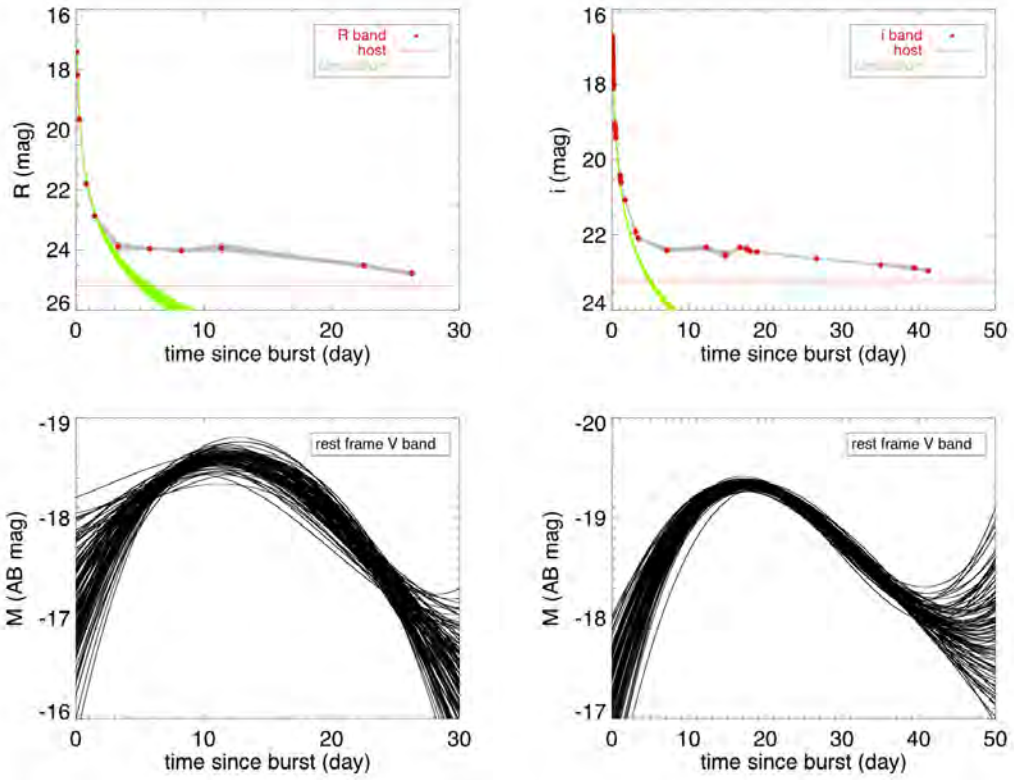

Figure 3.5: GRB 050525A /SN 2005nc (*left*) and GRB 090618 (*right*). The line styles are the same as in Figure 3.3. The green lines are the broken power-law functions fitted to the afterglow.

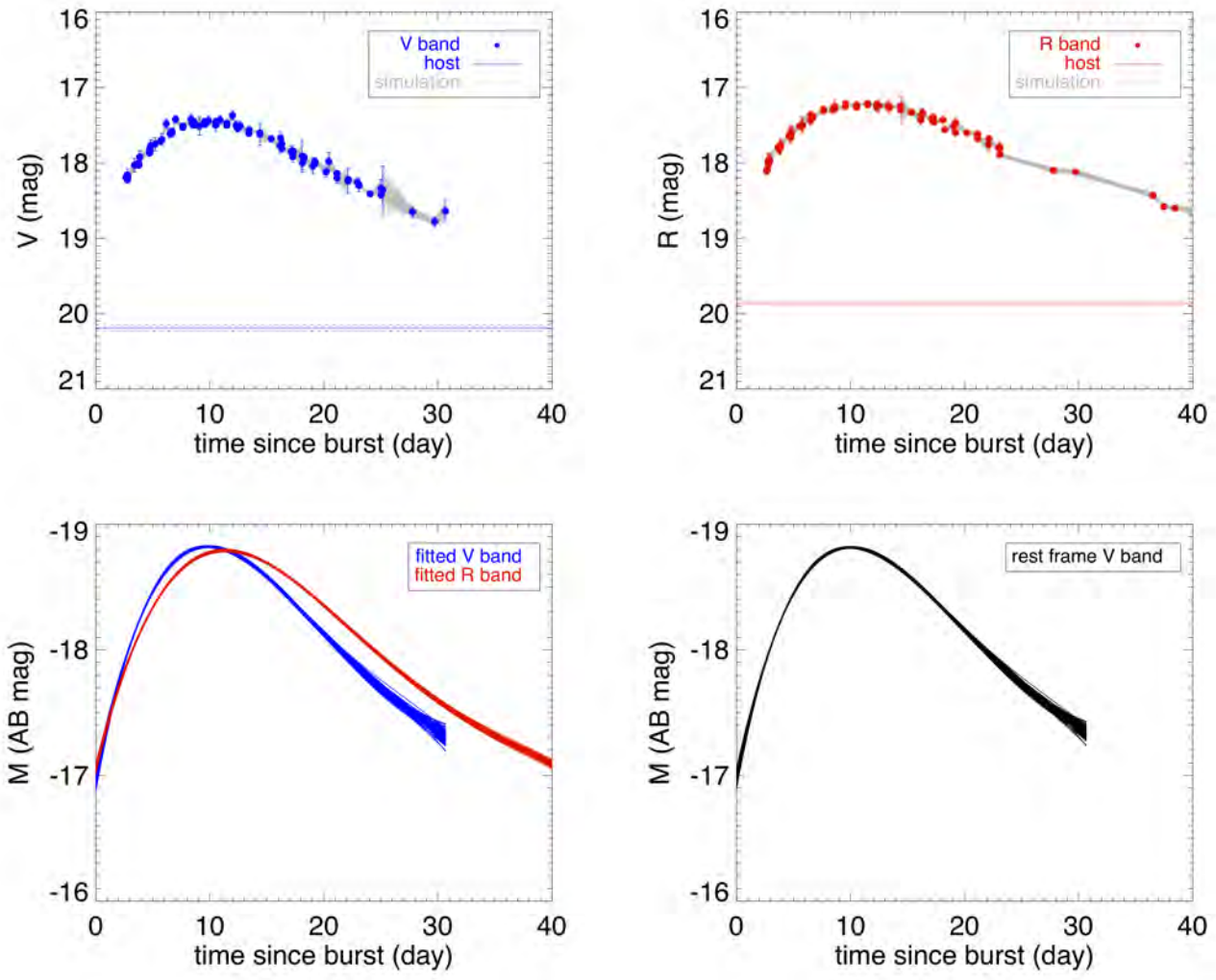

Figure 3.6: XRF 060218 (SN 2006aj). The line styles are the same as in Figure 3.3.

The data from Šimon et al. (2010) includes the early part (< 2.5 days) of the photometry since the burst, therefore the light curve shows two bumps. In this paper, we study the normal SN light curve so we only collect the data after 2.5 days since the burst.

SN 2006aj is located in a relatively bright host galaxy with $\mathrm{V_{host}} = 20.19 \pm 0.04$ mag and $\mathrm{R_{host}} = 19.86 \pm 0.03$ mag (Sollerman et al., 2006), which are subtracted from the observed fluxes. The distance modulus is $\mu = 35.92 \pm 0.07$. We fit 4th order polynomial functions. There is a discrepancy in the reported estimates of the host extinction. Campana et al. (2006) estimate it to be $E(B-V)_{\rm host} = 0.2 \pm 0.03$ mag, assuming an SMC reddening law. Assuming the relation between sodium absorption and dust extinction from Munari & Zwitter (1997) is representative for interstellar medium, Guenther et al. (2006) find $E(B-V)_{\rm host} = 0.042 \pm 0.003$ mag. With an updated empirical relation from Poznanski et al. (2012), the extinctions are $E(B-V)_{\rm host} = 0.026 \pm 0.014$ mag and $E(B-V)_{\rm MW} = 0.061 \pm 0.03$ mag, which are about half of the values from Munari & Zwitter (1997). We adopt the Galactic extinction is $E(B-V)_{\rm MW} = 0.145$ mag. The host extinction is estimated to be $E(B-V)_{\rm host} = 0.026 \pm 0.014$ mag and $A_{\rm V,host} = 0.076 \pm 0.041$ mag with the updated empirical relation from Poznanski et al. (2012). We apply the multi-band K-correction with $k = 0.87$. Figure 3.6 shows the light curves of SN 2006aj.

3.3.6 GRB 090618

The long GRB 090618 is a class C system with $z = 0.54$ (Cano et al., 2011a). We collect data from Cano et al. (2011a) in the i band. We subtract the brightness of the host galaxy and the afterglow. The host brightness is estimated to be $i_{\rm host} = 23.22 \pm 0.06$ mag (Cano et al., 2011a). The afterglow is fitted with broken power-law functions and the resimulated data are fitted with 3rd order polynomial functions. The Galactic extinction is $E(B-V)_{\rm MW} = 0.09$ mag. From X-ray to optical SED fitting, the host extinction is $A_{\rm V,host} = 0.3 \pm 0.1$ mag according to Cano et al. (2011a). The distance modulus is $\mu = 42.54 \pm 0.004$. The SN 1998bw peak SED and decline rate templates are used to convert the peak magnitude and the decline rates into the rest frame V band. Figure 3.5 (right) shows the results for GRB 090618.

3.3.7 XRF 100316D/SN 2010BH

XRF 100316D is a soft long GRB (Cano et al., 2011b). It is a class A system. The redshift is $z = 0.059$ and we use published photometry in the V and R bands (Bufano et al., 2012; Cano et al., 2011b; Olivares E. et al., 2012). The three data sets are not consistent with each other (shown in Figure 3.7). There are systematic offsets in the photometry, especially around the peak. Compared to Bufano et al. (2012) and Cano et al. (2011b), the R band data from Olivares E. et al. (2012) is about 0.3 mag fainter at the peak. This may because of zero point discrepancies. We reduce the offset by subtracting 0.3 mag from the R band data (Olivares E. et al., 2012), although we acknowledge there is a possibility that the other two data sets should be shifted instead.

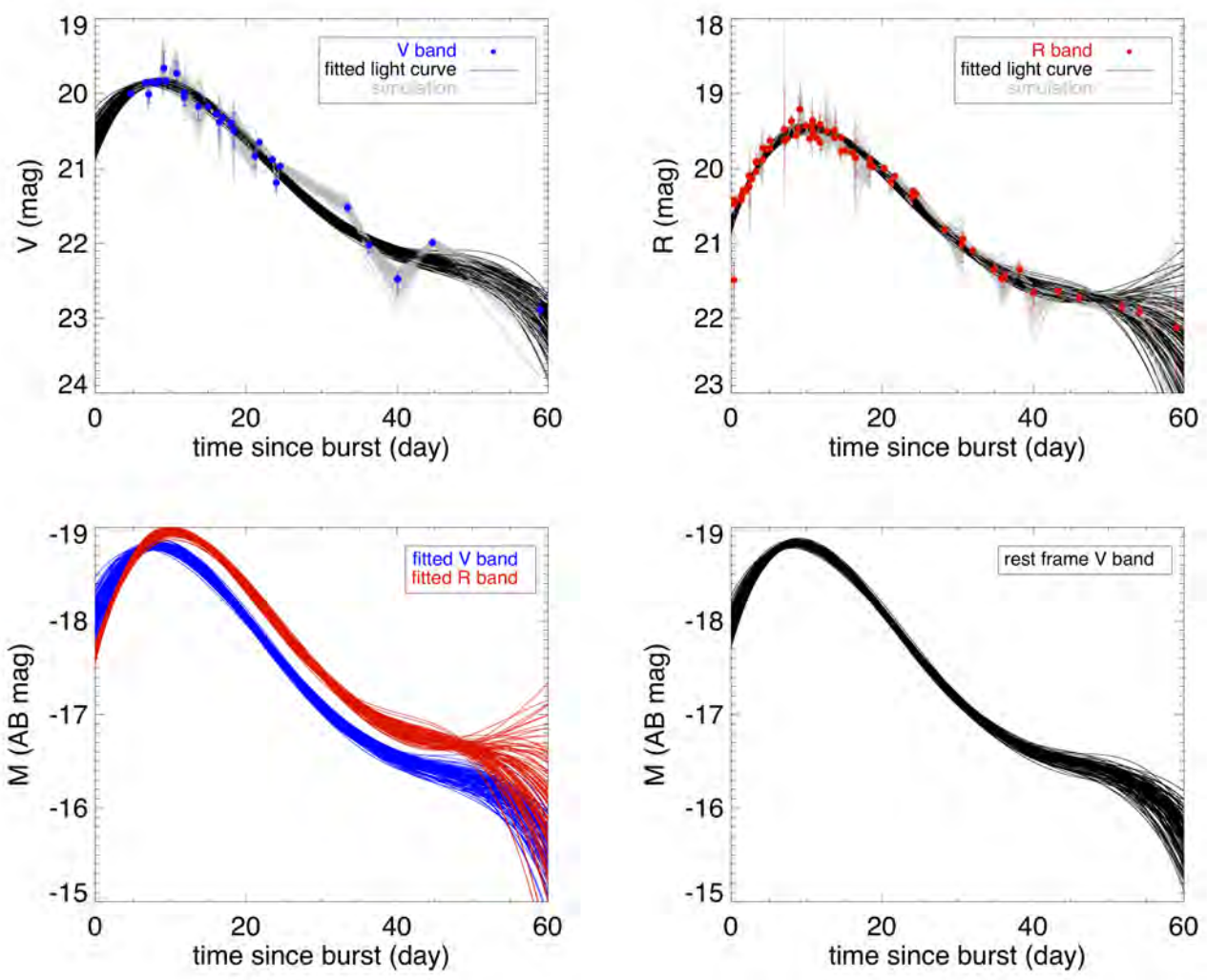

Figure 3.7: XRF 100316D/SN 2010bh. The line styles are the same as in Figure 3.3.

The foreground extinction is $E(B-V)_{\rm MW} = 0.117$ mag. Reported values of the host extinction are very different. Using the Hα/Hβ ratio, the host extinction is estimated to be $E(B-V)_{\rm host} = 0.14$ mag (Bufano et al., 2012). From color excess measurement, Cano et al. (2011b) assumes the host extinction to be $E(B-V)_{\rm host} = 0.18 \pm 0.08$ mag. Olivares E. et al. (2012) estimated the extinction using afterglow SED fitting and found $A_{\rm V,host} = 1.20 \pm 0.09$ mag. We adopt this value because the intrinsic SN spectrum is otherwise very red (Levan et al. (2013)). However, we consider the peak magnitude an uncertain value because of the possible zero point errors in the photometry and the uncertain extinction correction.

The distance modulus is $\mu = 37.20 \pm 0.04$. We fit 4th order polynomial functions to the resimulated data. The multi-band K-correction parameter is $k = 0.77$. Figure 3.7 shows the resulting light curves for SN 2010bh.

3.3.8 GRB 120422A/SN 2012BZ

Extensive observations have been done to detect GRB 120422A (SN 2012bz) with telescopes from mm to optical wavelengths (Melandri et al., 2012; Schulze et al., 2014). It is a class A system.

The redshift is $z = 0.283$, and the data are collected from Melandri et al. (2012); Schulze et al. (2014) in the r′ and i′ bands. Compared to the X-ray lightcurve (Fig. 2 in Schulze et al. (2014)), the afterglow in the r′ and i′ bands have a significant supernova contribution, so we fix the the post-break slope $\beta = 1.48 \pm 0.4$ based on the X-ray observations (Schulze et al., 2014). But the subtraction of the afterglow barely changes the intrinsic SN brightness. So for this system, either we fix the slope based on X-ray observation or on the SN modeling have no difference to the brightness of the SN (Schulze et al., 2014). We adopt the foreground extinction to be $E(B-V)_{\rm MW} = 0.035$ mag. The resimulated data are fitted with 4th order polynomial functions. The distance modulus is $\mu = 40.89 \pm 0.01$. The multi-band K-correction parameter is $k = 0.40$. Figure 3.8 shows the light curve results.

3.3.9 GRBS NOT INCLUDED

We investigated the possibilities of obtaining light curves for other GRB-SNe in class A, B and C. Here we briefly explain the reasons why we do not report the light curves for these systems.

There are several reasons that may cause the failure of obtaining the light curves in the rest frame V band: 1) The errors in the subtraction of the afterglow will inflate the errors in the SN photometry. This is a major reason why for some systems, even though enough data points have been obtained, after the afterglow fitting, there are too few useful data points left to do the polynomial fitting. We cannot get full light curves (notably information at and before the peak) for these systems. 2) Some systems lack data in proper band(s) to do the K-correction. This is because the multi-band K-correction is only valid

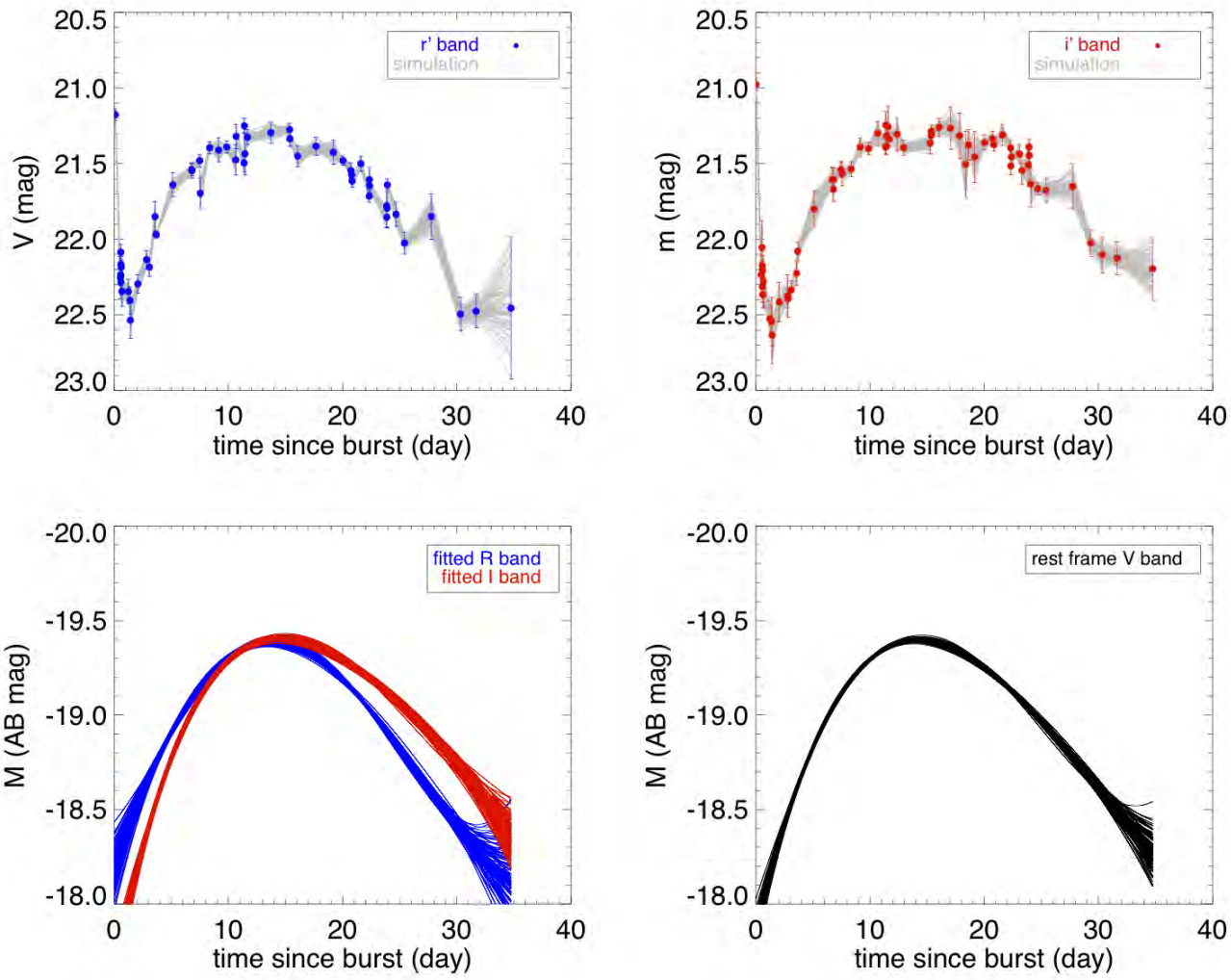

Figure 3.8: GRB 120422A/SN 2012bz. The line styles are the same as in Figure 3.3.

when the redshifted V band is between the two observed bands. 3) Some systems have very uncertain host extinction or host galaxy contribution. 4) Some systems lack enough data to do polynomial fits to obtain light curves. e.g., for 2nd order, at least 3 data points are required. In practice, to obtain well defined light curves, more data points are needed. Below we provide a brief discussion for each system. The reasons for these systems being excluded from our analysis are summarized in Table 3.3.

Table 3.3: A list of unselected systems in class A, B, and C.

GRB/XRF/SN	reason(s)
970228	4
990712	1, 4
011121/2001ke	3, 4
020405	1, 4
020903	1
021211/2002lt	1
040924	4
041106	2
080319B	1
081007/2008hw	3
091127/2009nz	1
101219B/2012ma	4
120714B/2012eb	4

1: After subtracting the afterglow, there are too few data points left to obtain full light curves.
2: Lack of data in proper band(s) to do K-correction.
3: Uncertain host extinction or host galaxy contribution.
4: Lack of sufficient data around the peak to do polynomial fitting.

GRB 970228 At $z = 0.695 \pm 0.002$ (Galama et al., 2000) I band data are collected. However, there are not enough data (< 3) around the peak in the I band.

GRB 990712 The V and I bands (Björnsson et al., 2001; Christensen et al., 2004; Sahu et al., 2000) have less than 3 data points after subtracting the afterglow brightness. In the R band, there are not enough data points to perform polynomial fitting.

GRB 011121/SN 2001ke At $z = 0.36$ (Bloom et al., 2002) R and I band data (Bloom et al., 2002; Garnavich et al., 2003; Greiner et al., 2003; Küpcü Yoldaş et al., 2007) are collected. The host and the afterglow brightness are subtracted. Then there are not enough data around peak to do polynomial fitting in the I band. In addition, the host extinction is very uncertain.

GRB 020405 After subtracting the host and afterglow flux, there are too few data points left (< 3) (Masetti et al., 2003; Price et al., 2003) to obtain light curves.

XRF 020903 After subtracting the afterglow brightness, there are not enough useful data points to do the polynomial fitting (Bersier et al., 2006; Soderberg et al., 2005).

GRB 021211/SN 2002lt After subtracting the host and afterglow flux, there are too few data points left (< 3) (Della Valle et al., 2003) to obtain light curves.

GRB 040924 The redshift is $z = 0.86$. But only in I band, there are enough data (Soderberg et al., 2006; Wiersema et al., 2008). After subtracting the afterglow brightness, there are not enough useful data to fit polynomial functions.

GRB 041006 Only in the R band there are enough data (Stanek et al., 2005) to extract the light curve. But at a redshift of $z = 0.716$, the R band is too far from the rest frame V band.

GRB 080319B The redshift is $z = 0.937$ and the data (Bloom et al., 2009; Tanvir et al., 2010) are in the R and I bands. The host contributions are $R_{\rm host} = 26.96 \pm 0.13$ mag and $I_{\rm host} = 26.17 \pm 0.15$ mag. The afterglow slope is fixed to $\beta_2 = 2.33$ (Bloom et al., 2009; Tanvir et al., 2010). After subtracting the afterglow brightness there are not enough useful data points left to fit polynomial functions.

GRB 081007/SN 2008hw The redshift is $z = 0.5295$ and the data are in the r′ and i′ bands (Jin et al., 2013). For the afterglow fitting, we fixed the slope to $\beta_2 = 1.25$, based on the X-ray observation (Jin et al., 2013). A multi-band K-correction is applied. But the host contribution is uncertain. If we assume it has host $r_{\rm host} = 25.0$ mag and $i_{\rm host} = 24.5$ mag, then the peak magnitude is $M_{\rm V,peak} = -18.85^{+0.91}_{-0.64}$ mag. However, a different estimate of the host galaxy brightness would lead to different peak magnitudes.

GRB 091127/2009nz The redshift is $z = 0.49$ and the data are collected from Cobb et al. (2010); Troja et al. (2012); Vergani et al. (2011). The i band data are selected. We subtract the host brightness with $I_{\rm host} = 22.54 \pm 0.10$ mag (Troja et al., 2012). The afterglow is fitted with broken power-law functions. But after the afterglow fitting, there are not enough data to obtain light curves and measure the peak magnitude and the decline rate.

GRB 101219B/SN 2010ma With only two data points and an upper limit (Sparre et al., 2011), it is not possible to obtain the light curve.

GRB 120714B/SN 2012eb SN 2012eb was confirmed to be associated with GRB 120714B by Klose et al. (2012). But there are no published data for SN 2012eb yet.

3.4 PROPERTIES OF THE LIGHT CURVES

The peak magnitudes, the decline rate in 15 days, the time of peak (see section 3.4.2) of the eight GRB-SNe are listed in Table 3.4. For SNe Ia, there is a relation between the

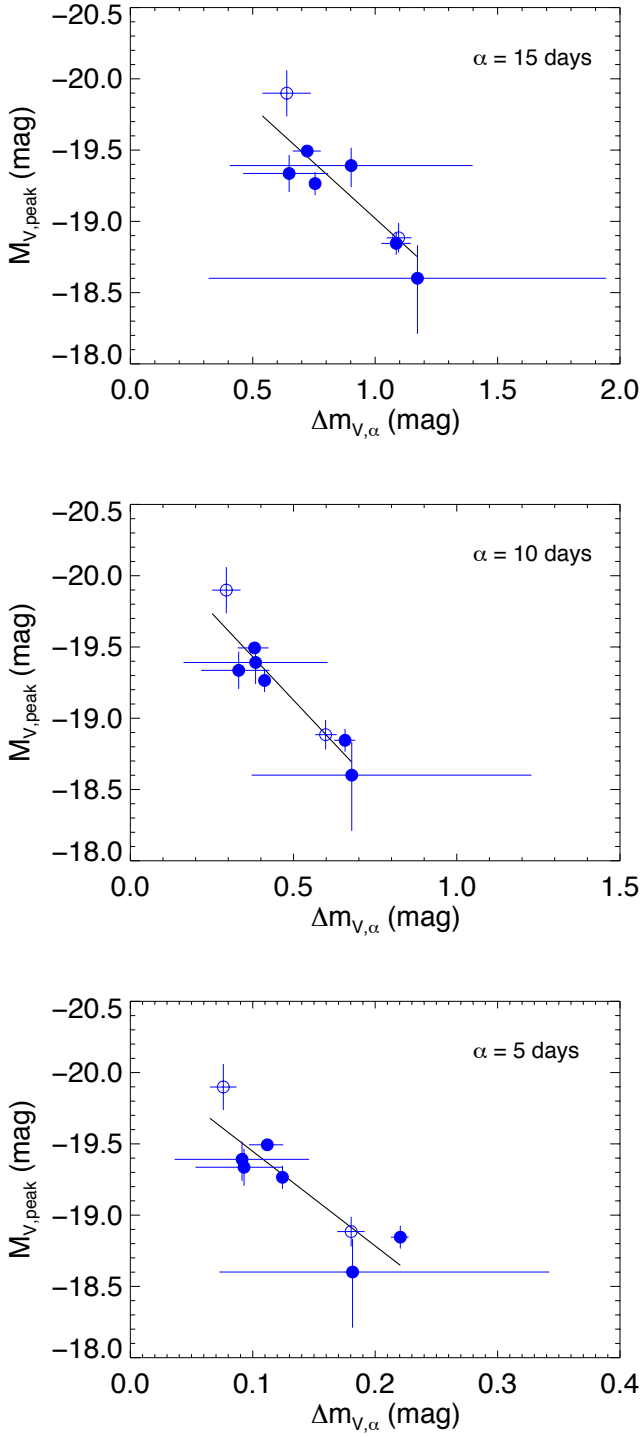

Figure 3.9: The peak-luminosity and decline rate relation for GRB-SNe with the decline times of 5, 10 and 15 days. Systems GRB 031203/SN 2003lw and GRB 100316D/SN 2010bh have uncertain extinction, and they are plotted as open symbols. The best linear fits to the relations are in black.

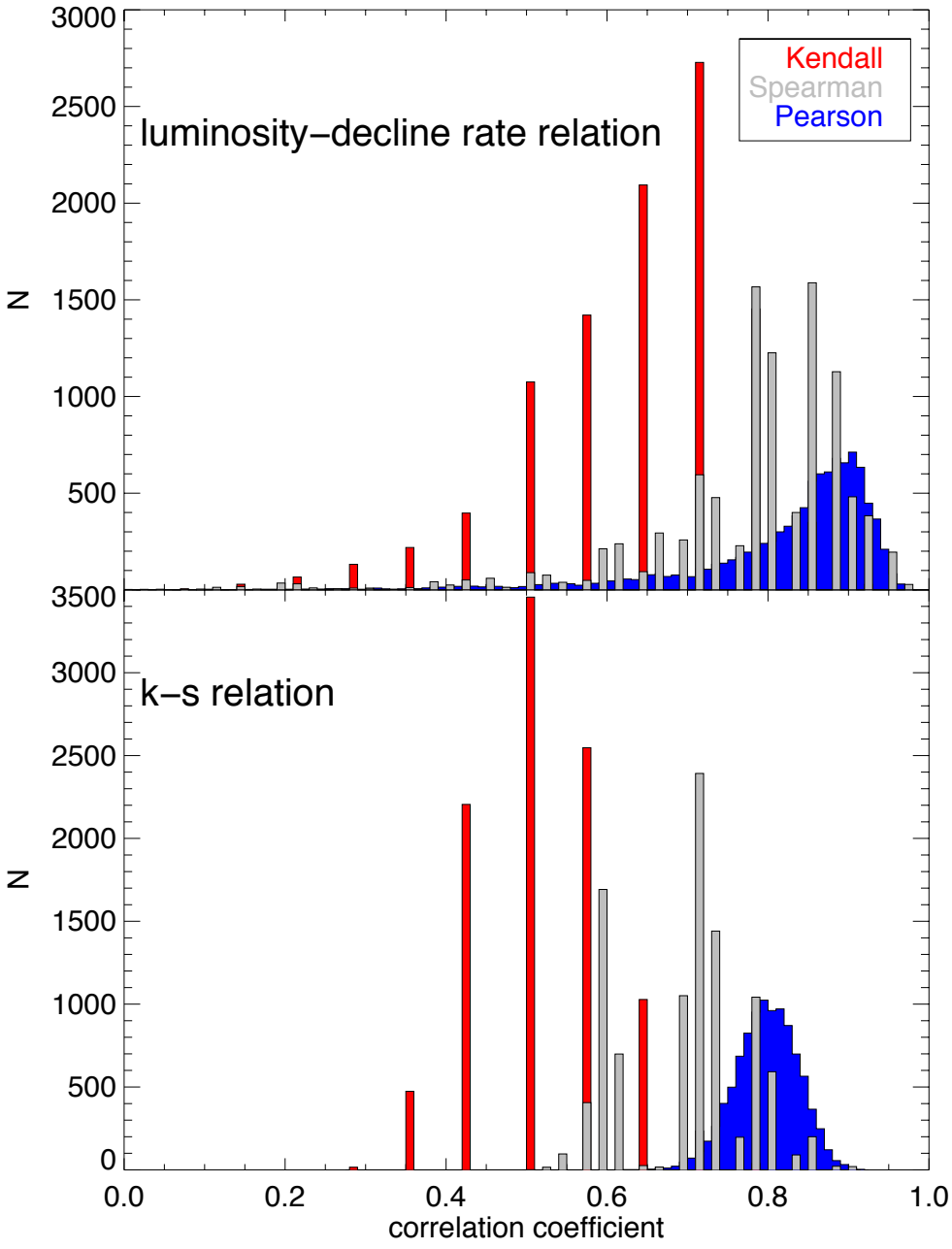

Figure 3.10: Kendal's τ, Spearman's rank, and Pearson's correlation coefficients of the luminosity-decline rate relation in the upper panel and the $k - s$ relation (section 3.4.2) in the bottom panel. Bin size is 0.01. $M_{\mathrm{V,peak}}$, $\Delta m_{\mathrm{V},15}$, the k factor and the s factor are resimulated 10 000 times with the standard Monte Carlo method.

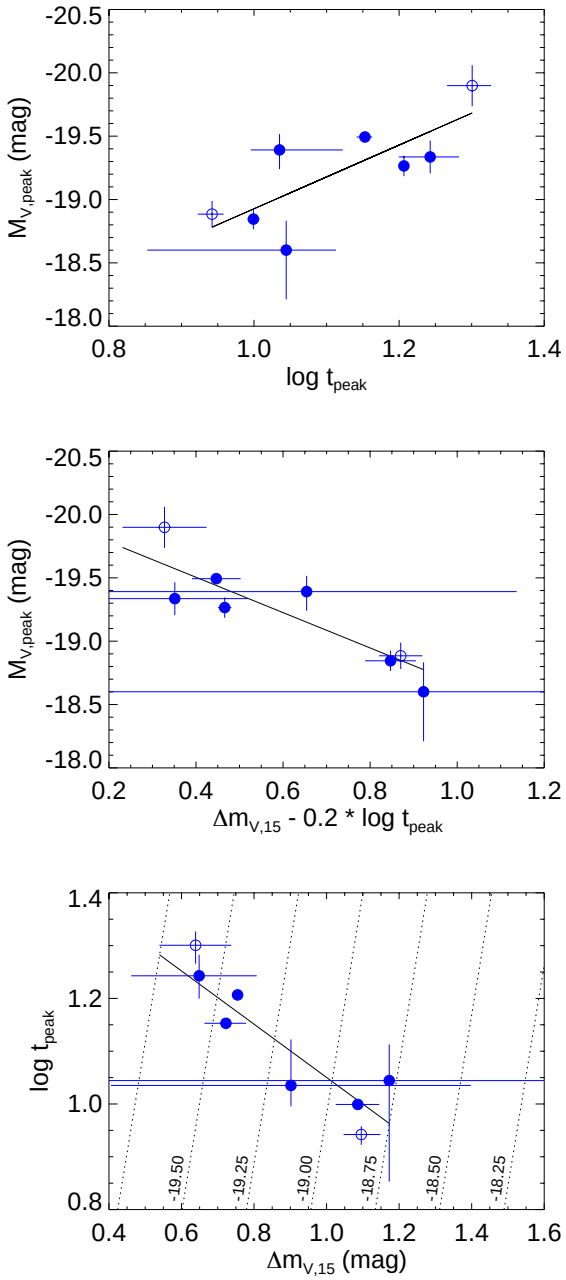

Figure 3.11: The relations between logarithmic peak time $\log t_{\rm peak}$, peak magnitude $M_{\rm V,peak}$ and decline rate $\Delta m_{\rm V,15}$. The upper panel shows $\log t_{\rm peak}$ as a function of $M_{\rm V,peak}$. The middle panel shows the multiple linear relation between $\Delta m_{\rm V,15}$, $\log t_{\rm peak}$ and $M_{\rm V,peak}$. The bottom panel displays a 'fundamental plane' like relation for GRB-SNe through $t_{\rm peak}$ and $\Delta m_{\rm V,15}$. The straight lines in blue are the best linear fitting functions (Eqs. 3.9, 3.11 and 3.10). The dotted lines indicate loci of equal absolute peak magnitudes. The best linear fits are plotted in black.

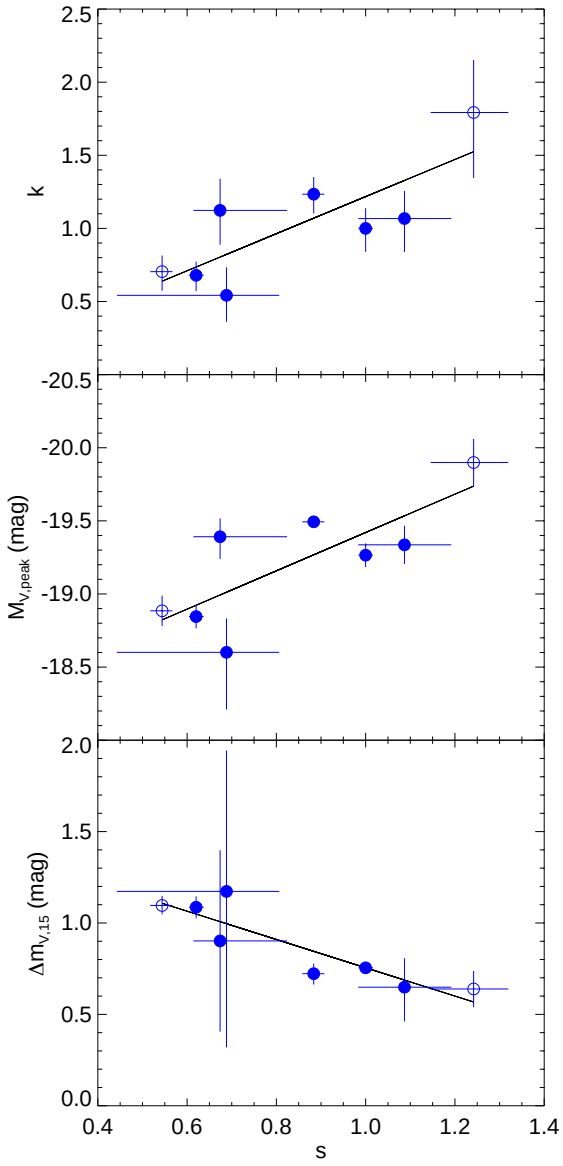

Figure 3.12: The relations between the s factor, the k factor, the decline rate $\Delta m_{\mathrm{V},15}$ and the peak magnitude $M_{\mathrm{V,peak}}$. The best linear fits are plotted in black.

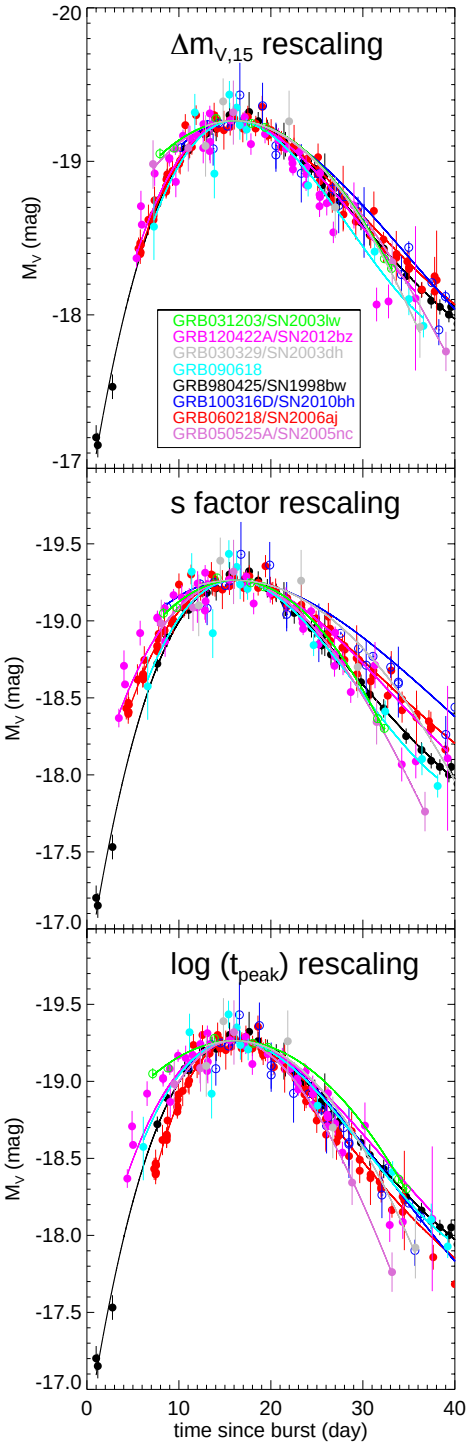

Figure 3.13: Different rescaling results of the the light curves of the selected systems in rest frame V band. Here $M_{\mathrm{V,peak}}$ has been normalized to that of SN 1998bw.

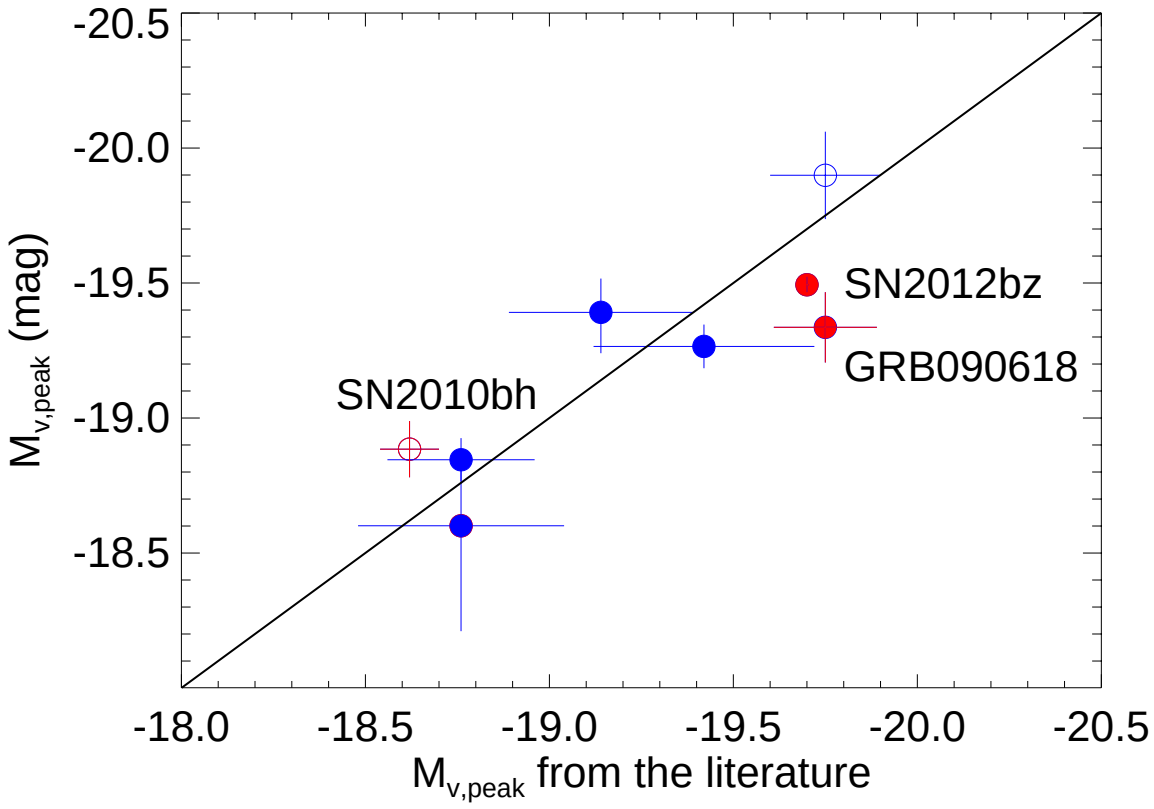

Figure 3.14: Comparison of the peak magnitudes determined in this paper (*y-axis*) and the values from Cano (2013); Cano et al. (2011a,b); Malesani et al. (2004); Schulze et al. (2014) (*x-axis*). The illustrative straight line in black is: $y = x$. There are three outliers GRB 090618, XRF 100316D/SN 2010bh and GRB 120422A/SN 2012bz (marked in red).

Table 3.4: The selected systems and relevant results with 1σ uncertainties.

GRB/XRF/SN	z	$M^{a}_{\rm V,peak}$ (mag)	$\Delta m_{\rm V,15}$ (mag)	$t_{\rm peak}$ (day)
980425/1998bw	0.00857	$-19.27^{+0.08}_{-0.08}$	$0.75^{+0.02}_{-0.02}$	$16.09^{+0.17}_{-0.18}$
030329/2003dh	0.1685	$-19.39^{+0.15}_{-0.12}$	$0.90^{+0.50}_{-0.50}$	$10.74^{+2.57}_{-0.85}$
031203/2003lw	0.1055	$-19.90^{+0.16}_{-0.16}$	$0.64^{+0.10}_{-0.10}$	$19.94^{+1.37}_{-1.48}$
050525A/2005nc	0.606	$-18.59^{+0.39}_{-0.23}$	$1.17^{+0.77}_{-0.85}$	$11.08^{+2.26}_{-3.37}$
060218/2006aj	0.03342	$-18.85^{+0.08}_{-0.08}$	$1.08^{+0.06}_{-0.06}$	$9.96^{+0.18}_{-0.18}$
090618	0.54	$-19.34^{+0.13}_{-0.13}$	$0.65^{+0.16}_{-0.19}$	$17.54^{+1.51}_{-1.64}$
100316D/2010bh	0.059	$-18.89^{+0.10}_{-0.10}$	$1.10^{+0.05}_{-0.05}$	$8.76^{+0.31}_{-0.37}$
120422A/2012bz	0.283	$-19.50^{+0.03}_{-0.03}$	$0.73^{+0.06}_{-0.06}$	$14.20^{+0.34}_{-0.34}$

a: The uncertainties in $M_{\rm V,peak}$ quadratically come from the polynomial fits, the 0.02 mag in K-correction, the distance modulus uncertainties and the uncertainties in the host extinction.

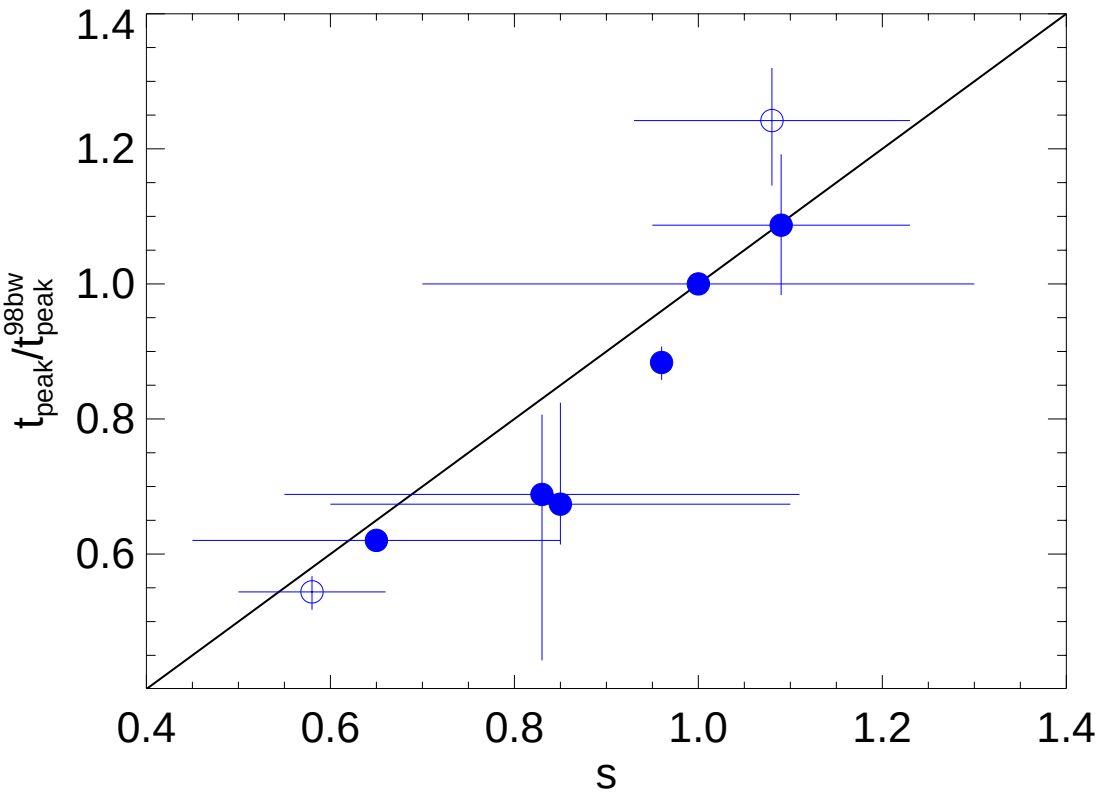

Figure 3.15: Comparison of peak time $t_{\rm peak}$ obtained in this paper (in Table 3.4) and the stretch factor s from Cano (2013). Here $t^{\rm 98bw}_{\rm peak} = 16.09^{+0.17}_{-0.18}$ days. The illustrative straight line in black is $y = x$.

intrinsic peak magnitude $M_{\rm V,peak}$ and decline rate $\Delta m_{\rm B,15}$ (Phillips, 1993; Phillips et al., 1999). In addition, $\Delta m_{\rm V,15}$ is used in this paper to check if the light curves of SN 1998bw can be used as light curve templates and if there is a better way to do the rescaling other than using the s factor.

3.4.1 LUMINOSITY-DECLINE RATE RELATION

$M_{\rm V,peak} = f(\Delta m_{\rm V,15})$

Though the physical progenitors and explosion mechanisms for SNe Ia and GRB-SNe are different (Smartt, 2009; **?**), their light curves show similar luminosity-decline rate relations. The peak magnitude and the decline rate are resimulated 10 000 times each. The widths of the distribution of the resimulated data are 1σ. We linearly fit each set of the resimulated data and get two distributions of the fitting parameters. The median values and $\pm1\sigma$ values on two sides of the median values in these two distributions are treated as the best fitting parameters and the $\pm1\sigma$ uncertainties. The luminosity-decline rate relation for GRB-SNe is

$$M_{\rm V,peak} = 1.57^{+0.25}_{-0.28}\Delta m_{\rm V,15} - 20.58^{+0.22}_{-0.20}, \tag{3.8}$$

with $\chi^2 = 5.51$ (6 dof). Figure 3.9 shows the luminosity-decline rate relation with $\alpha =$ 5, 10, and 15 days. Systems GRB 031203/SN 2003lw and GRB 100316D/SN 2010bh have uncertain extinction, so they are plotted as open symbols. Unless mentioned otherwise, these two systems are discerned in the same way in the following figures. Some systems lack data to constrain light curves at large times, i.e., $\alpha > 15$ days, so we cannot get $\Delta m_{\rm V,>15}$ for these systems. This relation shows that (1) the peak magnitudes span a small range; (2) the trend of the relation is the same as for SNe Ia, i.e., brighter systems decline slower. Though there could be significant selection effects, in that we only have good data for bright systems.

Correlation coefficients and significance

With the standard Monte Carlo method, the correlation coefficients: Pearson's, Kendal's τ and Spearman's rank, are calculated to statistically measure the strength of the correlation between the peak magnitudes and the decline rates. As in section 3.4.1, the peak magnitude $M_{\rm V,peak}$ and the decline rate $\Delta m_{\rm V,15}$ are resimulated 10 000 times each, where 1σ are the widths of the distribution of the resimulated data. For each set of resimulated data, we calculate three correlation coefficients.

Pearson's correlation coefficient (Pearson's r) measures the linear correlation between two variables. The result $r \in [-1, 1]$, where 1 (-1) is total positive (negative) correlation, and 0 is no correlation. When $|r| > 0.7$ (or 0.8 by different suggestion), the correlation is described as 'very strong'. If bin size is set to 0.01 (same in the following), $r = 0.905$ has the highest frequency and this shows the correlation is significant at 0.01 level. This means we expect to get the result occurring by chance once every 100 times. The result

indicates a significant correlation between $M_{\rm V,peak}$ and $\Delta m_{\rm V,15}$. There are [93%, 87%, 63%, 9%] of Pearson's correlation coefficients lie at [0.1, 0.05, 0.01, 0.001] significance levels.

Kendal's rank correlation coefficient (Kendal's τ) measures the strength of the monotonic relationship between variables. The result $\tau \in [-1, 1]$, where $1/-1$ imply the perfect agreement/disagreement between two rankings and 0 means the ranking is totally independent. In this paper, $\tau = 0.715$ has the highest frequency and the corresponding significance level is 0.01. There are [92%, 81%, 46%, 0.4%] of Kendal's rank correlation coefficients lie at [0.1, 0.05, 0.01, 0.001] significance levels.

Spearman's rank correlation coefficient (Spearman's ρ) tests the dependence between two variables. The result $\rho \in [-1, 1]$, where -1 or $+1$ appears when the relation of the variables can be perfectly described with a monotonic function. When $|\rho| \geq 0.6$, the correlation is described as 'strong'. In this paper, $\rho = 0.855$ has the highest frequency and the corresponding significance level is 0.025. There are [95%, 89%, 42%, 2%] of Spearman's rank correlation coefficients lie at [0.1, 0.05, 0.01, 0.001] significance levels.

Table 3.5: The most frequent values and the percentage of the correlation coefficients at different significance levels. Here we set the bin size equal to 0.01.

coefficient	significance level[a]				most frequent value
	0.1	0.05	0.01	0.001	
luminosity-decline rate relation					
Pearson's	93%	87%	63%	9%	0.905
Kendal's τ	92%	81%	46%	0.4%	0.715
Spearman's rank	95%	89%	42%	2%	0.855
$k - s$ relation					
Pearson's	100%	99%	18%	$\sim 0\%$	0.795
Kendal's τ	73%	38%	2.7%	$\sim 0\%$	0.505
Spearman's rank	100%	71%	3%	$\sim 0\%$	0.714

[a]: The probability of accidentally getting the result, e.g., 0.05 represents the result happens by chance once every 20 times.

The distributions of the correlation coefficients of the luminosity-decline rate relation are plotted in the upper panel in Figure 3.10. The most frequencies and the percentage of the correlation coefficients at different significance levels are listed in Table 3.5. The statistical correlation coefficients show that the luminosity and the decline rate of GRB-SNe are significantly correlated.

3.4.2 TIME SINCE BURST

Peak time

The peak time $t_{\rm peak}$ is defined as the time when the light curve of a GRB-SN reaches its peak brightness relative to the time of the GRB in the rest frame. The peak times for the eight systems are listed in Table 3.4. With the same procedure as in section 3.4.1, the best fit to the relation between $\log t_{\rm peak}$ and $M_{\rm V,peak}$ is

$$M_{\rm V,peak} = -2.52^{+0.15}_{-0.16} \log t_{\rm peak} - 16.40^{+0.18}_{-0.17}. \tag{3.9}$$

When combining the two parameters $\log t_{\rm peak}$ and $\Delta m_{\rm V,15}$, regression fit to $M_{\rm V,peak}$ can be expressed as

$$M_{\rm V,peak} = 1.41^{+0.72}_{-0.87} \Delta m_{\rm V,15} - 0.34^{+1.01}_{-1.43} \log t_{\rm peak} - 20.08^{+2.37}_{-1.73}. \tag{3.10}$$

The relation between $\log t_{\rm peak}$ and $\Delta m_{\rm V,15}$ can be expressed as

$$\log t_{\rm peak} = -0.50^{+0.13}_{-0.11} \Delta m_{\rm V,15} + 1.55^{+0.09}_{-0.10}. \tag{3.11}$$

Figure 3.11 shows the relations between $\log t_{\rm peak}$, $\Delta m_{\rm V,15}$ and $M_{\rm V,peak}$. The upper panel shows that there is a dependency between the peak time $t_{\rm peak}$ and the peak magnitude $M_{\rm V,peak}$. There is a trend that a GRB-SN with smaller peak time has fainter peak luminosity, i.e., $M_{\rm V,peak}$ decreases as $t_{\rm peak}$ increases. In general, brighter GRB-SNe evolve more slowly. Compared to Figure 3.9, $t_{\rm peak}$ is less strongly correlated with $M_{\rm V,peak}$ than $\Delta m_{\rm V,15}$. The middle panel shows a multiple linear regression fit to $M_{\rm V,peak}$ with $\log t_{\rm peak}$ and $\Delta m_{\rm V,15}$. The bottom panel of Figure 3.11 shows a 'fundamental plane' of GRB-SNe with peak time $t_{\rm peak}$ and decline rate $\Delta m_{\rm V,15}$. Constant absolute peak magnitudes are also indicated by dotted lines.

$k - s$ relation

Besides the peak magnitude $M_{\rm V,peak}$ and the decline rate $\Delta m_{\rm V,\alpha}$, another way to describe the light curve is through the luminosity factor k and the stretch factor s. These two factors stand for the relative peak (k) and width (s) of the light curves compared to SN 1998bw (Cano et al., 2011b):

$$f(t) = k \times f^{\rm 98bw}(t/s), \tag{3.12}$$

Here $f(t)$ is the flux of a SN, and $f^{\rm 98bw}(t)$ is the flux of SN 1998bw. The factor s equals to $t_{\rm peak}/t^{\rm 98bw}_{\rm peak}$, with $t^{\rm 98bw}_{\rm peak}$ representing the peak time of SN 1998bw. With the same procedure as in section 3.4.1, the s and k factors are correlated as

$$k = 1.27^{+0.12}_{-0.13} \cdot s - 0.05^{+0.10}_{-0.10}, \tag{3.13}$$

with $\chi^2 = 8.2$ (6 dof). This relation is named as $k - s$ relation. Figure 3.12 shows the correlations between s, k, the decline rate $\Delta m_{\rm V,15}$ and the peak magnitude $M_{\rm V,peak}$.

With the procedure discussed in section 3.4.1, the distributions of the correlation coefficients of the $k - s$ relation are plotted in the lower panel in Figure 3.10. The most frequencies and the percentage of the correlation coefficients at different significance levels are listed in Table 3.5. Comparing the results in Figures 3.9, 3.11, 3.12 and Table 3.5, we conclude that 1) the correlation between $\Delta m_{\mathrm{V},15}$ and $M_{\mathrm{V,peak}}$ is stronger than the one between factors k and s. 2) $\Delta m_{\mathrm{V},15}$ is stronger correlated with $M_{\mathrm{V,peak}}$ than t_{peak} and the s factor.

3.4.3 RESCALING OF LIGHT CURVES

We rescale the time axes of the light curves in three ways. $M_{\mathrm{V,peak}}$ has been normalized relative to SN 1998bw.

Δm_{15} rescaling The light curves are stretched around t_{peak}, when the light curves reach the peak brightness. The time of the light curve is calculated as $t' = (t - t_{\mathrm{peak}}) \times \Delta m_{\mathrm{V},15}/\Delta m_{15}^{\mathrm{98bw}} + t_{\mathrm{peak}}^{\mathrm{98bw}}$, with $\Delta m_{15}^{\mathrm{98bw}}$ and $t_{\mathrm{peak}}^{\mathrm{98bw}}$ representing the decline rate and the peak time of SN 1998bw, i.e., a faster decline light curve with bigger $\Delta m_{\mathrm{V},15}$ will be rescaled to be more flat.

s factor rescaling The light curves are stretched since the burst as $t' = t/s$, with s being the stretch factor. The factor s is another way representing the decline rate of the light curves, similar to $\Delta m_{\mathrm{V},15}$. A faster decline light curve with smaller s will be more flatter after the stretch.

$\log(t_{\mathrm{peak}})$ rescaling The light curves are stretched around t_{peak}. The time is calculated as $t' = (t - t_{\mathrm{peak}}) \times \log(t_{\mathrm{peak}}^{\mathrm{98bw}})/\log(t_{\mathrm{peak}}) + t_{\mathrm{peak}}^{\mathrm{98bw}}$. This method is similar to Δm_{15} rescaling, both stretch the light curves around the peak brightness. But in this method, a parameter $\log(t_{\mathrm{peak}})$ is used instead of $\Delta m_{\mathrm{V},15}$.

A collection of rescaled light curves for the selected systems are shown in Figure 3.13. The fitting curves are the rest frame V band light curves obtained in section 3.3. The data points are for illustration and are from the bands closest to the rest frame V band. The figure shows that a rescaled SN 1998bw light curve is a reasonable template for other GRB-SN light curve. Δm_{15} rescaling appears superior to the other approaches. If values of Δm_{15} are not available, $\log(t_{\mathrm{peak}})$ rescaling is an alternative to the commonly used s factor rescaling.

3.4.4 DISCUSSION

We compare the values of the peak magnitudes to other studies (Cano, 2013; Cano et al., 2011a,b; Malesani et al., 2004; Schulze et al., 2014). The result is shown in Figure 3.14. There are three obvious outliers: GRB 090618, SN 2010bh and SN 2012bz (marked in red). These systems are estimated to have fainter peak magnitudes in this paper. It is difficult to trace the exact causes of the differences in the peak magnitudes. We follow the procedure from the literature, and compare it to our results.

There is no independent third-part study for the peak magnitude of GRB 090618. The peak magnitude is estimated to be $M_{\rm V,peak} = -19.34^{+0.13}_{-0.13}\,(-19.75^{+0.14}_{-0.14})$ mag from this paper (Cano et al., 2011a). The reasons cause the difference are: 1) With different cosmological parameters, the distance modulus is different. We adopt distance modulus $\mu = 42.53$ with the cosmological parameters $\{\Omega_M, \Omega_\Lambda, h\}$ = {0.315, 0.685, 0.673}, while $\mu = 42.45$ from Cano et al. (2011a). 2) The subtraction of the afterglow may be another reason for the discrepancy. This may cause ~ 0.15 mag difference around the peak. The observed peak magnitude is $i = 22.33$ mag. After the host and the afterglow subtraction with $i_{\rm host} = 23.22 \pm 0.06$ mag, the peak magnitude becomes $i = 22.96$ mag and $i = 23.13$ mag, respectively. From Cano et al. (2011a) the apparent peak magnitude is $i = 23.00$ mag. 3) The polynomial fitting may bring ~ 0.08 mag difference. The fitted (observed) apparent peak magnitude is $i = 23.21$ (23.13) mag. Figure 3.5 shows the observed data. Around peak, the data are noisy. At $t = 16.69$ and 17.60 days, the magnitudes are ~ 0.2 and 0.04 mag fainter than the one at $t = 14.79$. Instead of using a single datum, in this paper, polynomial functions are fitted, especially around the peak. 4) The Galactic extinction is different. In this paper, we use $R_V = 3.1$ as well as the re-calibration results of DIRBE/IRAS dust map from Schlafly & Finkbeiner (2011). This may bring ~ 0.15 mag difference.

For XRF 100316D/SN 2010bh, the peak magnitude is constrained to be $M_{\rm V,peak} = -18.89^{+0.10}_{-0.10}/-18.62 \pm 0.08$ mag in this paper/Cano et al. (2011b). This is a system with uncertain host extinction and peak magnitude. The reasons are: 1) The values in Cano et al. (2011b) are inconsistent. In Table 2 (Cano et al., 2011b), the apparent peak magnitude in the V band is 19.47 mag after the Galactic extinction correction. So if $R_V = 3.1$ and K-correction $\Delta k = 0.09$ are used in his calculation, the peak magnitude should be $M_{\rm V,peak} = m_V - \mu - A_{\rm V,host} - \Delta K = 19.47 - 37.08 - 0.18 \cdot 3.1 - 0.09 = -18.26$ mag instead of -19.62 mag, which is listed In Table 4 (Cano et al., 2011b). The photometric data from Cano et al. (2011b) is consistent with the result from Bufano et al. (2012), so we guess the foreground extinction is subtracted twice in the calculation, which is consistent with the statement of the captions of Table 2 and 4. The result also shows that a larger host extinction is expected, otherwise the spectrum is very red (as stated in section 3.3.7). 2) The host extinction estimated in the literature are different. We adopt a large extinction with $E(B-V)_{\rm host} = 0.39 \pm 0.03$ mag from Olivares E. et al. (2012). The value of $E(B-V)_{\rm host} = 0.18 \pm 0.08$ mag is estimated in Cano et al. (2011b). This may cause ~ 0.64 mag difference. 3) The distance moduli are different. In this paper, $\mu = 37.20$ while Cano et al. (2011b) adopts $\mu = 37.08$. This causes about 0.12 mag difference. 4) The K-correction in (Cano et al., 2011b) may bring about 0.09 mag difference.

For GRB 120422A/SN 2012bz, the peak magnitude is estimated to be $M_{\rm V,peak} = -19.50^{+0.03}_{-0.03}/-19.7$ mag in this paper/Schulze et al. (2014), while using the same cosmological parameters (Planck Collaboration et al., 2013), Leloudas (2014) estimates the peak magnitude to be -19.63 mag. The reasons of the discrepancies may be as follows: 1) The Galactic extinction may be corrected twice in calculating the absolute peak mag-

nitude (Leloudas, 2014; Schulze et al., 2014). So the magnitude should be about 0.09 mag fainter. 2) In addition, R_V instead of R_I may be multiplied in calculating the Galactic extinction. This may in further bring about ~ 0.05 mag difference. 3) As discussed above, the noisy data around the peak may bring about 0.03 mag difference.

Figure 3.15 shows the comparison of peak time in this paper (in Table 3.4) and the stretch factor s from Cano (2013). There is no information on s_V for systems SN 2003dh, SN 2003lw, GRB 050525A and GRB 090618, so s_R is used instead.

3.5 CONCLUSIONS

We developed a method for obtaining the light curves in the rest frame V band from the observational data. A standard Monte Carlo method was used for error estimation. Afterglow and host brightness were subtracted. We used the DIRBE/IRAS dust map and the correction coefficients to correct the foreground extinction. The host extinction was corrected. We used a multi-band K-correction to correct the light curves from the observed bands into the rest frame V band. Alternatively, SN 1998bw peak SED and decline rate templates were used when a multi-band K-correction is not feasible. Polynomial functions were fitted to obtain the light curves.

Based on this method we obtained the peak magnitudes and the decline rates for eight GRB-SN systems in classes A, B, and C. We discovered a relation between the peak magnitude and the decline rate. This luminosity-decline rate relation was tested with the decline day α at 5, 10 and 15 days. The strength of the relationship between the peak magnitude and the decline rate was statistically measured by three correlation coefficients and the significance levels were discussed. There is a dependency between the peak magnitude and the peak time. The larger the peak time, the brighter the SN is. We found that the light curve of SN 1998bw can be used as a representative template. In addition, rescaling around the peak time with $\Delta m_{\mathrm{V},15}$ is better than rescaling with peak time $\log t_{\mathrm{peak}}$ or stretch factor s. We also compared the peak magnitudes and the decline rates constrained from this work to the results from other studies.

SNe Ia and GRB-SNe have completely different progenitors. Nevertheless, the light curves have similar peak magnitudes and decline rates. This phenomenon may potentially help us shed light on progenitor models of GRBs. As SNe Ia are widely used as standard candles to measure cosmological distances, it is possible that GRB-SNe may also turn out to be useful high-redshift standard candles. In Li et al. (2014), we study the cosmological constraints of Ω_m and Ω_Λ resulting from these 8 systems. In particular, the prospects of studying dark energy through $w(z)$ with GRB-SNe using the James Webb Space Telescope (JWST) is intriguing.

We thank Enrico Ramirez-Ruiz, Tamara Davis Giorgos Leloudas and Radek Wojtak for their many helpful discussions and comments on the paper. We thank Teddy Frederiksen, Darach Watson, Daniele Malesani and Dong Xu for discussions on GRB and SNe. The Dark Cosmology Centre is funded by the Danish National Research Foundation.

4

COSMOLOGICAL PARAMETERS WITH GRB-SNE

Knowing others
is wisdom,
knowing yourself
is Enlightenment
Lao Tzu

Abstract -
We report estimates of the cosmological parameters Ω_m and Ω_Λ obtained using supernovae (SNe) associated with gamma-ray bursts (GRBs) at redshifts up to 0.606. Eight high-fidelity GRB-SNe with well-sampled light curves across the peak are used. We correct their peak magnitudes for a luminosity-decline rate relation to turn them into accurate standard candles with dispersion $\sigma = 0.18$ mag. We also estimate the peculiar velocity of the low-redshift host galaxy of SN 1998bw, using constrained cosmological simulations. In a flat universe, the resulting Hubble diagram leads to best-fit cosmological parameters of $(\Omega_m, \Omega_\Lambda) = (0.58^{+0.22}_{-0.25}, 0.42^{+0.25}_{-0.22})$. This exploratory study suggests that GRB-SNe can potentially be used as standardizable candles to high redshifts to measure distances in the universe and constrain cosmological parameters.

4.1 INTRODUCTION

The accelerating expansion of the universe was detected with the help of Type Ia supernovae (SNe Ia) (Perlmutter et al., 1997, 1999; Riess et al., 1998). Taking advantage of the correlation between their decline rate and peak brightness (Phillips, 1993; Phillips et al., 1999), the corrected luminosities of SNe Ia exhibit sufficiently small dispersons that they can be used to measure cosmological distances and constrain cosmological parameters.

Submitted for publication as: Xue Li, Jens Hjorth, Radek Wojtak – *Cosmological parameters from supernovae associated with gamma-ray bursts*, Astrophysical Journal Letters.

While SNe Ia are exquisite standard candles that are routinely used to measure distances out to $z \approx 1.0$ (Hook, 2013; Koekemoer et al., 2011), the rate of events unfortunately appears to decline at higher redshifts (Graur et al., 2014; Rodney et al., 2014). However, it is necessary to observe the universe at redshift $z > 1$ to constrain the dark-energy equation of state parameter $w(z)$ by breaking the degeneracies between cosmological models (King et al., 2013; Linder & Huterer, 2003).

At higher redshifts, e.g., $z > 1.5$, core collapse supernovae (CCSNe) strongly dominate the rates of SNe (Li et al., 2012; Rodney et al., 2014). Moreover, with more powerful telescopes to be launched, e.g., the *James Webb Space Telescope* (*JWST*), CCSNe may be discovered at redshifts up to $z = 7 - 8$ (Pan & Loeb, 2013). But in general, CCSNe are much fainter than SNe Ia. They do not have the same intrinsic luminosities and their peak magnitudes do not exhibit any correlation with the decline rates (Drout et al., 2011).

This problem may be solved by considering a certain type of CCSNe: a subclass of broad-lined Type Ic SNe which are observed to be associated with gamma-ray bursts (GRBs). First observed by the Vela Satellites in 1967 (Klebesadel et al., 1973), GRBs are flashes of narrow beams of intense electromagnetic radiation whose peak energies occur at gamma-ray wavelengths (Metzger et al., 1997). SN 1998bw was first detected to be associated with GRB 980425 (Galama et al., 1998; Iwamoto et al., 1998; Kulkarni et al., 1998; Woosley et al., 1999). Since then, many GRB-SNe have been found (Hjorth & Bloom, 2012; Hjorth et al., 2003; Stanek et al., 2003; Woosley & Bloom, 2006).

GRB-SNe have relatively smooth optical spectra and very large explosion energies (Galama et al., 1998; Hjorth, 2013). The peak magnitudes of GRB-SNe are in the same range as SNe Ia. Moreover, their peak magnitudes are correlated with their decline rates (Li & Hjorth, 2014). While GRB-SNe are rare and difficult to disentangle from the contaminating light of the GRB afterglow and host galaxy, these properties could make GRB-SNe a powerful tool for distance determination and constraining cosmological parameters. This paper is devoted to the first quantitative exploration of this idea.

The outline of the paper is as follows. In Section 4.2, we briefly review the procedure of obtaining light curves of GRB-SNe, and measuring peak magnitudes and decline rates. We also present an estimate of the peculiar velocity of the host galaxy of the low-redshift SN 1998bw. In Section 4.3, we establish GRB-SNe as standard candles based on a limited set of high-quality GRB-SNe. In Section 4.4 we create a Hubble diagram and place constraints on the matter density parameter assuming a flat ΛCDM cosmological model. We conclude in Section 4.5.

4.2 GRB-SNE SYSTEMS

The selected GRB-SNe are firmly associated with GRBs from class *A* to class *C* (Hjorth & Bloom, 2012), where class *A* has 'strongest spectroscopic evidence'. Here we briefly summarize the discussion of the steps in obtaining the light curves of GRB-SNe. More details on the procedure are in Li & Hjorth (2014). The systems are listed in Table 4.1.

Table 4.1: Light curve properties of GRB-SNe systems

GRB/XRF/SN	z	$m_V^{\rm corr}$ [a] (mag)	$\Delta m_{V,15}$ [b] (mag)
980425/1998bw	0.00857 [c]	$13.66^{+0.08}_{-0.08}$	$0.75^{+0.02}_{-0.02}$
030329/2003dh	0.1685	$20.23^{+0.15}_{-0.12}$	$0.90^{+0.50}_{-0.50}$
031203/2003lw	0.1055	$18.62^{+0.16}_{-0.16}$	$0.64^{+0.10}_{-0.10}$
050525A/2005nc	0.606	$24.24^{+0.39}_{-0.23}$	$1.17^{+0.77}_{-0.85}$
060218/2006aj	0.03342	$17.07^{+0.08}_{-0.08}$	$1.09^{+0.06}_{-0.06}$
090618	0.54	$23.20^{+0.13}_{-0.13}$	$0.67^{+0.16}_{-0.19}$
100316D/2010bh	0.059	$18.31^{+0.10}_{-0.10}$	$1.10^{+0.05}_{-0.05}$
120422A/2012bz	0.283	$21.40^{+0.03}_{-0.03}$	$0.73^{+0.06}_{-0.06}$

[a]: Here $m_V^{\rm corr}$ is the apparent magnitude after extinction correction and K correction (Li & Hjorth, 2014).

[b]: Here $\Delta m_{V,15}$ represents the decline of the rest frame V-band magnitude 15 days after the SN reaches its peak brightness.

[c]: More details are in Section 4.2.2.

4.2.1 Data Analysis

The afterglow is either fitted to power-law or broken power-law functions and subtracted. Both Galactic and host extinction are corrected for. For the Galactic extinction, we assume $R_V = 3.1$ and get $E(B-V)$ from the DIRBE/IRAS dust map (Schlegel et al., 1998). The values are re-calibrated based on Table 6 in Schlafly & Finkbeiner (2011). We take the values of host extinction from the literature. We fit low-order polynomial functions to obtain the light curves. A K correction method is developed to correct the peak magnitudes and decline rates into the rest frame V band. A 'multi-band K-correction' is used for systems which have two band data available and these two bands are close to the redshifted V band. Otherwise, SN 1998bw peak SED and decline rate templates are used to correct the peak magnitude and the decline rate from the light curve obtained at a wavelength close to the redshifted V band. In total eight light curves of GRB-SNe with z up to 0.606 are obtained in the rest frame V band (Li & Hjorth, 2014).

4.2.2 Peculiar Velocity and Uncertainty of Distance Modulus of SN 1998bw

SN 1998bw (Galama et al., 1998; Iwamoto et al., 1998; Kulkarni et al., 1998; Woosley et al., 1999) was the first SN discovered to be connected with a GRB (GRB 980425). It is the nearest GRB-SN so far, and the measured redshift is $z = 0.00867 \pm 0.00004$ (Foley et al., 2006), so it constitutes an important low-redshift anchor of the Hubble diagram. For the recessional velocity of this low-redshift system, the contribution from the peculiar velocity may be relatively substantial. The true recessional velocity $v_{\rm rec}$ due to the Hubble

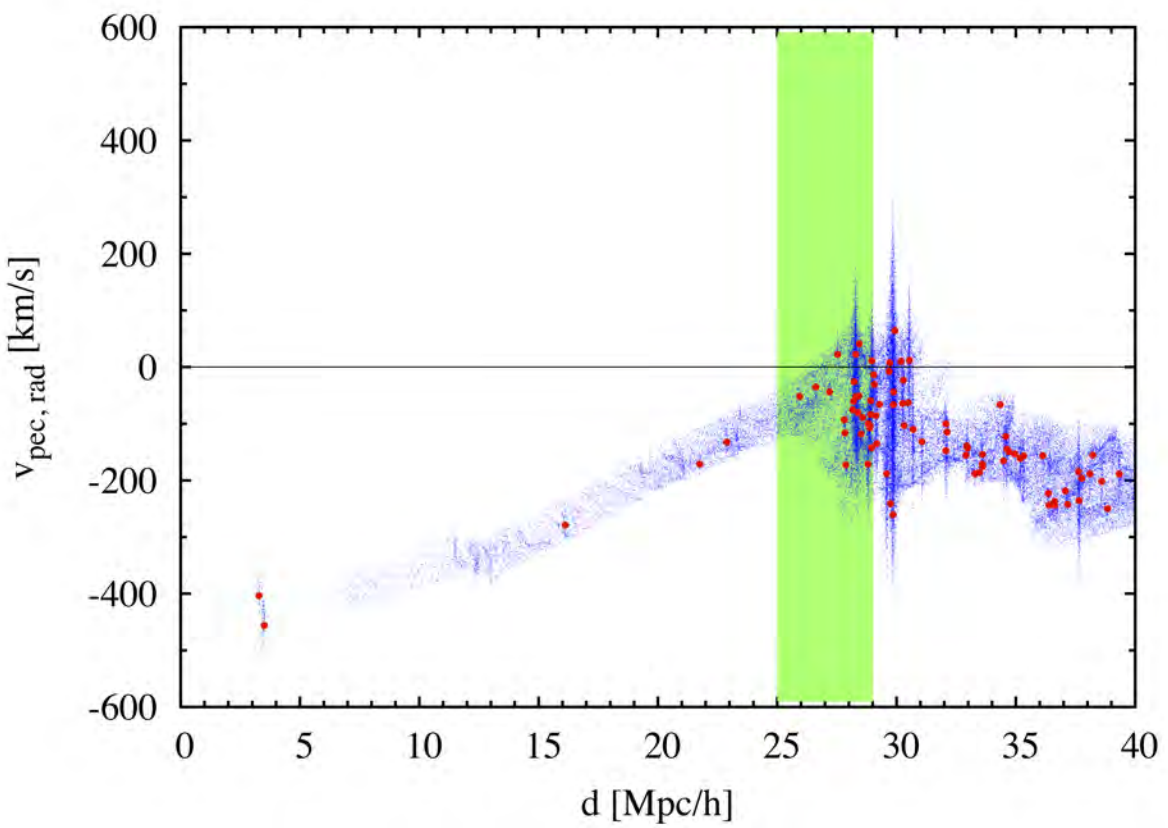

Figure 4.1: Peculiar velocities (line-of-sight component) in the direction of the supernova host galaxy, ESO 184−G82, as a function of the comoving distance from the Local Group formed the constrained simulation. The blue dots show dark matter particles and the red symbols represent dark matter haloes. The green band indicates the location of the galaxy ESO 184−G82.

flow should be corrected for the peculiar velocity $v_{\rm pec}$ of the host galaxy: $v_{\rm CMB} = v_{\rm rec} + v_{\rm pec}$, with $v_{\rm CMB}$ being the velocity relative to the cosmic microwave background (CMB).

In order to estimate the peculiar velocity of its host galaxy, ESO 184−G82, and calculate the uncertainty in the distance modulus, we use a dark matter simulation performed as a part of the Constrained Local Universe Simulations (CLUES) project. The simulation is carried out in a volume of $(160h^{-1}{\rm Mpc})^3$ containing 1024^3 particles. The assumed cosmological model is based on the 3rd data release of the WMAP satellite (WMAP3 cosmology), i.e., matter density $\Omega_m = 0.24$, dimensionless Hubble parameter $h = 0.73$, and normalization of the power spectrum $\sigma_8 = 0.76$. The initial conditions are generated from observational data of the galaxy distribution and galaxy velocities in the local universe (for technical details see Gottloeber et al., 2010). With this setup, the simulation recovers all observed structures on scales larger than $5h^{-1}{\rm Mpc}$. In particular, all nearby galaxy clusters and superclusters, such as the Virgo cluster, the Coma cluster, the Great Attractor and the Perseus–Pisces cluster, are well reproduced in the final simulation snapshot. On the other hand, small scale structures formed in the simulation emerge from a random realization of the power spectrum on these scales. Their evolution, however, is strongly constrained by nearby large-scale structures. Therefore, the simulation provides a realistic and dynamically self-consistent model for the matter distribution and the velocity field in the local universe.

The position vector of the host galaxy with respect to the Local Group in the simulation box can be found be matching angular separations from several large-scale structures. As the reference structures, we use the Coma cluster, the Perseus–Pisces cluster and the Great Attractor. Having determined the direction to the host galaxy from the Local Group in the simulation box, we compute the radial components of peculiar velocities within a narrow light cone. Figure 4.1 shows the resulting projected peculiar velocities as a function of the comoving distances from the Local Group. The blue dots show velocities of dark matter particles, whereas the red symbols represent dark matter haloes found with the friends-of-friends algorithm. Lack of dark matter haloes at small distances is related to the fact that the line of sight crosses the edge of the Local Void (see Nasonova & Karachentsev, 2011).

To identify the position of the host galaxy ESO 184−G82 in the simulation box, we use a range of plausible distances to the host galaxy in units of Mpc/h so they are independent of H_0. We assume that the true recessional velocity is likely between the host velocity with respect to the CMB $v_{\rm CMB} = 2505 \pm 14$ km s^{-1} (Foley et al., 2006) and the host velocity with respect to the local large-scale structures (Virgo, Great Attractor and Shapley Supercluster) $v_{\rm Virgo+GA+Shapley} = 2769 \pm 21$ km s^{-1}, as shown in the green band in Figure 4.1 . Within the green band, the mean peculiar velocity is $v_{\rm pec} = -65$ km s^{-1} with a mean systematic error ± 75 km s^{-1}. Combined with the peculiar velocity $v_{\rm pec}$ and the CMB velocity $v_{\rm CMB}$, the Hubble flow velocity is $v_{\rm rec} = 2570 \pm 76$ km s^{-1}, which is in the green band in Figure 4.1, as expected. The uncertainty of $v_{\rm pec}$ dominates the uncer-

more details are in http://ned.ipac.caltech.edu/ and the reference therein

tainty of $v_{\rm rec}$. The corresponding redshift is $z = v_{\rm rec}/c = 0.00857 \pm 0.00025$. Therefore, the contribution of the peculiar velocity of the the host galaxy to uncertainty in the distance modulus of SN 1998bw is $\sigma(\rm DM) = (5/2.3)\sigma(v_{\rm pec})(cz)^{-1} = 0.06$ mag, where c is the speed of light and $\sigma(v_{\rm pec})$ is the uncertainty of peculiar velocity $v_{\rm pec}$.

4.3 GRB-SNE AS STANDARD CANDLES

In much the same way as SNe Ia were used to measure the cosmological parameters Ω_m and Ω_Λ (Perlmutter et al., 1997, 1999; Riess et al., 1998), here we use GRB-SNe as standard candles.

Similar to SNe Ia (Phillips, 1993; Phillips et al., 1999), GRB-SNe have bright peak luminosities. The luminosity-decline rate relation for GRB-SNe in the rest-frame V band is (Li & Hjorth, 2014)

$$M_{\rm V,peak} = \alpha \Delta m_{V,15} + M_0, \tag{4.1}$$

where α is the slope and M_0 is a constant representing the absolute peak magnitude at $\Delta m_{V,15} = 0$. Assuming $\Omega_m = 0.315$ and $H_0 = 67.3$ km s^{-1} Mpc^{-1} (Planck Collaboration et al., 2013), we have $\alpha = 1.57^{+0.25}_{-0.28}$ and $M_0 = -20.58^{+0.22}_{-0.20}$ (Li & Hjorth, 2014). This relation is superior to other similar relations (Li & Hjorth, 2014), such as the $k-s$ relation (Cano, 2014), where k and s are the relative peak and width of the light curves compared to SN 1998bw, or the relation between the peak magnitude and the elapsed time since GRB. With $M_{\rm V,peak}$ from Li & Hjorth (2014), obtained using the above Planck cosmology, the corrected apparent peak magnitude in the rest-frame V band is

$$m_V^{\rm corr} = M_{\rm V,peak} + DM(z), \tag{4.2}$$

where $m_V^{\rm corr}$ is the corrected apparent magnitude in the rest-frame V band after corrections for dust extinction and K correction (Li & Hjorth, 2014). Here $DM(z)$ is the distance modulus at $\Omega_m = 0.315$ and $H_0 = 67.3$ km s^{-1} Mpc^{-1} in a flat universe. The values of $m_V^{\rm corr}$ are listed in Table 4.1. Considering the relation in Eq. (4.1), the effective apparent peak magnitude $m_V^{\rm eff}$ can be obtained as

$$m_V^{\rm eff} = m_V^{\rm corr} - \alpha \Delta m_{V,15}. \tag{4.3}$$

The term $\alpha \Delta m_{V,15}$ represents the correction due to the luminosity-decline rate relation. The effective apparent magnitude can also be expressed as (Perlmutter et al., 1997, 1999)

$$m_V^{\rm eff} = \Upsilon + 5 \log \mathcal{D}_L(z; \Omega_m, \Omega_\Lambda), \tag{4.4}$$

where $\mathcal{D}_L \equiv H_0 d_L$ is the "H_0-free" luminosity distance in units of km s^{-1}, with d_L being the luminosity distance in units of Mpc (Hogg, 1999) and H_0 in units of km s^{-1} Mpc^{-1}. Here $\Upsilon = M_0 - 5 \log H_0 + 25$ is the "H_0-free" V-band absolute peak magnitude (Perlmutter et al., 1997, 1999). The fitting procedure does not invoke H_0 and the constraints on cosmological parameters are therefore independent of the Hubble constant. In this paper, α and Υ are statistical 'nuisance' parameters.

4.4 CONSTRAINTS ON Ω_m AND Ω_λ

We employ a Monte Carlo Markov Chain technique to place constraints on the matter density parameters and the two nuisance parameters. We adopt a flat cosmological model, i.e. $\Omega_m + \Omega_\Lambda = 1$, and assume a flat prior on all free parameters, i.e. Ω_m, α and Υ. With a straightforward generalization of the χ^2 function from Astier et al. (2006), the adopted likelihood function L is

$$L \propto \prod_i \exp\left[\frac{\Delta_i^2}{2\sigma_i^2}\right]\frac{1}{\sigma_i}, \tag{4.5}$$

with $\Delta_i = m_{V,i}^{\rm corr} - \alpha\Delta m_{V,15,i} - \Upsilon - 5\log\mathcal{D}_L(z_i,\Omega_m)$, where $\sigma_i^2 = \sigma^2(m_{V,i}^{\rm corr}) + \alpha^2\sigma^2(\Delta m_{V,15,i})$, and $\sigma(m_{V,i}^{\rm corr})$ and $\sigma(\Delta m_{V,15,i})$ are the errors of $m_{V,i}^{\rm corr}$ and $\Delta m_{V,15,i}$, respectively. The formula for σ_i assumes an independent propagation of errors in $m_{V,i}^{\rm corr}$ and $\Delta m_{V,15,i}$. We verify this assumption by finding no signature of a correlation between $m_V^{\rm corr}$ and $\Delta m_{V,15}$ in a covariance matrix obtained from fitting the light curves.

The marginalised posterior probability densities of Ω_m, α and Υ are shown in Figure 4.2. The confidence levels of the density contours are 68.3% and 95.5%. We quantify the fit in terms of the maximum-likelihood values and confidence intervals containing 68.3% of the corresponding marginal probabilities. The best-fit nuisance parameters are $\alpha = 1.37^{+0.36}_{-0.19}$ and $\Upsilon = -4.50^{+0.17}_{-0.32}$, which are consistent with the values derived from the luminosity-decline rate relation, assuming $\Omega_m = 0.315$ and $H_0 = 67.3$ km s^{-1} Mpc^{-1} (Li & Hjorth, 2014). In a flat universe, the best-fit cosmological model is $(\Omega_m, \Omega_\Lambda) = (0.58^{+0.22}_{-0.25}, 0.42^{+0.25}_{-0.22})$.

Figure 4.3 shows the Hubble diagram for eight GRB-SNe systems. The effective magnitudes $m_V^{\rm eff}$ of the GRB-SN systems in the rest frame V band are plotted as red points. The best cosmological model is the black curve. For comparison, we plot three other cosmological models: $\{(\Omega_m,\Omega_\Lambda)\} = \{(0,1),(0.32,0.68),(1,0)\}$ as dotted lines. The lower panel in Figure 4.3 shows the magnitude residuals relative to the best cosmological model.

4.5 CONCLUSION

The cosmological parameters Ω_m and Ω_Λ can be constrained with SNe Ia (Knop et al., 2003; Perlmutter et al., 1999), CMB radiation (Planck Collaboration et al., 2013; Spergel et al., 2003), and clusters of galaxies (Allen et al., 2002; **?**). As shown in this paper, GRB-SNe may add further constraints on cosmological parameters. With more systems at z up to 1, the result would be more constraining, but we have opted here for systems with very well sampled light curves. At higher redshifts ($z > 1.5$), with more powerful telescope to be launched, e.g., *JWST*, GRB-SNe are potential candidates to break the degeneracies and constrain the equation of state parameter $w(z)$ (King et al., 2013; Linder & Huterer, 2003).

We thank Enrico Ramirez-Ruiz, Tomotsugu Goto and Dong Xu for their many helpful

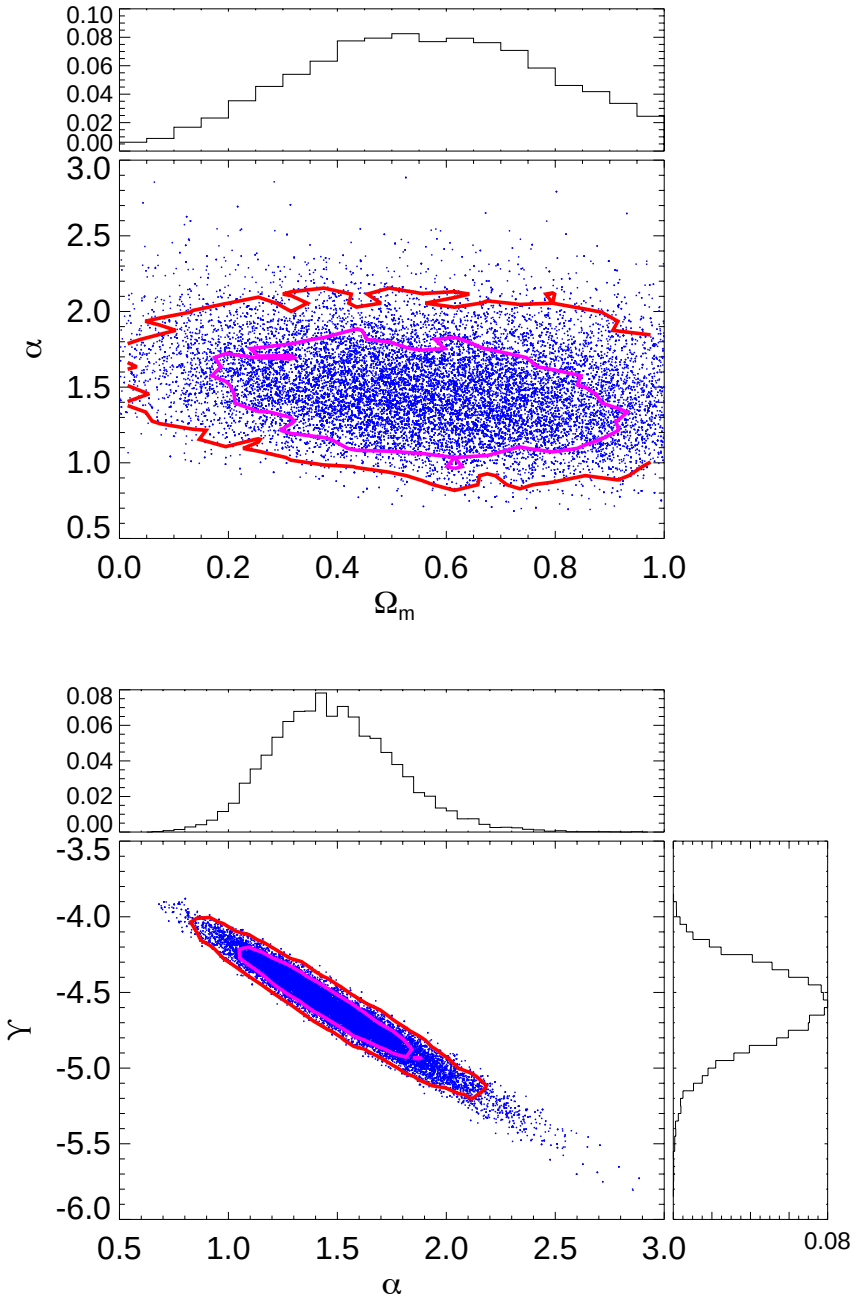

Figure 4.2: Constraints on α, Υ and Ω_m assuming a flat cosmological model. The confidence levels of the density contours are 68.3% and 95.5%.

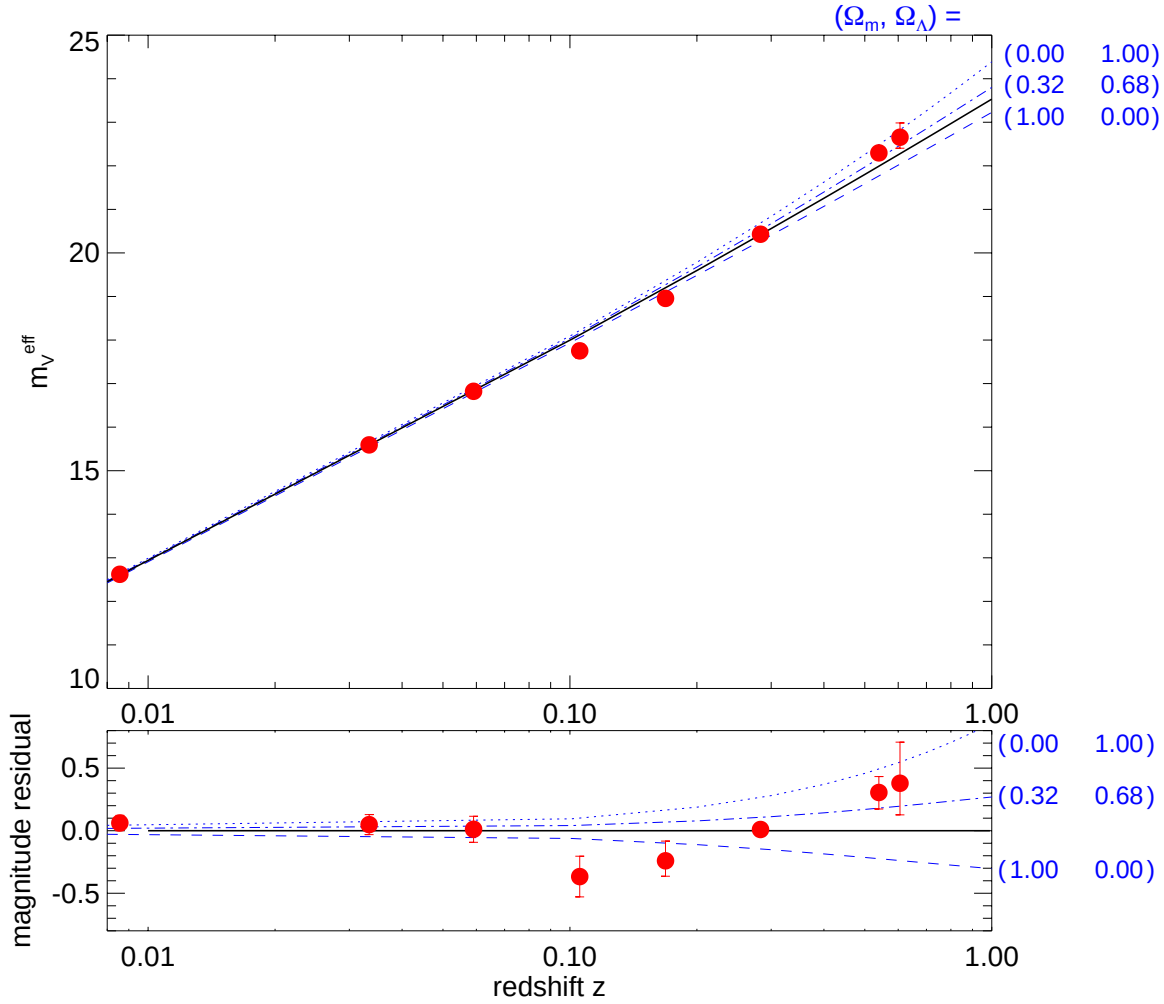

Figure 4.3: Hubble diagram for GRB-SNe. The effective apparent magnitudes of eight GRB-SNe plotted as red points, are calculated using the best-fit parameters $\alpha = 1.37$ and $\Upsilon = -4.50$. The best cosmological model with $(\Omega_m, \Omega_\Lambda) = (0.58, 0.42)$ is in black, while other models (labeled on the right side of the figure) are in blue. The lower panel shows the magnitude residuals from the best-fit cosmological model.

discussions. We thank Stefan Gottlöber for making available one of the CLUES simulations (http://www.clues-project.org/). The simulation has been performed at the Leibniz Rechenzentrum (LRZ), Munich. The Dark Cosmology Centre is funded by the Danish National Research Foundation.

5

CONCLUSIONS AND OUTLOOK

Three things
cannot be long hidden:
the sun, the moon,
and the truth.
buddha

In this thesis, we have explored properties of SNe, especially GRB-SNe. GRB-SNe can be used as standard candles in measuring cosmic distance. Their light curves also show Phillips relation similar to SN Ia, whose peak magnitudes are correlated with decline rates. Considering that they are associated with GRBs, and GRBs are extremely bright that they can be easily detected, so we can detect light curves of GRB-SNe, especially around the peaks. Corrected peak magnitudes with the decline rates, GRB-SNe can be used to measure distance in the universe and constrain cosmological parameters.

The first main topic, which is discussed in Chapter 2, is the time delay distribution and the rates of observing a lensed SN behind Abell 1689. Started with SIS profile, we first theoretically analyze the time delays in strong gravitational lensing systems. Perturbs are then added into the system. A theoretical function describing the distribution of time delays is derived. The effects of different mass profiles on the time delay distribution are also discussed. The dPIE profile has the shallowest slope, NFW is steeper, and SIS is the steepest one. Taking cluster Abell 1689 as an example, time delays are simulated with different mass clumps. We find that small time delays ($<$ 1000 days) are most generated by low massive clumps with velocity dispersion $\sigma < 500$ km s^{-1}. With 17 strong lensing clusters, we constrain the parameters in the theoretical time delay distribution function. The clusters are selected that at least one image is spectroscopically confirmed, as well as the range of the redshifts of the clusters are as large as possible. The rates of observing a lensed background SN behind Abell 1689 is calculated. For SN Ia, the rate is associated with both the mass and the star-formation rate of a host galaxy. A two component model is used with one component describing the mass contribution and

the other being the star-formation contribution. For CC SNe, the rate can be estimated with the star-formation rate of a host galaxy. Assuming the SNe are located at $z = 3$, the yearly rate of observing a lensed SN with time delays less than 1000 days is small. With more powerful space telescope to be launched, the rates of observing a lensed SN will rise.

As discussed in Chapter 3, the second main topic is on the light curves of GRB-SNe. Observed light curves of a GRB-SN are a combination of a GRB afterglow, a host galaxy and a SN. The difficulty in obtaining an intrinsic light curve of a SN is to subtract the afterglow and the host brightness from the total brightness. Sometimes a GRB afterglow is too bright, though it decays exponentially, it is still bright enough to conceal the SN, or a host galaxy where the SN is located at is brighter than the SN. In these cases, the light curve of a SN is not detectable. Furthermore, dust along the line of sight is also needed to be considered. In Chapter 3, we presented a general step to obtain the light curves of GRB-SNe. The standard Monte Carlo method is widely used in error estimation. First the flux from the host galaxy is subtracted. Then we subtract the afterglow contribution by assuming the afterglow decays in a power law or a broken power-law way. This is different from the commonly used smooth function, but as discussed in the chapter, the results in both ways are similar and consistent with each other. After that, we estimate dust extinction in the Milky Way. DIRBE/IRAS dust map is used to constrain the foreground extinction. A recalibration value is multiplied in order to correct the overestimated dust map. We also eliminate the host extinction from the literature. An updated cosmological parameters are applied in distance modulus calculation. A multi-band K correction is applied to the systems which have been observed in two or more bands and two bands are appropriate for interpolation. We also build the SN 1998bw peak SED and decline rate templates for those where multi-band K correction is not applicable. These templates are built based on the light curves of SN 1998bw in U, B, V, R and I bands. Compared to other steps, this is only a second order effect. The comparison between two K correction methods is discussed and applied. The light curve data are fitted in polynomial functions, and most of them are in 3rd or 4th order. Among 21 GRB-SNe which have 'strongest evidence' to be associated with GRB, we succeed in getting 8 light curves. We also present the reason for those we failed to obtain the light curves. Most of them lack enough data to do polynomial fitting, either the afterglow subtraction take away too many data or the observational data are not sufficient. There are two systems have uncertain extinction or host galaxy contributions. One system lack data in proper bands to do the K correction. With eight light curves, we find the correlation between the peak magnitudes and the decline rates. The correlation effects: Pearson's, Kendal's and Spearman's are calculated. The peak magnitudes and the decline rates are stronger correlated than the k and s factors. The correlation between the peak magnitudes, the peak times, and the decline rates are presented. Rescaled light curves with decline rates, factor s and peak time are presented. Among them, GRB-SNe show the most uniform light curves with corrected with the decline rates.

The third main topic is an application of the correlation between the peak magnitude and the decline rate, which is discussed in Chapter 5. With the corrected peak magnitudes, we constrained the cosmological parameters Ω_M and Ω_Λ. Extinction and K correction are corrected to get apparent peak magnitudes of eight GRB-SNe mentioned above. With the Standard Monte Carlo method, the effective apparent magnitudes and the decline rates are simulated with $1-\sigma$ uncertainties covering the 68% of the total simulation values to constrain the best cosmological parameters Ω_M, assuming a flat universe. A Hubble diagram is shown in flat universe.

The correlation between the peak magnitudes and the decline rates indicates that the light curves of GRB-SNe behave similar to SNe Ia. Though the progenitor scenarios of SNe Ia and GRB-SNe are different, their light curves have similar property and this makes them standard candles in cosmic distance measurements. This correlation can further constrain the progenitor model of GRB-SNe.

The rate of CC SNe do not decline rapidly beyond $z > 1.5$, and GRB-SNe are associated with the most luminous events in the universe: gamma-ray bursts, which make GRB-SNe potential candidates as high redshift standard candles. With JWST to be launched, GRB-SNe are potential candidates to breakdown the degeneracies and constrain the equation of state parameter $w(z)$. GRB-SNe are potentially useful tools in dark energy research.

A

SUPPLEMENTARY MATERIALS

To test the accuracy of the code constraining the cosmological parameter Ω_m (Li et al., 2014), we use a different approach to constrain the best resultant free parameters α, Υ and Ω_m.

A.1 CROSS-CHECKING OF CONSTRAINING THE PARAMETERS α, Υ AND Ω_m

Covariance matrix does not show any relevant correlation between $m_V^{\rm corr}$ and $\Delta m_{\rm V,15}$. We simulate $m_V^{\rm corr}$ and $\Delta m_{\rm V,15}$ independently with a standard Monte Carlo method. The data are simulated 10^4 times with 68.3% of the total simulated data covering 1σ uncertainties of the observed data.

The procedure of constraining Ω_m is similar to Astier et al. (2006). We constrain the cosmological parameters in a flat universe with $\Omega_\Lambda = 1 - \Omega_m$ and Ω_m ranging from 0 to 1. For each simulated data set (including eight $m_V^{\rm corr}$ and eight $\Delta m_{\rm V,15}$), we constrain the best-fit values of α, Υ and Ω_m by minimizing

$$\chi^2 = \sum_{i=1}^{8} \frac{(m_{\rm V,i}^{\rm corr} - \alpha \Delta m_{\rm V,15,i} - \Upsilon - 5\log \mathcal{D}_L(z;\Omega_m))^2}{\sigma^2(m_{\rm V,i}^{\rm corr}) + \alpha^2\sigma^2(\Delta m_{\rm V,15,i})}, \tag{A.1}$$

where $\sigma(m_V^{\rm corr})$ and $\sigma(\Delta m_{\rm V,15})$ are the 1σ uncertainties of the data $m_{\rm V}^{\rm corr}$ and $\Delta m_{\rm V,15}$.

The obtained constraints on the model parameters are shown in Figure A.1. The confidence levels of the density contours are 68.3%, 90% and 95.5%. We choose the median values of the distributions of α, Υ and Ω_m as the best-fit values and 68% confidence level around the median values as the errors. The best free parameters are $\alpha = 1.59^{+0.31}_{-0.28}$ and $\Upsilon = -4.68^{+0.25}_{-0.27}$, which are consistent with the values derived from the luminosity-decline rate relation, assuming $\Omega_m = 0.315$ and $H_0 = 67.3$ km s^{-1} Mpc^{-1} (Li & Hjorth, 2014). In a flat universe, the best-fit cosmological model is $(\Omega_m, \Omega_\Lambda) = (0.52^{+0.34}_{-0.31}, 0.48^{+0.31}_{-0.34})$. With more systems at z up to 1, the result would be more constraining, but we have opted here for systems with very well sampled light curves.

Figure A.2 shows the Hubble diagram for eight GRB-SNe systems. The effective magnitudes $m_V^{\rm eff}$ of the GRB-SN systems in the rest frame V band are plotted as red points.

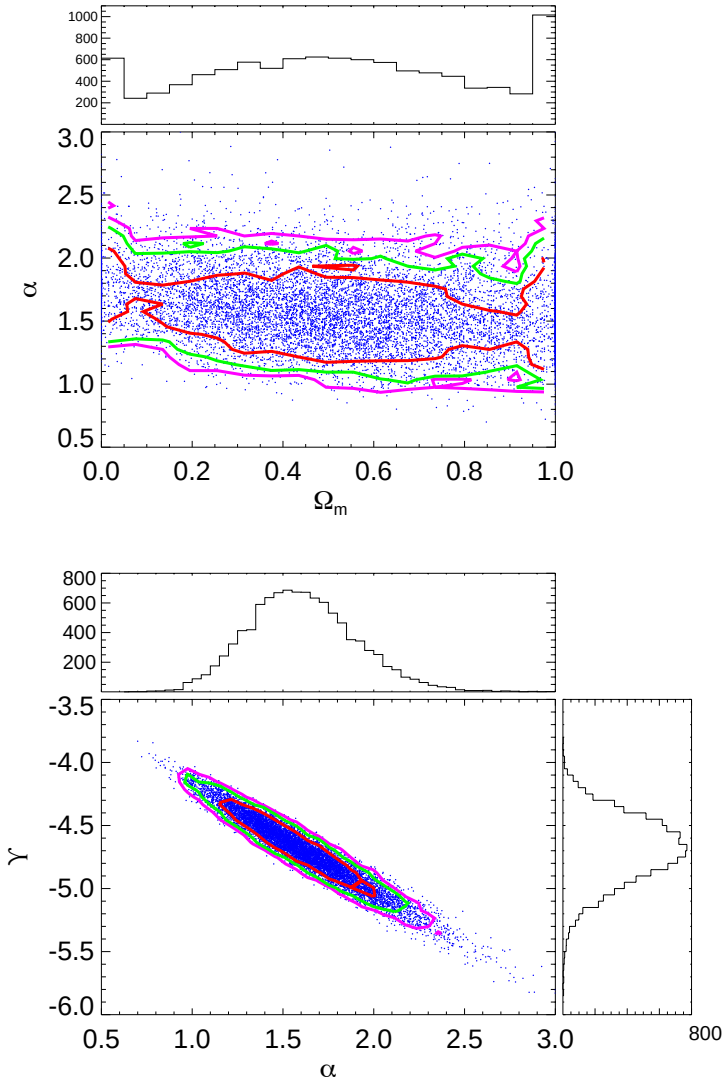

Figure A.1: Cross-checking of the resultant parameters α, Υ and Ω_m, assuming a flat cosmological model. The confidence levels of the density contours are 68.3%, 90% and 95.5%.

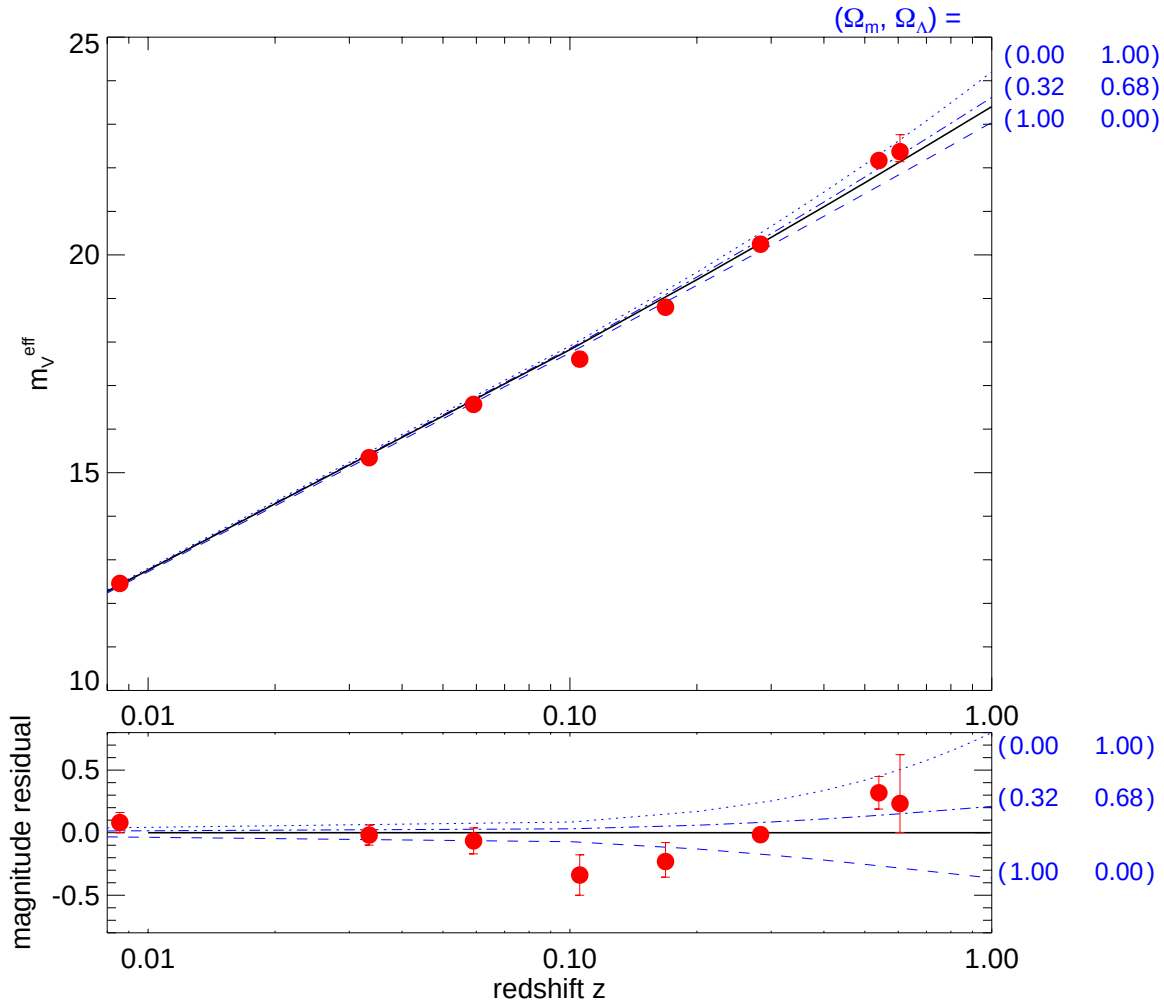

Figure A.2: Cross-checking of the Hubble diagram for GRB-SNe. The effective apparent magnitudes of eight GRB-SNe plotted as red points, are calculated using the best-fit parameters $\alpha = 1.59$ and $\Upsilon = -4.68$. The best cosmological model with $(\Omega_m, \Omega_\Lambda) = (0.52, 0.48)$ is in black, while other models (labeled on the right side of the figure) are in blue. The lower panel shows the magnitude residuals from the best-fit cosmological model.

The best cosmological model is the black curve. In comparison, three other cosmological models: $\{(\Omega_m, \Omega_\Lambda)\} = \{(0,1), (0.32, 0.68), (1,0)\}$ are also plotted as dotted lines. The lower panel in Figure A.2 shows the magnitude residuals relative to the best cosmological model.

The discussion above shows that though the two procedures are different in constraining α, Υ and Ω_m, the results are consistent with each other.

A.2 CODE TEST ON SCATTERS

To test the effects of the uncertainties of the data on the uncertainties of Ω_m and Ω_Λ, with the same procedure in Section A.1, we generate sets of pseudo-data containing $M_{\mathrm{V,peak}}$, $\Delta m_{15,\mathrm{V}}$ and their uncertainties and the redshifts, under a certain value of Ω_m, α and Υ, then we vary the scatter of m_{V} and Δm_{15}, i.e., m^{scat}. The uncertainties of Ω_m and Ω_Λ are changed according to the changes of $\sigma(m^{\mathrm{scat}})$. We generate an initial set of m^{scat}. When the input σ_{input} changes, the scatter values are multiplied by a factor of $\sigma_{\mathrm{input}}/\sigma(m^{\mathrm{scat}})$ to make a new scatter $m^{\mathrm{scat,new}}$. The pseudo-data are generated in $\Omega_m = 0.3$ and $\Omega_\Lambda = 0.7$. The uncertainties of Ω_m change as a function of σ_{input} as shown in blue in Figure A.3. In general, as we expected, the uncertainties of the best cosmological parameters become larger as $\sigma(\delta m_{\mathrm{V}}^{\mathrm{pseudo}})$ increases.

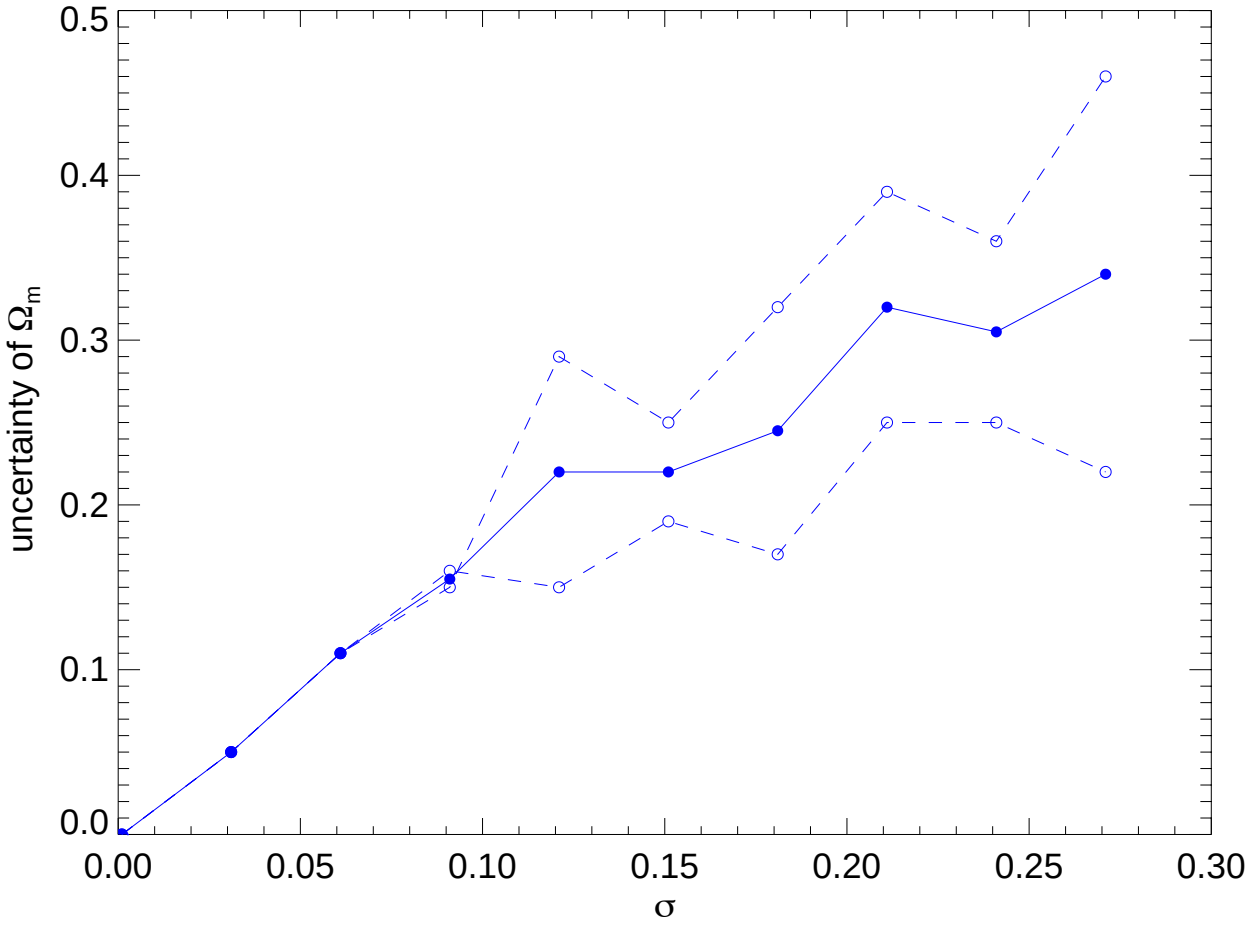

Figure A.3: Uncertainties of best cosmological parameters as a function of pseudo-scatters of the pseudo-data generated in $\Omega_m = 0.3$ and $\Omega_\Lambda = 0.7$. The open points and dashed lines represent the upper and lower uncertainties, while filled points and bold lines show the averaged uncertainties (average of upper and lower limits).

B

COAUTHOR STATEMENTS

B.1 Paper I

The rates and time-delay distribution of multiply imaged supernovae behind lensing clusters

by

Xue Li, Jens Hjorth and Johan Richard

Submitted to Journal of Cosmology and Astroparticle Physics, Issue 11, article id. 015 (2012)

Chapter 2 is based on this paper. Xue Li did all the data analysis, wrote all of the software and the paper draft. Jens Hjorth provided extensive feedback throughout the writing and analysis process. Johan Richard provided mass models and feedback in the writing and analysis process.

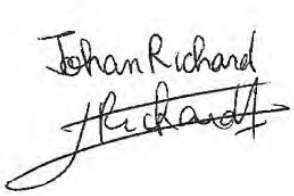

B.2 Paper II

Light Curve Properties of Supernovae Associated With Gamma-ray Bursts

by

Xue Li, and Jens Hjorth

Submitted to Astronomy & Astrophysics

Chapter 3 is based on this paper. Xue Li did all the data analysis, wrote all of the software and the paper draft. Jens Hjorth provided extensive feedback throughout the writing and analysis process.

B.3 Paper III

Cosmological parameters from supernovae associated with gamma-ray bursts

by

Xue Li, Jens Hjorth and Radek Wojtak

Submitted to The Astrophysical Journal Letters

Chapter 4 is based on this paper. Xue Li did data analysis, wrote most of the software and the major part of the paper draft. Jens Hjorth provided extensive feedback throughout the writing and analysis process. Radek Wojtak calculated the constraints on the parameters, wrote the draft of the peculiar velocity section and the parameter constraint paragraphs, provided feedback throughout the writing and analysis process.

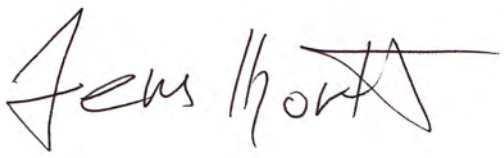

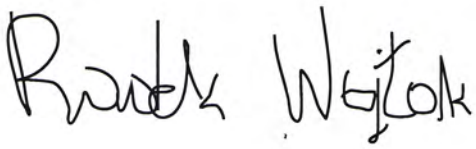

BIBLIOGRAPHY

Allen, S. W., Schmidt, R. W., & Fabian, A. C. 2002, Mon. Not. R. Astron. Soc., 334, L11

Anderson, J. P., Habergham, S. M., & James, P. A. 2011, Mon. Not. R. Astron. Soc., 416, 567

Astier, P., et al. 2006, Astron. Astrophys., 447, 31

Badenes, C., Hughes, J. P., Bravo, E., & Langer, N. 2007, Astrophys. J., 662, 472

Bersier, D., et al. 2006, Astrophys. J., 643, 284

Bildsten, L., Shen, K. J., Weinberg, N. N., & Nelemans, G. 2007, Astrophys. J. Lett., 662, L95

Binney, J., & Tremaine, S. 2008, GALACTIC DYNAMICS (Princeton Series in Astrophysics)

Björnsson, G., Hjorth, J., Jakobsson, P., Christensen, L., & Holland, S. 2001, Astrophys. J. Lett., 552, L121

Blandford, R. D., & Narayan, R. 1992, Annual Review of Astronomy and Astrophysics, 30, 311

Bloom, J. S., et al. 1999, Nature, 401, 453

—. 2002, Astrophys. J. Lett., 572, L45

—. 2009, Astrophys. J., 691, 723

Blustin, A. J., et al. 2006, Astrophys. J., 637, 901

Branch, D., Livio, M., Yungelson, L. R., Boffi, F. R., & Baron, E. 1995, Publications of the Astronomical Society of the Pacific, 107, 1019

Bufano, F., et al. 2012, Astrophys. J., 753, 67

Campana, S., et al. 2006, Nature, 442, 1008

Cano, Z. 2013, Mon. Not. R. Astron. Soc., 434, 1098

—. 2014, ArXiv e-prints

Cano, Z., et al. 2011a, Mon. Not. R. Astron. Soc., 413, 669

—. 2011b, Astrophys. J., 740, 41

Cardelli, J. A., Clayton, G. C., & Mathis, J. S. 1989, Astrophys. J., 345, 245

Christensen, L., Hjorth, J., Gorosabel, J., Vreeswijk, P., Fruchter, A., Sahu, K., & Petro, L. 2004, Astron. Astrophys., 413, 121

Clocchiatti, A., Suntzeff, N. B., Covarrubias, R., & Candia, P. 2011, Astron. J., 141, 163

Cobb, B. E., Bloom, J. S., Perley, D. A., Morgan, A. N., Cenko, S. B., & Filippenko, A. V. 2010, Astrophys. J. Lett., 718, L150

Coe, D., & Moustakas, L. A. 2009, Astrophys. J., 706, 45

Cooke, J. H., & Kantowski, R. 1975, Astrophys. J. Lett., 195, L11+

Dahlen, T., Strolger, L.-G., & Riess, A. G. 2008, Astrophys. J., 681, 462

Dahlen, T., et al. 2004, Astrophys. J., 613, 189

D'Andrea, C. B., et al. 2010, Astrophys. J., 708, 661

Darbha, S., Metzger, B. D., Quataert, E., Kasen, D., Nugent, P., & Thomas, R. 2010, Mon. Not. R. Astron. Soc., 409, 846

Davis , T. 2013, private communication

Della Valle, M., et al. 2003, Astron. Astrophys., 406, L33

—. 2006, Astrophys. J. Lett., 642, L103

Dilday, B., et al. 2008, Astrophys. J., 682, 262

—. 2010, Astrophys. J., 713, 1026

Drout, M. R., et al. 2011, Astrophys. J., 741, 97

Dunkley, J., et al. 2009, Astrophys.J.Suppl., 180, 306

Efstathiou, G., Sutherland, W. J., & Maddox, S. J. 1990, Nature, 348, 705

Eisenstein, D. J., et al. 2005, Astrophys. J., 633, 560

Elíasdóttir, Á., et al. 2007, ArXiv e-prints

Ferrero, P., et al. 2006, Astron. Astrophys., 457, 857

Fink, M., Hillebrandt, W., & Röpke, F. K. 2007, Astron. Astrophys., 476, 1133

Fixsen, D. J., Cheng, E. S., Gales, J. M., Mather, J. C., Shafer, R. A., & Wright, E. L. 1996, Astrophys. J., 473, 576

Foley, S., Watson, D., Gorosabel, J., Fynbo, J. P. U., Sollerman, J., McGlynn, S., McBreen, B., & Hjorth, J. 2006, Astron. Astrophys., 447, 891

Fynbo, J. P. U., et al. 2006, Nature, 444, 1047

Gal-Yam, A., et al. 2006, Nature, 444, 1053

Galama, T. J., et al. 1998, Nature, 395, 670

—. 2000, Astrophys. J., 536, 185

Gall, C., Hjorth, J., & Andersen, A. C. 2011, The Astronomy and Astrophysics Review, 19, 43

Garnavich, P. M., et al. 2003, Astrophys. J., 582, 924

Gehrels, N., et al. 2006, Nature, 444, 1044

Giavalisco, M., et al. 2004, Astrophys. J. Lett., 600, L103

Goicoechea, L. J., & Shalyapin, V. N. 2010, ApJ, 708, 995

Gottloeber, S., Hoffman, Y., & Yepes, G. 2010, ArXiv e-prints

Graur, O., et al. 2011, ArXiv e-prints

—. 2014, Astrophys. J., 783, 28

Greiner, J., et al. 2003, Astrophys. J., 599, 1223

Guenther, E. W., Klose, S., Vreeswijk, P., Pian, E., & Greiner, J. 2006, GRB Coordinates Network, 4863, 1

Guerrero, J., García-Berro, E., & Isern, J. 2004, Astron. Astrophys., 413, 257

Guillochon, J., Dan, M., Ramirez-Ruiz, E., & Rosswog, S. 2010, Astrophys. J. Lett., 709, L64

Hachisu, I., Kato, M., & Nomoto, K. 1999, Astrophys. J., 522, 487

Hamuy, M., et al. 1996, Astron. J., 112, 2408

Heise, J., Zand, J. I., Kippen, R. M., & Woods, P. M. 2001, in Gamma-ray Bursts in the Afterglow Era, ed. E. Costa, F. Frontera, & J. Hjorth, 16

Hillebrandt, W., & Niemeyer, J. C. 2000, Annual Review of Astronomy and Astrophysics, 38, 191

Hjorth, J. 2013, Royal Society of London Philosophical Transactions Series A, 371, 20275

Hjorth, J., & Bloom, J. S. 2012, The Gamma-Ray Burst - Supernova Connection, 169–190

Hjorth, J., et al. 2003, Nature, 423, 847

Hogg, D. W. 1999, ArXiv Astrophysics e-prints

Hogg, D. W., Baldry, I. K., Blanton, M. R., & Eisenstein, D. J. 2002, ArXiv Astrophysics e-prints

Hook, I. M. 2013, Royal Society of London Philosophical Transactions Series A, 371, 20282

Hoyle, F., & Fowler, W. A. 1960, Astrophys. J., 132, 565+

Iwamoto, K., et al. 1998, Nature, 395, 672

Jin, Z.-P., et al. 2013, Astrophys. J., 774, 114

Jullo, E., Kneib, J.-P., Limousin, M., Elíasdóttir, Á., Marshall, P. J., & Verdugo, T. 2007, New Journal of Physics, 9, 447

Jullo, E., Natarajan, P., Kneib, J.-P., D'Aloisio, A., Limousin, M., Richard, J., & Schimd, C. 2010, Science, 329, 924

Keeton, C. R., Kochanek, C. S., & Seljak, U. 1997, Astrophys. J., 482, 604

Keeton, C. R., & Madau, P. 2001, Astrophys. J. Lett., 549, L25

Kennicutt, Jr., R. C. 1998, Ann.Rev.Astron.Astrophys, 36, 189

King, A. L., Davis, T. M., Denney, K., Vestergaard, M., & Watson, D. 2013, ArXiv e-prints

Klebesadel, R. W., Strong, I. B., & Olson, R. A. 1973, Astrophys. J. Lett., 182, L85

Klose, S., Greiner, J., Fynbo, J., Nicuesa Guelbenzu, A., Schmidl, S., Rau, A., & Kruehler, T. 2012, Central Bureau Electronic Telegrams, 3200, 1

Kneib, J.-P., & Natarajan, P. 2011, The Astronomy and Astrophysics Review, 19, 47

Knop, R. A., et al. 2003, Astrophys. J., 598, 102

Kobayashi, C., & Nomoto, K. 2009, Astrophys. J., 707, 1466

Kochanek, C. S. 2002, Astrophys. J., 578, 25

Kochanek, C. S., & Schechter, P. L. 2004, Measuring and Modeling the Universe, 117

Koekemoer, A. M., et al. 2011, Astrophys.J.Suppl., 197, 36

Komatsu, E., et al. 2011, Astrophys.J.Suppl., 192, 18

Kouveliotou, C., Meegan, C. A., Fishman, G. J., Bhat, N. P., Briggs, M. S., Koshut, T. M., Paciesas, W. S., & Pendleton, G. N. 1993, Astrophys. J. Lett., 413, L101

Kulkarni, S. R., et al. 1998, Nature, 395, 663

Küpcü Yoldaş, A., Salvato, M., Greiner, J., Pierini, D., Pian, E., & Rau, A. 2007, Astron. Astrophys., 463, 893

Leloudas, G. 2014, private communication

Leonard, D. C. 2007, Astrophys. J., 670, 1275

Levan, A. J., et al. 2013, ArXiv e-prints

Li, X., & Hjorth, J. 2014

Li, X., Hjorth, J., & Richard, J. 2012, The Journal of Cosmology and Astroparticle Physics , 11, 15

Li, X., Hjorth, J., & Wojtak, R. 2014, ArXiv e-prints

Limousin, M., et al. 2007, The Astrophysical Journal, 668, 643

Linder, E. V. 2011, Phys. Rev. D, 84, 123529

Linder, E. V., & Huterer, D. 2003, Phys. Rev. D, 67, 081303

MacFadyen, A. I., & Woosley, S. E. 1999, Astrophys. J., 524, 262

MacFadyen, A. I., Woosley, S. E., & Heger, A. 2001, Astrophys. J., 550, 410

Malesani, D. 2013, private communication

Malesani, D., et al. 2004, Astrophys. J. Lett., 609, L5

Mannucci, F., Della Valle, M., Panagia, N., Cappellaro, E., Cresci, G., Maiolino, R., Petrosian, A., & Turatto, M. 2005, Astron. Astrophys., 433, 807

Maoz, D., & Mannucci, F. 2011, ArXiv e-prints

Masetti, N., et al. 2003, Astron. Astrophys., 404, 465

Massey, R., Kitching, T., & Richard, J. 2010, Reports on Progress in Physics, 73, 086901

Matheson, T., et al. 2003, Astrophys. J., 599, 394

Mazzali, P. A., McFadyen, A. I., Woosley, S. E., Pian, E., & Tanaka, M. 2014, Mon. Not. R. Astron. Soc., 443, 67

Mazzali, P. A., Walker, E. S., Pian, E., Tanaka, M., Corsi, A., Hattori, T., & Gal-Yam, A. 2013, Mon. Not. R. Astron. Soc., 432, 2463

Mazzali, P. A., et al. 2006, Astrophys. J., 645, 1323

McBreen, S., et al. 2008, Astrophys. J. Lett., 677, L85

Melandri, A., et al. 2012, Astron. Astrophys., 547, A82

Metzger, M. R., Djorgovski, S. G., Kulkarni, S. R., Steidel, C. C., Adelberger, K. L., Frail, D. A., Costa, E., & Frontera, F. 1997, Nature, 387, 878

Munari, U., & Zwitter, T. 1997, Astron. Astrophys., 318, 269

Narayan, R., & Bartelmann, M. 1996, ArXiv Astrophysics e-prints

Nasonova, O. G., & Karachentsev, I. D. 2011, Astrophysics, 54, 1

Navarro, J. F., Frenk, C. S., & White, S. D. M. 1996, Astrophys. J., 462, 563

Neill, J. D., et al. 2006, Astron. J., 132, 1126

Nomoto, K., & Iben, Jr., I. 1985, Astrophys. J., 297, 531

Nordin, J., et al. 2011, Astron. Astrophys., 526, A119+

Ofek, E. O., et al. 2007, Astrophys. J., 662, 1129

Oguri, M., & Kawano, Y. 2003, Mon. Not. R. Astron. Soc., 338, L25

Oguri, M., Taruya, A., Suto, Y., & Turner, E. L. 2002, Astrophys. J. Lett., 568, 488

Olivares E., F., et al. 2012, Astron. Astrophys., 539, A76

Pan, T., & Loeb, A. 2013, Mon. Not. R. Astron. Soc., 435, L33

Paraficz, D., & Hjorth, J. 2009, Astron. Astrophys., 507, 49

—. 2010, Astrophys. J., 712, 1378

Peebles, P. J., & Ratra, B. 2003, Reviews of Modern Physics, 75, 559

Pei, Y. C. 1992, Astrophys. J., 395, 130

Percival, W. J., et al. 2010, Mon. Not. R. Astron. Soc., 401, 2148

Perlmutter, S., et al. 1997, Astrophys. J., 483, 565

—. 1999, Astrophys. J., 517, 565

Perrett, K., et al. 2012, Astron. J., 144, 59

Phillips, M. M. 1993, Astrophys. J. Lett., 413, L105

Phillips, M. M., Lira, P., Suntzeff, N. B., Schommer, R. A., Hamuy, M., & Maza, J. 1999, Astron. J., 118, 1766

Planck Collaboration et al. 2013, ArXiv e-prints

Poznanski, D., Prochaska, J. X., & Bloom, J. S. 2012, Mon. Not. R. Astron. Soc., 426, 1465

Price, P. A., et al. 2003, Astrophys. J., 589, 838

Prochaska, J. X., et al. 2004, Astrophys. J., 611, 200

Refsdal, S. 1964, Mon. Not. R. Astron. Soc., 128, 307

Richard, J. 2010

—. 2011

Richard, J., et al. 2010, Mon. Not. R. Astron. Soc., 404, 325

Richardson, D. 2009, Astron. J., 137, 347

Richardson, D., Branch, D., & Baron, E. 2006, Astron. J., 131, 2233

Riehm, T., et al. 2011, Astron. Astrophys., 536, A94

Riess, A. G., et al. 1998, Astron. J., 116, 1009

Rodney, S. A., et al. 2014, Astron. J., 148, 13

Rusin, D. 2000, ArXiv Astrophysics e-prints

Saha, P., Coles, J., Macciò, A. V., & Williams, L. L. R. 2006, Astrophys. J. Lett., 650, L17

Sahu, K. C., et al. 2000, Astrophys. J., 540, 74

Samsing, J. 2010

Scannapieco, E., & Bildsten, L. 2005, Astrophys. J. Lett., 629, L85

Schlafly, E. F., & Finkbeiner, D. P. 2011, Astrophys. J., 737, 103

Schlegel, D. J., Finkbeiner, D. P., & Davis, M. 1998, Astrophys. J., 500, 525

Schneider, P., Ehlers, J., & Falco, E. 1992, Gravitational Lenses (Springer-Verlag)

Schulze, S., et al. 2014, ArXiv e-prints

Shen, K. J., Bildsten, L., Kasen, D., & Quataert, E. 2012, Astrophys. J., 748, 35

Smartt, S. J. 2009, Annual Review of Astronomy and Astrophysics, 47, 63

Smith, M., et al. 2011, ArXiv e-prints

Soderberg, A. M., et al. 2005, Astrophys. J., 627, 877

—. 2006, Astrophys. J., 636, 391

Sollerman, J., et al. 2002, Astron. Astrophys., 386, 944

—. 2006, Astron. Astrophys., 454, 503

Sparre, M., et al. 2011, Astrophys. J. Lett., 735, L24

Spergel, D. N., et al. 2003, Astrophys.J.Suppl., 148, 175

Stanek, K. Z., et al. 2003, Astrophys. J. Lett., 591, L17

—. 2005, Astrophys. J. Lett., 626, L5

Sullivan, M., et al. 2006, Astrophys. J., 648, 868

Suyu, S. H., Marshall, P. J., Auger, M. W., Hilbert, S., Blandford, R. D., Koopmans, L. V. E., Fassnacht, C. D., & Treu, T. 2010, Astrophys. J., 711, 201

Suyu, S. H., et al. 2012, ArXiv e-prints

Suzuki, N., et al. 2012, Astrophys. J., 746, 85

Tanvir, N. R., et al. 2010, Astrophys. J., 725, 625

Troja, E., et al. 2012, Astrophys. J., 761, 50

Šimon, V., Pizzichini, G., & Hudec, R. 2010, Astron. Astrophys., 523, A56

van Dokkum, P. G., & Franx, M. 1996, Mon. Not. R. Astron. Soc, 281, 985

van Paradijs, J., et al. 1997, Nature, 386, 686

Vergani, S. D., et al. 2011, Astron. Astrophys., 535, A127

Walcher, J., Groves, B., Budavári, T., & Dale, D. 2011, Astrophysics and Space Science, 331, 1

Webbink, R. F. 1984, Astrophys. J., 277, 355

Whelan, J., & Iben, Jr., I. 1973, Astrophys. J., 186, 1007

Wiersema, K., et al. 2008, Astron. Astrophys., 481, 319

Witt, H. J., & Mao, S. 1997, Mon. Not. R. Astron. Soc., 291, 211

Witt, H. J., Mao, S., & Keeton, C. R. 2000, Astrophys. J., 544, 98

Woosley, S. E., & Bloom, J. S. 2006, Annual Review of Astronomy and Astrophysics, 44, 507

Woosley, S. E., Eastman, R. G., & Schmidt, B. P. 1999, Astrophys. J., 516, 788

Wyithe, J. S. B., Turner, E. L., & Spergel, D. N. 2001, Astrophys. J., 555, 504

Xu, D., et al. 2013, Astrophys. J., 776, 98

Zeh, A., Klose, S., & Hartmann, D. H. 2004, Astrophys. J., 609, 952

Zwicky, F. 1937, Physical Review, 51, 679